Boston University

OpenBU **http://open.bu.edu**

Mechanical Engineering ENG: Mechanical Engineering: Theses & Dissertations

2010

PHOTOREFRACTIVE CRYSTAL-BASED ACOUSTO-OPTIC IMAGING IN THE NEAR-INFRARED AND ITS APPLICATIONS

https://hdl.handle.net/2144/1378
Boston University

BOSTON UNIVERSITY

COLLEGE OF ENGINEERING

Dissertation

PHOTOREFRACTIVE CRYSTAL-BASED ACOUSTO-OPTIC IMAGING IN THE NEAR-INFRARED AND ITS APPLICATIONS

by

PUXIANG LAI

B.E., Tsinghua University, 2002
M. S., Chinese Academy of Sciences, 2005

Submitted in partial fulfillment of the
requirements for the degree of
Doctor of Philosophy
2011

Approved by

First Reader (Major Advisor)	Ronald A. Roy, Ph.D. Professor of Mechanical Engineering
Second Reader (Co-Advisor)	Todd W. Murray, Ph.D. Associate Professor of Mechanical Engineering
Third Reader	Paul E. Barbone, Ph.D. Associate Professor of Mechanical Engineering
Fourth Reader	Charles A. DiMarzio, Ph.D. Associate Professor of Electrical Engineering Northeastern University

Dedication

This work is dedicated to

my wife Ning Su,

my sisters,

and my parents.

Thank you all for your love, patience, understanding, and support throughout my life.

Acknowledgements

It is hard to believe that I've been working my dissertation for almost five years, since it feels like I started just yesterday! I can remember my first group meeting with Ron, Todd and Lei. Back then I was panicked by the speed at which Ron spoke, making me afraid to open my mouth to speak English. Nevertheless, five years later I still cannot quite keep up with, but it has been one of the most rewarding experiences of my life. For which I am very grateful to all those people who made it possible and so enjoyable.

My deepest gratitude goes to my advisors, Professor Ronald A. Roy (my Acousto Guru) and Professor Todd W. Murray (my Opto Guru), for their patience, encouragement, unfailing guidance, unflinching motivation and for providing an excellent atmosphere for research. Without them, I would not have the chance to work in the interdisciplinary field of light and sound, providing the opportunity to experience both acoustics and optics. In addition, I would like to thank them for giving me the opportunity to present at many professional conferences, and to communicate with the researchers in the field. I also owe a debt of gratitude to them for the valuable time they spent helping me with papers and presentations, as especially in preparation of this dissertation.

I would like to thank members of my Ph.D dissertation committee, Professor Charles A. DiMarzio and Professor Paul Barbone, for their continued interest in my project, throughout numerous discussions and helpful comments throughout these five years. I thank Professor Robin Cleveland for his invaluable teachings on nonlinear acoustics and ultrasound imaging, and for his advice on research and paper writing. Also I would like to thank Professor Srikanth Gopalan for chairing my dissertation final defense.

I am grateful to work with Dr. Lei Sui in my first year, from whom I inherited a vast amount of practical knowledge of acousto-optic imaging, and would like to thank him for his friendship and encouragement. I would also like to thank Dr. James McLaughlan for his guidance and contribution to my work, especially on HIFU lesion monitoring using AO sensing. It is really my fortune to have had a chance to work with him, where I received helps in both experiments and writing. I would also like to thank my colleague, Andy Draudt, as it is has been a wonderful experience to work with him on HIFU lesion monitoring using AO sensing and the sharing of equipments, and please do not forget all of the interesting discussions with him.

I would also like to express my gratitude to my colleagues and friends who have worked in the Physical Acoustics Laboratory and Laser Acoustic Laboratory over these five years: Tianming Wu, Parag Chitnis, Caleb Farney, Zach Waters, Haibiao Luo, Peng Zhang, Chris Ormonde, Nick Manzi, Jon Kracht, Yanjun Gong, Qi Wang, Phillip Anderson, Thomas Steen, Ashwin Kumar, Suraj Bramhavar, and Hengyi Ju. Their friendship and support have been invaluable to me. Special thanks go to James McLaughlan, Andrew Draudt, Ashwin Kumar and Jon Kracht for their tireless help in carefully proof reading the manuscript for this dissertation.

I acknowledge the generous financial support between 2006-2010 from the Bernard M. Gordon Center for Subsurface and Imaging Systems (CenSSIS) via the NSF ERC award number EEC-9986821.

Most of all, I would like to acknowledge my family, especially my parents and sisters, for their unconditional love and support. Last, but definitely not least, I would like to thank my wife, Ning Su, for her love, trust, understanding, constant encouragement and support for the past ten years. Without her devotion throughout my life, this dissertation would not have been possible.

Puxiang Lai

Boston, MA

May 2010

PHOTOREFRACTIVE CRYSTAL-BASED ACOUSTO-OPTIC IMAGING IN THE NEAR-INFRARED AND ITS APPLICATIONS

(Order No.)

PUXIANG LAI

Boston University, College of Engineering, 2011

Major Professor: Ronald A. Roy, Ph.D., Professor of Mechanical Engineering,

Co-advised by Todd. W. Murray, Ph.D., Associate Professor of Mechanical Engineering, University of Colorado, Boulder

ABSTRACT

Acousto-optic (AO) sensing and imaging (AOI) is a dual-wave modality that combines ultrasound with diffusive light to measure and/or image the optical properties of optically diffusive media, including biological tissues such as breast and brain. The light passing through a focused ultrasound beam undergoes a phase modulation at the ultrasound frequency that is detected using an adaptive interferometer scheme employing a GaAs photorefractive crystal (PRC). The PRC-based AO system operating at 1064 nm is described, along with the underlying theory, validating experiments, characterization, and optimization of this sensing and imaging apparatus. The spatial resolution of AO sensing, which is determined by spatial dimensions of the ultrasound beam or pulse, can be sub-millimeter for megahertz-frequency sound waves.

A modified approach for quantifying the optical properties of diffuse media with AO sensing employs the ratio of AO signals generated at two different ultrasound focal pressures. The resulting “pressure contrast signal” (PCS), once calibrated for a particular set of pressure pulses, yields a direct measure of the spatially averaged optical transport attenuation coefficient within the interaction volume between light and sound. This is a significant improvement over current AO sensing methods since it produces a quantitative measure of the optical properties of optically diffuse media without *a priori* knowledge of the background illumination. It can also be used to generate images based on spatial variations in both optical scattering and absorption.

Finally, the AO sensing system is modified to monitor the irreversible optical changes associated with the tissue heating from high intensity focused ultrasound (HIFU) therapy, providing a powerful method for noninvasively sensing the onset and growth of thermal lesions in soft tissues. A single HIFU transducer is used to simultaneously generate tissue damage and pump the AO interaction. Experimental results performed in excised chicken breast demonstrate that AO sensing can identify the onset and growth of lesion formation in real time and, when used as feedback to guide exposure parameters, results in more predictable lesion formation.

Contents

List of Tables …...…………………………………………………………….....xv

List of Figures ………………………………………………………………….xvi

Chapter 1 Introduction ………………………………………………………………1

1.0 Overview …………………………………………………………………...1

1.1 Overview of imaging modalities for early diagnosis of breast cancer ….……1

1.1.1 Mammography ……………………………………………….....2

1.1.2 Ultrasound imaging used for breast cancer diagnosis …………….……3

1.1.3 Magnetic resonance imaging used for breast cancer diagnosis …..5

1.2 Biomedical optical imaging ……………………………………………..6

1.2.1 Motivation for optical imaging ……………………………...6

1.2.2 Near-surface optical imaging ……………………………….9

1.2.3 Subsurface optical imaging ………………………………...10

1.2.4 Multimodality imaging and dual-wave imaging ………………...11

1.3 Acousto-optic imaging ……………………………………........11

1.3.1 Introduction ……………………………………………...11

1.3.2 The historical development of acousto-optic (AO) sensing and imaging ……………………………..…………..…15

1.4 Motivation and focus of the work ……………………………...28

1.4.1 Understanding the nature of ultrasound-induced modulation on diffuse light ……………………………………………...28

1.4.2 Development of a near-infrared (NIR) AOI system …………….29

1.4.3 Quantitative measurement of local optical properties with AOI...29

1.4.4 Real time monitoring of HIFU therapy using AO sensing ……..30

1.5 Dissertation roadmap ……………………………………………………..31

Chapter 2 Light Propagation in Tissue and Mechanisms of Ultrasound-induced Phase Modulation on Diffuse Light ………………………...………...33

2.0 Overview ……………………………………………………………………33

2.1 Light propagation in tissue ………………………………………………..33

2.1.1 Optical absorption ……………………………………………….35

2.1.2 Optical scattering ………………………………………………..39

2.1.3 Modeling of light propagation in tissue: a brief introduction …...42

2.2 Mechanisms for ultrasound-induced modulation of diffuse light …..………..43

2.2.1 A general review of mechanisms of ultrasound-induced phase modulation ……….……………………………………………..43

2.2.2 Speckle intensity and ultrasound-induced phase modulation …...46

2.2.3 The physical significance of $C_{s,U}$ ………………………......53

2.2.4 The influence of acousto-optic-tissue properties on modulation ..54

2.2.4.1 Contribution from scatterer displacement ….…….….55

2.2.4.2 Contribution from refractive index variation ……….58

2.2.4.3 Contribution from the cross correlation between two mechanisms ……………………………………….…58

2.2.4.4 The net modulation due to the ultrasound ……….…..59

2.3 Summary ……………………………………..………………………...59

Chapter 3 Acousto-Optic Imaging System in the Near-Infrared Using the Photorefractive Effect ……………………………………..……………...62

3.0 Overview ………………………………………………………………….62

3.1 System design: the rationale for employing a 1064 nm optical wavelength ..62

3.2 Experimental arrangement ……………………...…………………...………65

3.3 System calibration ………………………………….............................69

3.3.1 Measurement of the expanded signal beam incident on sample surface……………………………………………………………....69

3.3.2 Calibration of the ultrasound transducer ………………………...70

3.3.3 Tissue-mimicking phantoms …………………………………….73

3.3.3.1 Scatterer concentration required to achieve a desired phantom $\mu_s^{'}$ ……………………...………………..75

3.3.3.2 Absorber concentration required to achieve a desired phantom μ_a ……………………………......….76

3.3.4 Principle of PRC effect and its usage for the detection of AO signals …………………………………….……………….78

3.3.5 Optimization of PRC TWM gain and diffuse light collection …..85

3.3.6 System noise characterization …………………………………...90

Chapter 4 Quantitative Measurement of Optical Properties in Diffuse Media Using Pressure Contrast Acousto-Optic Imaging ……………………...…....92

4.0 Overview ………………………………………………………………….92

4.1 Introduction ……………………………………………………………….....93

4.2 Pressure contrast AOI ……………………………………………….....96

4.3 Methods and materials ………………………………………..……..98

4.3.1 AOS strength dependence on ultrasound focal pressure ……..….98

4.3.2 The selection of ultrasound focal pressure amplitudes ………...101

4.3.3 Determination of PCS experimentally ………………………103

4.3.4 Experimental samples …………………………………………105

4.4 Experiment results ……………………………………………………108

4.4.1 Correlation between PCS and optical properties ………………108

4.4.2 Dependence of PCS on ultrasound field focus position with respect to the light illumination ……………………………………...110

4.4.3 Application of pressure contrast AOI for the detection and quantification of optical heterogeneities ………………………112

4.5 Discussion ……………………………………………………………115

4.6 Summary ………………………………………………………………...121

Chapter 5 Monitoring High Intensity Focused Ultrasound (HIFU) Treatment in Real Time Using Acousto-optic Sensing ……….……………………...122

5.0 Overview ………………………………………………………………...122

5.1 Introduction ……………………………………………………………...123

5.1.2 High intensity focused ultrasound ……………………………..123

5.1.2 Clinical monitoring of HIFU treatment ………………………124

5.1.2.1 Magnetic resonance imaging …………………………..125

5.1.2.2 Diagnostic ultrasound ……………………………………126

5.2 Acousto-optic sensing …………………………………………...……128

5.3 Materials and methods …………………………………………………..130

5.3.1 *Ex-vivo* tissue sample preparation ……………………………..132

5.3.2 HIFU exposure sub-system ……………………………………..…134

5.3.3 AO sensing sub-system ………………………………………...137

5.3.4 Passive cavitation detection ……………………………………139

5.3.5 Active cavitation detection ……………………………………….142

5.3.6 Characterization of the lesion volume ………………………....142

5.4 Experiment results ……………………………………………………144

5.5 Discussion …………………………………………………………………153

5.5.1 AO monitoring of exposures ……………………….……….153

5.5.2 AOI-guided exposures ………………………………………154

5.5.3 Limitations of lesion detection ……………………………....155

5.5.4 Influence of inertial cavitation 156

5.6 Summary ………………………………………………………………...159

Chapter 6 Summary and Conclusions ……….…………………………………...160

6.1 Objectives and goals ……………………………………………………160

6.2 AO sensing in the NIR……………………………………………………...160

6.3 AO sensing for guiding HIFU therapy …………………………….....162

6.4 Suggestions for future work ……………………………………..………163

6.4.1 Improvement of effective sensing depth ……..………………...163

6.4.2 Improvement of sensing speed and image-guidance HIFU treatments ………...164
6.4.3 Optical illumination and detection alignment ………………….165

Bibliography ……………………………………………………………………..166

Vita ……………………………………………………………………..…...186

List of Tables

Table 1.1: Definition of accuracy and efficacy criterion used in cancer diagnosis …….………………………………………………………2

Table 2.1: Parameters used for the simulations in Figure 2.8 ……….………….…...57

Table 3.1: MPE for skin exposures (10-30,000 seconds) to a laser beam (American National Standard Institute 2000)…………………………….….……65

Table 3.2: Measured acoustic properties of made phantom versus human breast tissue …………………………………...…………………………..75

Table 3.3: Parameters to perform the Mie scattering calculation …………………..75

Table 3.4: Experiment parameters for PRC TWM characterization ………………..87

Table 4.1: The optical features of phantoms used in this chapter ………….……...106

Table 5.1: HIFU exposure parameters …………………………….………………136

Table 5.2: Mean and standard deviation (STD) of durations for Group 3 exposures ………………………………………………………………………..152

List of Figures

Figure 1.1: A cyst removed during a breast biopsy showing increased vascularization. The optical contrast with respect to the surrounding normal tissue is evident [Reproduced from Ref. (Hughes *et al.* 1989)]...………...………..8

Figure 1.2: The optical imaging of an optical absorber embedded in (a) a thin tissue or transparent medium where photons experience no scattering and in (b) a thick tissue or turbid medium where photons are multiply scattered before reaching the detector………………...……………………..…………...10

Figure 1.3: Ultrasound-induced (phase) modulation of diffuse light ……………..…12

Figure 1.4: Diagram of a frequency-chirped system. TM- turbid medium (liquid); UT- ultrasound transducer; UA- ultrasound absorber; PMT- photomultiplier tube; BPF- band-pass filter; Amp- amplifier; FG1 and FG2- function generator; PA- power amplifier; TF- transformer; f_s - generated (signal) ultrasound frequency (chirped); $f_{s,z}$ - instantaneous signal ultrasound frequency at location z; f_r - reference ultrasound frequency; f_h - heterodyned signal frequency ...……………………………………...18

Figure 1.5: Diagram of the system using the CCD array-based parallel speckle modulation processing approach [From Ref. (Murray and Roy 2007)] ……………………………………………….…………...…20

Figure 2.1: A schematic showing the propagation of photons in a turbid medium 34

Figure 2.2: Optical absorption spectra of (a) water [Data from Ref. (Hale and Querry 1973)], (b) lipid [Data from Ref. (van Veen *et al.* 2004)], and (c) hemoglobin [Data from Ref. (Prahl 1999)] in the visible and NIR ranges …………………………………………………………………………37

Figure 2.3: (a) The weighted absorption spectra of major chromophores of breast tissue between 500-1100 nm; (b) Absorption spectrum of a whole breast: calculated values (solid line) using Eq. (2.4) versus measured data (squares) extracted from Ref. (Pifferi *et al.* 2004) ………………..……..38

Figure 2.4: Tissue ultrastructures affecting visible and NIR light by Mie and Rayleigh scattering [Reproduced from Ref. (Prahl 2002)] ………………………..39

Figure 2.5: A schematic of a scattering event causing the deflection of a photon …..40

Figure 2.6: The measured (Pifferi *et al.* 2004) and theoretical (Mourant *et al.* 1997; Nilsson *et al.* 1998) values for the reduced scattering spectrum of human breast tissue …………………………..……………………………..41

Figure 2.7: Ultrasound-modulation of multiply scattered light in a diffuse medium ..47

Figure 2.8: Dependence of all C terms as a function of (a) ultrasound frequency and (b) transport coefficient with parameters listed in Table 2.1. Green (squared) line is for $C_{s,d}$, blue (circled) for $C_{s,n}$, black (triangular) for $C_{s,nd}$, and red (diamond) for the net contribution $C_{s,U}$ ……..………....56

Figure 3.1: (a) Effective attenuation coefficient of human breast as a function of optical wavelength in the visible and near-infrared regime; (b) The decay of the optical field as a function of depth into the tissue for wavelengths between 600-1064 nm, weighted by the MPE level at each individual wavelength (Table 3.1) ……………………………………………….64

Figure 3.2: Schematic of the experimental setup. $\lambda/2$- half-wave plate; BS- beam splitter; M_1, M_2- mirror; BE- beam expander; WT- water tank; S- tissue-mimicking phantom or *ex vivo* tissue sample; UA- ultrasound absorbing material; L_1, L_2- lens; HV AC- high voltage AC electrical field; PRC- photorefractive crystal; BPF- band-pass filter; APD- avalanche photodiode; AF- Active filter; DAQ- data acquisition device; PC- personal computer; FG- function generator; AMP- amplifier; IMN- impedance matching network; UT- ultrasound transducer; XYZ- system coordinate (Z is the vertical axis)………………………………………………….66

Figure 3.3: Setup of measuring the expanded signal beam …………………………69

Figure 3.4: (a) Optical power as a function of blade edge position; (b) Differentiation over power distribution yields the beam shape (squares- derivative data; line- Gaussian fit) ………………………………...…………………...70

Figure 3.5: Experimental setup to calibrate the ultrasound transducer in water. MedBed Tank- a big water tank filled with degassed water; MH- membrane hydrophone (placed in the XY plane); PA- MH integrated preamplifier; Power- DC power supply for the PA (0-28 volts); OSC- oscilloscope; other abbreviations please refer to Figure 3.2 …………….71

Figure 3.6: The normalized peak pressure (a) along the ultrasound axis and (b) a function of radial distance in the focal plane …………………………....72

Figure 3.7: Response on the membrane hydrophone at the focal position when driving the HIFU transducer with different cycle numbers bursts at 1 MHz central frequency ………………………………………………………………...73

Figure 3.8: Focal pressure amplitude as a function of IMN output voltage (10 cycle pulse) …...…..…………………………………………………………....73

Figure 3.9: Setup to measure the absorption coefficient as a function of Indian ink concentration in the phantom solution (scatterers are not added) …........76

Figure 3.10: Absorption coefficient due to the Indian ink as a function of ink concentration (squares- experiment data; line- the linear fit) …………...77

Figure 3.11: The process that mediates the photorefractive effect by which the spatial distribution of optical illumination alters the refractive index grating of the photorefractive material [Modified from (Saleh and Teich 1991)] ……..79

Figure 3.12: Principle of photorefractive two-wave-mixing (TWM) effect with (a) the absence and (b) the presence of the ultrasound modulation. E_{sig} is the scattered (signal) beam collected from the diffuse sample, E_{ref} is the reference beam, $E_{sig,t}$ and $E_{ref,t}$ are the transmitted signal and reference beams through the PRC, respectively, and $E_{ref,d}$ is the reference beam energy diffracted into the direction of signal beam ……………………..80

Figure 3.13: Schematic diagram to characterize the TWM gain coefficient ………....85

Figure 3.14: TWM gain coefficient as a function (a) θ_{SR} (b) β (c) I_{ref} and (d) E_{ext}. The squares are the data when no external high voltage field is applied across the PRC and the circles correspond to the data with external high voltage field ……………………………..………………………88

Figure 3.15 (a) The relative TWM gain coefficient (Γ) and (b) enhanced signal beam intensity as a function of θ_{SR} ……………………………..…………..89

Figure 3.16 Light variance as a function of preamplified $I_{sig,t}$ ……………………....91

Figure 4.1: (a) The 2-cycle, 1MHz ultrasound pulse used to generate the AO response around the focal position; (b) The ultrasound pulse propagates along the Z direction across the phantom portion (i) without and (ii) with an optically absorbing inclusion; (c) and (d) AO signal waveforms corresponding to scenario (i) and (ii), respectively ………..………………………………94

Figure 4.2: Two AO signal waveforms generated with two different ultrasound focal pressure amplitudes (dashed curve for lower pressure, P_{f1}, and real curve for higher pressure, P_{f2}) within a diffuse phantom ($\mu_s^{'} = 5\,cm^{-1}$). Both waveforms were averaged over 10,000 times with a PRF of 1 kHz ….....97

Figure 4.3: Measured AO signal strength as a function of applied ultrasound focal pressure amplitude in a homogeneous phantom ($\mu_s^{'} = 7\,cm^{-1}$). The discrete circles are the measured data and the real line is the curve fit using the function $S = \kappa\left[1 - J_0(\beta P_f)\right]$ …………………………………….......99

Figure 4.4: Simulated PCS as a function of focal pressure amplitude pair for reduced scattering coefficient of (a) 6 cm^{-1} and (b) 7 cm^{-1}. The color bar represents the PCS value. (c) Simulated PCS contrast between small optical changes in diffusivity (7 cm^{-1} and 6 cm^{-1}) as a function of pressure amplitude pair, and in (d) the PCS contrast is plot as a function of lower pressure amplitude when the higher pressure amplitude is fixed at 1.5 MPa …………………...………………………………………………...102

Figure 4.5: (a) The user-defined pulse excited by the function generator and used for driving the ultrasound transducer. The inset shows the zoom-in of the 3-cycle sine waves at 1.0 MHz with the lower amplitude. (b) The resulting AO (averaged) scan line obtained within a homogenous phantom ($\mu_a = 0.14\,cm^{-1}$, $\mu_s^{'} = 7\,cm^{-1}$) ……………………………………….…...104

Figure 4.6: Illustration of phantoms embedded with (a) one inclusion at the center and (b) two inclusions positioned at the same Z position in the X-Z plane and separated by 15 mm along the X axis. XYZ is the system coordinate ……………………………………………………………………….……107

Figure 4.7: PCS as a function of transport coefficient in homogeneous media (Group I) or in embedded inclusions (Group II and III) ………………….………109

Figure 4.8: The schematic configuration of mechanically scanning the ultrasound transducer along the X and Z directions respectively …………………110

Figure 4.9: PCS dependence on ultrasound transducer position for (a) $\mu_s^{'} = 5\,cm^{-1}$ along the X direction, (b) $\mu_s^{'} = 5\,cm^{-1}$ along the Z direction, (c) $\mu_s^{'} = 7\,cm^{-1}$ along the X direction, and (d) $\mu_s^{'} = 7\,cm^{-1}$ along the Z direction ……………………………………………………..…111

Figure 4.10: PCS as a function of phantom position along the X direction revealing the presence and diffusivity of the embedded optical inhomogeneities …...113

Figure 4.11: An XY-plane pressure contrast AO image of an optically scattering inclusion ($\mu_a = 0.14\,cm^{-1}$, $\mu_s^{'} = 10\,cm^{-1}$) embedded in a highly diffuse phantom ($\mu_a = 0.14\,cm^{-1}$, $\mu_s^{'} = 7\,cm^{-1}$). The color bar corresponds to the measured value of mean PCS ……………………………………….114

Figure 4.12: The smoothed image of the 2-D pressure contrast AO image ………..133

Figure 4.13: (a) Calculated β from measured PCS and (b) $1 - J_0(\beta P_f)$ as a function of optical transport coefficient …………………………..…………..116

Figure 4.14: Simulated modulation depth as a function of optical transport coefficient based on the mechanisms of AO interaction discussed in Chapter 2 ….117

Figure 4.15: PCS detection of two embedded inhomogeneities in Group IV phantom with the same procedure but different numbers of repetition on PCS computation. The error bars represent the levels of standard error ……120

Figure 5.1: A schematic diagram showing the basic principle of HIFU treatment of a tumor in a target organ. By scanning the focal position of the HIFU field, a series of adjacent "lesions" can be created as shown to obtain the ablation of the whole tumor volume. Cross section of a formed necrosed region (lesion) in exercised chicken breast is shown on the right ……………..123

Figure 5.2: An example of magnetic resonance image of a lesion sample (Courtesy of Dr. Ian Rivens, Institute of Cancer Research, UK) ……………………126

Figure 5.3: B-mode ultrasound images (a) before and (b) after a 10 MPa (free field, peak-positive pressure) and 34 s HIFU exposure within an exercised chicken breast submersed in degassed water ……..................................128

Figure 5.4: A schematic of the experimental setup used in this study. XYZ- optical system coordinate (with Z as the vertical axis); VBS- variable beam splitter; BE_1, BE_2- beam expander; M_1, M_2- mirror; DUSP- Diagnostic ultrasound probe (its acoustic axis along the Z axis); WT- tank filled with degassed water; S- degassed chicken breast sample; UT_1- HIFU transducer; UT_2- ultrasound transducer for passive-cavitation detection (PCD); L_1, L_2- lens; HV AC- high voltage AC electrical field; PRC- photorefractive crystal; BPF- band-pass filter; APD- avalanche photodiode; AF- active filter; LA- lock-in amplifier; FG- function generator; Amp- power amplifier; IMN- impedance matching network; PA- preamplifier; HPF- high-pass filter; Scope- Oscilloscope; SYNC- synchronizing output; Trg- trigger signal; Ref- reference signal ……………………………………………………………….…………131

Figure 5.5: A photograph showing the arrangements of HIFU transducer, PCD transducer, diagnostic ultrasound probe, incident light beam and experiment chicken breast sample ……………………………….…132

Figure 5.6: Preparation of chicken breast sample. (a), (b): cut tissue sample in the XZ and YZ planes, respectively; (c), (d): degassed tissue sample mounted in the holder …………….………………………………………...133

Figure 5.7: The amplitude modulated sinusoidal waves with central frequency of 1.1 MHz during the HIFU exposure. The modulation frequency is 50 Hz and the duty cycle is 50% ……………………………………….…………134

Figure 5.8: An example of time-domain AO signal waveform at the APD output under a relatively low ultrasound focal pressure (1 MPa peak positive) in *ex-vivo* chicken breast. The waveform was obtained by coherently averaging over

1,000 sweeps (10-ms HIFU bursts) which took more than 20 s. No lesion was formed in this case …………………………………………...138

Figure 5.9: Schematic of PCD transducer positioning with respect to the HIFU field and incident light illumination ……………………….………..140

Figure 5.10: The PCD broadband emission obtained as a function of exposure time from two exposures. The real and dashed curves represent the scenario without and with the presence of inertial cavitation during the exposure, respectively …………………………………………………….141

Figure 5.11: A cross-section photo of a lesion produced in *ex-vivo* chicken breast by a 3300 W/cm^2 (peak intensity, 10 MPa peak pressure) and 50 s exposure. The HIFU direction was from left to right, with its focus plane 16 mm into the tissue along the X direction. (b) The photograph of the lesion with its boundary outlined by dashed black lines ………………………………143

Figure 5.12: Examples for a typical 3300 W/cm^2 (peak intensity, 10 MPa peak pressure) 40 s exposure in *ex-vivo* chicken breast: (a) non-normalized AOI amplitude as a function of exposure time; (b) PCD signal as a function of exposure time; B-mode ultrasound images acquired immediately (c) before and (d) after the exposure (the dashed box indicates the approximate location of the HIFU focus); (e) A photograph of the cross-section of the lesion generated by this exposure (HIFU field propagated from left to right, and the bar length represents 5 mm spatially) ………146

Figure 5.13: Normalized AO signal amplitude as a function of time for three HIFU exposures in one single tissue sample with the same peak intensity (3300 W/cm^2, 10 MPa peak pressure) but different durations of (a) 5 s, (b) 30 s, and (c) 40 s; (d) Photographs of the cross-sections …..……………….147

Figure 5.14: The correlation between normalized AO signal amplitude change ΔS as a function of resulting lesion volume for Group 1 (stars), and 2 (circles) exposures as well as the LSE fit for the data (line). The correlation between AO signal amplitude change and resulting lesion volume for Group 2 exposures were sorted according to the exposure parameters (b) sample source (c) and sample thickness (d). Each color symbol in (c) represents one sample cut from the same chicken breast ……………...149

Figure 5.15: The feedback method used for guiding the exposure using the measured AO response ……………………………………………………….…...151

Figure 5.16: Lesion volumes as a function of exposure duration for exposures guided by AO response (circles, with 20, 30, 40, 50 and 60% preset ΔS_p from left to right) and exposures with fixed durations (squares, with 25, 30, 40, 50, 60, and 75 s from left to right). The height of the column and the error bar represent the mean value and the standard deviation of the lesion volumes, respectively ……………………………………………………………....152

Figure 5.17: Lesion photos (a) along the focal plane and (b) in the XZ plane when the HIFU field propagated across a big blood vessel in an *ex-vivo* chicken breast sample.…………………………...….…..……………………...156

Figure 5.18: The PCD broadband emission (dashed line) as a function of time when inertial cavitation activity was detected during a HIFU exposure and an example of corresponding AO response (real line) as a function of time ……………………………………………………………….……….157

Figure 5.19: The relationship between AO signal amplitude change and lesion volume for four exposures (triangles) when inertial cavitation occurred during the exposure ……………………...158

Chapter 1

Introduction

1.0. Overview

This chapter provides an overview of the "state of the art" of imaging modalities used for the early diagnosis of breast cancer, which is followed by an in-depth review of acousto-optic imaging (AOI). The final section of this chapter discusses the research motivations and objectives, and provides an outline of this dissertation.

1.1. Overview of imaging modalities for early diagnosis of breast cancer

In 2009, approximately 200,000 women were diagnosed with breast cancer in the United States (American Cancer Society 2009). Breast cancer is the most common form of diagnosed cancer and the second leading cause of death (only exceeded by lung cancer) in American women. The mortality rate from breast cancer, however, has seen a notable reduction of 30-50% since the early 1990s, which is largely attributed to improvements in the early diagnosis of breast cancer, along with improved treatment methodologies (Webb *et al.* 2004).

The US Food and Drug Administrator (FDA) has approved numerous techniques for breast cancer diagnosis, including mammography, ultrasound, magnetic resonance imaging (MRI), positron emission tomography (PET), electrical impedance tomography (EIT) and thermography (Institute of Medicine 2001). Among these, mammography, ultrasound and MRI are the techniques that are most commonly used clinically, and thus these are discussed briefly in the following section. However, in order to assess these techniques properly, it is necessary to define the criteria used to describe the accuracy and efficacy of diagnostic procedures applied to cancer detection. Table 1.1 provides a list of the key terminology.

Table 1.1 Definition of accuracy and efficacy criterion used in cancer diagnosis

Sensitivity	Likelihood of reporting an existing cancer
Specificity	Likelihood of reporting no abnormality for a non-existing cancer
False-negative	Likelihood of missing an existing cancer
False-positive	Likelihood of reporting abnormality for a non-existing cancer

1.1.1. Mammography

Mammography uses low dose X-rays (usually around 0.7 mSv; 1 Sv=1 J/kg) to penetrate the breast which is positioned between a compression plate and a cassette plate. A large sheet of X-ray film (film mammography) or a photoconductive layer (digital mammography) records the penetrated X-rays. From that, craniocaudal and oblique images of the breast can be obtained. Depending on the attenuation of X-rays, cancerous tissues appear white in mammograms while normal (fatty) breast tissues appear dark grey or black, providing an excellent background contrast to visualize soft tissue abnormalities as well as subtle calcifications (tiny deposits of calcium in the breast that cannot be felt by palpation). Mammography has long functioned as the "gold standard" and is recommended by the American Cancer Society (ACS) as the preferred annual screening routine, together with clinical examination for women aged 40 or more (American Cancer Society 2009). However, to confirm whether or not an observed abnormality on mammography is cancerous, a small piece of tissue then needs to be removed to conduct a biopsy, which is an invasive procedure. In addition, the sensitivity of mammography in dense breast is significantly reduced due to the presence of an enhanced "white background", increasing the probability of false diagnosis in patients having denser breasts (Harper *et al.* 1981; Hindle *et al.* 1999). As a result, up to 20% of breast cancers are not discovered by mammograms in spite of their presence at the time of screening (National Cancer Institute 2009). Lastly, it should be noted that mammography utilizes ionizing radiation, albeit at a very small dose level compared to typical X-ray imaging, and repeated exposures potentially cast risk to patients.

1.1.2. Ultrasound imaging used for breast cancer diagnosis

Ultrasound imaging, also known as ultrasonography, uses an acoustic transducer to generate ultrasonic waves (sound frequency higher than 20 kHz) that reflected off tissue or organ structures (National Cancer Institute 2002). The backscattered echoes are detected by the same transducer and, by scanning the beam over a plane, one can generate a 2-D image of the target region in which the image contrast is based on both microscopic and macroscopic variations in acoustic impedance. In the context of breast cancer diagnosis, ultrasound imaging has been proven useful for differentiating liquid-filled cysts from solid masses (Jackson *et al.* 1996; Kopans 1998). This technique can also be used to characterize the extent and nature of a speculated solid mass, and has been used to help classify cancerous lesions (an abnormal change involving tissue or organ due to disease or injury) as benign or malignant, which can help to avoid biopsies (Stavros *et al.* 1995). It has been shown than under certain conditions an ultrasound examination can better identify palpable masses in denser breasts than mammography (Kolb *et al.* 2002; Berg *et al.* 2003). Furthermore, ultrasound devices are relatively inexpensive, portable, capable of offering real-time information, and do not employ ionizing radiation. That being said, ultrasound imaging lacks consistent sensitivity for certain early signs of cancer such as microcalcifications and also yield false-negative and false-positive rates which are unacceptably high (Jackson 1995; Hurd and Edge 1999; Kopans 1999; National Cancer Institute 2002). In addition, the interpretation of breast ultrasound images can be extremely subjective and operator dependent (Stavros *et al.* 1995; Flobbe *et al.* 2002; Smith and Andreopoulou 2004). As a result, ultrasound imaging is not recommended as the preferred routine breast cancer screening procedure. Rather it is considered an essential adjunct to conventional mammography, for it potentially offers improved detection sensitivity in contrast to examinations with mammography alone (Kolb *et al.* 2002).

1.1.3. Magnetic resonance imaging used for breast cancer diagnosis

Magnetic resonance imaging (MRI) (Squire and Novelline 1997) uses a powerful magnetic field to form an alignment of the nuclear magnetization of hydrogen atoms in the body, which is sequentially altered by external radio frequency (RF) fields and hence creates a rotating magnetic field. This field is detected and the resulting data processed to construct a high spatial resolution (2-3 mm) structural image of the target tissue/organ. As for breast cancer diagnosis, MRI is currently mainly used as supplement to mammography and physical examination. It has been shown that MRI of the breast is capable of detecting signs of early breast cancer with extremely high sensitivity (71-100%) in women at increased risk for breast cancer (Lehman and Schnall 2005; Peters *et al.* 2008; Dang *et al.* 2009; Marcotte-Bloch *et al.* 2009). MRI is also often used for accurately mapping out the physical extent of a lesion, including detailed structure information (Kim *et al.* 2007; Wasif *et al.* 2009), and for assessing the abnormalities that are seen with mammography/ultrasound. In addition, MRI allows for dynamic, contrast-enhanced imaging, and for distinguishing benign and malignant lesions (Kneeshaw *et al.* 2003). These studies have prompted the ACS to recommend MRI as an adjunctive screening procedure for women with an approximate lifetime risk of 20% or greater (Saslow *et al.* 2007). The greater sensitivity of MRI, however, is accompanied with variable specificities (Peters *et al.* 2008). For example, MRI cannot detect microcalcifications in the breast. Other disadvantages of this technique include the requirement of a dedicated breast surface coil (Lehman and Schnall 2005), requirement of magnetic compatibility (which is critical for patients with metal implants (Luechniger *et al.* 2004)), high cost of both the MRI system and subsidiary equipment, and the relatively long scan time, when compared to mammography and ultrasound imaging.

1.2. Biomedical optical imaging

1.2. 1. Motivation for optical imaging

The previous section outlined the most common techniques used for the early diagnosis of breast cancer. Despite the successes of these techniques there are still areas for improvement. For example, the tumors sensed by these modalities in clinics have typically grown to more than 10 mm (Kim *et al.* 2007; Marcotte-Bloch *et al.* 2009; Wasif *et al.* 2009) and might have advanced biologically. A study by Webb *et al.* (2004) showed that larger tumors were more likely to be of higher grade, which in turn reduces survival rates, according to Cummings *et al.* (1995). Therefore, new detection techniques are needed that can overcome existing limitations.

In recent years, optical imaging has received considerable attention and significant progress has been achieved in this very exciting field (Tuchin 2002). In the visible (λ=380-760 nm) and near-infrared (NIR) (λ=760-1400 nm) optical wavelength range, optical absorption in tissue is predominantly dictated by the relative concentration of water, lipids, oxy-haemoglobin (HbO_2) and deoxy-haemoglobin (Hb) (Quaresima *et al.* 1998), while optical scattering in tissue is affected by the tissue structure (cell nuclei size and concentration) and variations in the refractive index. Optical absorption is intrinsically sensitive to tissue angiogenesis (a physiological process involving the growth of new blood vessels and a fundamental sign in the transition of tumors from an inactive stage to a malignant one) as well as metabolic process (haemoglobin concentration and oxygen saturation). It has been well documented that the growth of a tumor is associated with an increase in vascularization due to the tumor's high metabolic demand, and sometimes poorer perfusion (Vaupel *et al.* 1991; Weidner *et al.* 1992; Vaupel *et al.* 1998; Rice and Quinn 2002) compared with normal tissue. The increased concentration of haemoglobin with consequentially decreased oxygen saturation (Nziachristos and Chance 2001; Leff *et al.* 2007) (as shown in Figure 1.1) augments the absorption coefficient by as much as a factor of 100 in the visible and NIR spectral range (Cubeddu *et al.* 1999), while the density increase in organelle population (nuclei, mitochondria (Mourant *et al.* 1998) as well as collagen in the extracellular matrix (Thomsen and Tatman 1998)) resulting from the proliferation of tumor cells produces an additional increase in scattering coefficient for tumors. As a result, the optical contrast between tumourous and normal tissues (Fishkin *et al.* 1997) can be as great as 200%-500% (the corresponding acoustic contrast is only a few percent). This presents an opportunity to use the changes in optical properties of tissue to identify cancerous regions. The "signatures" of a change in the optical properties can be detected earlier than indicators that affect diagnostic ultrasound such as acoustic impedance and bulk mechanical properties.

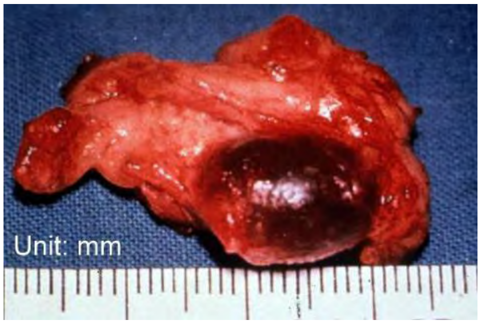

Figure 1.1 A cyst removed during a breast biopsy showing increased vascularization. The optical contrast with respect to the surrounding normal tissues is evident [Reproduced from Ref. (Hughes *et al.* 1989)].

In addition, optical imaging employs coherent laser light, which, unlike X-rays for mammography, is non-invasive, non-ionizing and thus can be used repeatedly. In comparison to MRI systems, optical imaging systems can be made relatively portable and economical. Finally, compared with ultrasound imaging for breast cancer diagnosis, optical imaging can yield quantitative measurements for objective diagnosis and follow-ups. These unique features render optical imaging a modality that has potential for positive impact on functional imaging, diagnosis and characterization of early stage cancer (Weissleder and Ntziachristos 2003).

Thus far, optical imaging has been used for near-surface imaging of structures like skin (Gladkova *et al.* 2001), retina (Podoleanu *et al.* 2000; Srinivasan *et al.* 2007) and exposed brain (Cannestra *et al.* 2000), as well as subsurface, internal imaging in large organs like breast (Colak *et al.* 1999) and unopened brain (Bluestone *et al.* 2001). For example, Chance *et al.* reported the use of an optical technique, referred to as near infrared spectroscopy, for the diagnosis of breast cancer in 116 patients, yielding sensitivity and specificity of 96% and 93%, respectively (Chance *et al.* 2005).

1.2. 2. Near-surface optical imaging

In terms of imaging depth and spatial resolution, optical imaging methods today can be categorized into two groups.

The first group is near-surface tissue optical imaging, such as time-gated optical imaging (Selb *et al.* 2006), optical microscopy (Betzig *et al.* 1991) and optical coherence optical tomography (OCT, Huang *et al.* 1991; Fercher *et al.* 2003), where photons incident on tissue experience no scattering and propagate in straight paths (like X-ray photons), enabling spatial resolution on the order of microns (Povazay *et al.* 2002) (Figure 1.2a). However, as photons travel deeper into tissue, the number of ballistic photons decays exponentially with depth due to the highly diffusive nature (strong scattering) of light in tissue. Eventually, the imaging depth of these approaches is limited to on the order of one optical mean free path length, or around 1 mm (corresponding to a 10 cm^{-1} scattering coefficient) in soft biological tissues at visible and NIR wavelengths, which is not suitable for applications in large organs like breast.

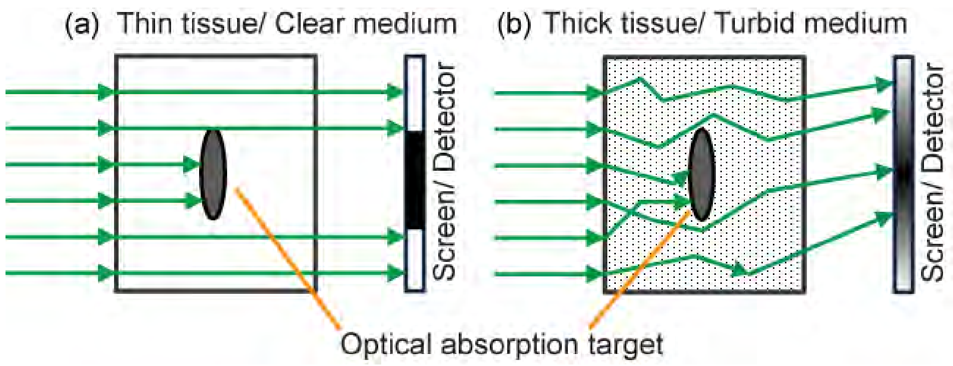
(a) Thin tissue/ Clear medium
(b) Thick tissue/ Turbid medium
Screen/ Detector
Screen/ Detector
Optical absorption target

Figure 1.2 The optical imaging of an optical absorber embedded in (a) a thin tissue or transparent medium where photons experience no scattering and in (b) a thick tissue or turbid medium where photons are multiply scattered before reaching the detector.

1.2. 3. Subsurface optical imaging

The second group refers to subsurface optical imaging, such as diffuse optical tomography (DOT, Yodh and Chance 1997; Boas *et al.* 2001), where photons penetrate into tissue beyond the optical mean free path up to a depth of several centimeters. These photons undergo multiple scattering events, following “random walks” in the tissue, and the observed image of the embedded absorber based on the transmitted photons sensed by the detectors outside of the tissue is blurred (Figure 1.2b). In order to invert that data and reconstruct the target image from the blurred detected image, one employs a theoretical propagation model based on a diffusion equation, rather than a wave equation (Arridge and Schotland 2009). The resulting image quality is generally dependent on the algorithm used and the spatial resolution is limited to a minimum of 5 mm with a depth penetration of several centimeters (Boas *et al.* 2001).

1.2. 4. Multimode imaging and dual-wave imaging

To help overcome the loss of spatial resolution due to strong light diffusivity when using optical imaging alone, one can combine optics with structure specific imaging modalities like X-ray imaging (Li *et al.* 2003a), MRI (Nziachristos *et al.* 2002) and diagnostic ultrasound imaging (Zhu *et al.* 2003). These multimodality images provide internal morphology and structure information at a spatial resolution determined by those established imaging modalities coupled to complementary quantitative mapping of optical properties and functional information (Demos *et al.* 2006). Dual-wave imaging techniques such as Acousto-optic imaging[1] (also called ultrasound-modulated optical tomography) (Wang 2004; Murray and Roy 2007) and photoacoustic tomography (also called opto-acoustic or thermo-acoustic tomography) (Xu and Wang 2006; Li and Wang 2009), combine ultrasound with light, taking the advantage of contrast provided by pure optics and the spatial resolution of ultrasound.

1.3. Acousto-optic imaging

1.3.1. Introduction

Acousto-optic imaging (AOI) is a dual-wave modality that uses ultrasound waves to modulate the propagation of diffuse light in an effort to image the optical contrast deep within turbid media with a spatial resolution (millimeter or even sub-millimeter) dictated by the ultrasound field (frequency, beam size) used (Dolfi and Micheron 1989; Marks *et al.* 1993; Brooksby and Penny 1995; Leutz and Maret 1995; Wang *et al.* 1995). This technique is also referred to as ultrasound-modulated optical tomography (UMOT, Wang 1996), ultrasound tagging of light (UTL, Marks *et al.* 1993; Mahan *et al.* 1998), acousto-optic tomography (AOT, Kempe *et al.* 1997; Forget *et al.* 2003) and acousto-photonic imaging (API, Stott *et al.* 2000).

---

[1] Acousto-optic imaging sometimes is also implemented in clear media, but in this dissertation, unless otherwise stated, it is limited to investigations in diffuse media.

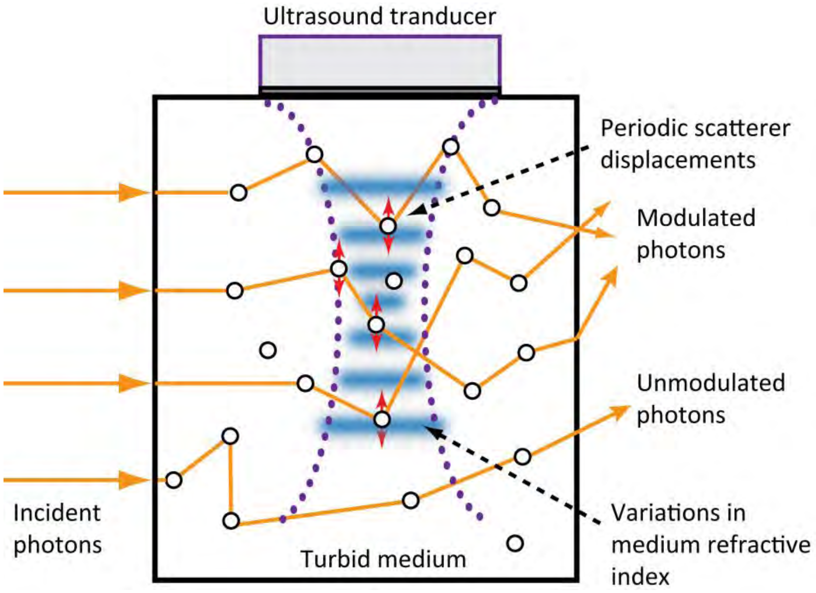
Ultrasound tranducer
Periodic scatterer displacements
Modulated photons
Unmodulated photons
Incident photons
Turbid medium
Variations in medium refractive index

Figure 1.3 Ultrasound-induced (phase) modulation of diffuse light.

Figure 1.3 demonstrates the principle of AOI in a turbid medium. The sample under examination is exposed to continuous wave (CW) or pulsed, light and sound simultaneously. The individual photons experience a sequence of scattering events in the sample, with the averaging distance between consecutive events given by the scattering mean free path (reciprocal of optical scattering coefficient). The resulting optical field in the turbid medium can be treated as a composition of numerous partial waves (Murray and Roy 2007), with each of these partial waves following a unique optical path. Individual photons that are propagating along each of these paths can be either absorbed or scattered in the tissue. Under moderate ultrasound peak pressure (e.g. 0.3-1.5 MPa at 1.0 MHz), the scattering sites within the ultrasound field are periodically displaced along the ultrasound propagation direction, causing a periodic disturbance in the optical path length. Eventually the partial wave experiences a phase shift that is accumulated over different scattering events along that optical path traversing the ultrasound field with respect to those traveling in the absence of ultrasound influence. In addition, periodic variations in optical index of refraction caused by the pressure field also perturb the effective optical path length, which in turn periodically shifts the phase of the partial wave. These two mechanisms (Marks *et al.* 1993; Leutz and Maret 1995; Wang 2001) along with the correlation between them (Sakadzic and Wang 2005) result in a net cumulative phase shift of the light propagating through the acousto-optic (AO) interaction volume, defined as the region where light and sound coexist. We refer to this process as ultrasound modulation (or "tagging") of diffuse light, and the strength of this modulation is influenced the optical properties of medium within the AO interaction volume. More details on this topic will be given in Chapter 2.

By employing appropriate light detection and processing schemes, a signal that is related to both the intensity of the ultrasound modulation of light and the average phase shift of the modulated partial waves, termed the acousto-optic signal (AOS), can be extracted. This parameter can then be used to infer the spatially-averaged optical properties of the AO interaction volume (Murray *et al.* 2004; Ramaz *et al.* 2004;

Sakadzic and Wang 2004; Xu *et al.* 2007; Li *et al.* 2008b; Rousseau *et al.* 2008; Lai *et al.* 2009a). Since the modulation is only generated within the interaction volume, the spatial resolution of AOS is therefore dictated by the dimensions of this volume. Since the optical beams incident on tissue are normally expanded (Tomlinson and Tiemann 1992; Marks *et al.* 1993; Sui *et al.* 2005) and hence have much broader (diffuse) illumination pattern in the sample with respect to the ultrasound beam, the detection spatial resolution for optically diffuse media is determined by the ultrasound beam. Using the megahertz-frequency, tightly focused, short-pulse insonation parameters normally employed in clinical diagnostic ultrasound imaging, millimeter or submillimeter resolution can be achieved (Murray *et al.* 2004; Kothapalli and Wang 2008). By steering the ultrasound beam with respect to the sample that is optically illuminated throughout, a 2D or 3D image of the sample can be obtained with relatively straightforward image reconstructive methods (Marks *et al.* 1993).

It should be noted that AOI technology is still in its infancy, and to achieve widespread clinical applications, further advancements are required. The key challenge is to increase the signal-to-noise ratio (SNR) of the system. Poor SNR in AO sensing arises from the fact that only the light traversing through the AO interaction region is modulated by the ultrasound field. For a given exposure light level permitted by the American National Standards Institute (ANSI) (American National Standards Institute 2000), the flux of photons that is tagged and ultimately collected outside of the sample is extremely low due to the strong attenuation of light in the tissue. Furthermore, the “tagged” photons are typically detected against a much stronger background of unmodulated light. Indeed, the modulated light can account for less than 1% of the total light collected outside of the sample (Leveqe-Fort *et al.* 1999). This effect is particularly critical when tightly focused, short pulses of ultrasound are used to generate the AO interaction at deeper depth. Moreover, the collected photons propagate over various optical paths from the source to the detection system. The interference among individual paths causes the resulting intensity to be anywhere from full brightness to full darkness, depending on the relative de-phasing between paths. This leads to the formation of a speckle pattern where individual speckles are phase modulated at the ultrasound frequency, with the modulation being dependent on the specific path that a photon travels and the spatial position where the AO interaction occurs. Therefore the modulation of individual speckle grains is spatial incoherent, *i.e.* the phase of the modulated signal is random from speckle to speckle. This leads to a predicament where, when using a small aperture detector that is restricted to detecting a single speckle, one is left with the detection of a relatively small intensity modulation on an exceedingly weak signal; if the aperture is increased so as to receive multiple speckle grains, the overall intensity of modulated light is enhanced but at the expense of reduced modulation efficiency due to the random phase among speckles.

1.3.2. The historical development of acousto-optic (AO) sensing and imaging [2]

The concept of using ultrasound to mark or "tag" the diffuse light was first proposed by Dolfi and Micheron in 1989. Their aim was to use this technique to improve the spatial resolution of optical imaging, but this proved difficult to realize experimentally due to the low flux of modulated photons. Tomlinson and Tiemann (1992) later proposed a modification of this photon localization concept, suggesting that using a 2D optical detector array with each pixel matched to a speckle would help to enhance the detection SNR, and enable the sensing of the local optical absorption contrast through the changes in speckle intensities generated by a short ultrasound pulse. However, no experimental results were reported in their work.

---

[2] Only experimental work is referred to here. Theoretical studies are in Chapter 2.

In 1993, Mark *et al.* first demonstrated experimentally the feasibility of employing short-pulsed ultrasound to interact with diffuse light in an optically homogeneous tissue-mimicking (liquid) phantom. A weak, but measurable time-domain intensity modulation was detected at temporal positions corresponding to the focal region of the ultrasound beam, even though coherent averages of 131,072 scans were required to achieve even minimal SNR (Dolfi and Micheron 1989). Shortly afterwards, researchers shifted their focus to developing an understanding of the origins of the modulated signals. Brooksby and Penny (1995) demonstrated through experiment that it was the diffuse, not the ballistic, light that was modulated by the ultrasound field. They also showed that the AOS strength decreased with increasing medium diffusivity. Leutz and Maret (1995) observed sidebands (shifted by the ultrasound frequency) in the frequency spectrum of modulated scattered light, from which they extracted a modulated signal that had a quadratic dependence on ultrasound pressure amplitude.

After the mid 1990's, the utility of using the "ultrasound tagging" of diffuse light to image the absorption contrast embedded in turbid media was demonstrated. Wang *et al.* (1995) employed a focused CW ultrasound source to generate the AO response. The use of CW ultrasound field allowed for narrow-band detection schemes. The CW ultrasound-induced frequency sidebands in light intensity spectrum were very narrowband and tuned to the ultrasound fundamental and first several harmonic frequencies, whereas for pulsed ultrasound these sidebands were significantly broader (corresponding to the inverse of the ultrasound pulse temporal duration). Additionally, the use of a CW ultrasound field enlarged the volume of AO interaction, yielding more photons tagged by the ultrasound and hence increasing the strength of AOS. As a result, considerable improvement in SNR was obtained, and averaging over only 256 frequency sweeps produced adequate SNR. It was found that the strength of the AOS was greatly decreased when the focus of the ultrasound beam intersected the absorbing target, demonstrating that the relative AOS strength was related to the local optical properties and *in situ* ultrasound pressure amplitude within the AO interaction region. Therefore, by physically scanning the experimental sample in a plane perpendicular to the optical propagation direction and measuring the strength of AOS at each position, one was able to create a 2-D optical image of an absorbing target (glass bead and rubber) embedded in a liquid tissue phantom. The lateral spatial resolution was dictated by the off-axis focal spot size of the ultrasound beam. By keeping the sample fixed and instead moving the position of the single element photodetector (PMT) off the optical axis, the same group confirmed (Wang and Zhao 1997) that the AO images generated were based on diffuse light, as opposed to ballistic light.

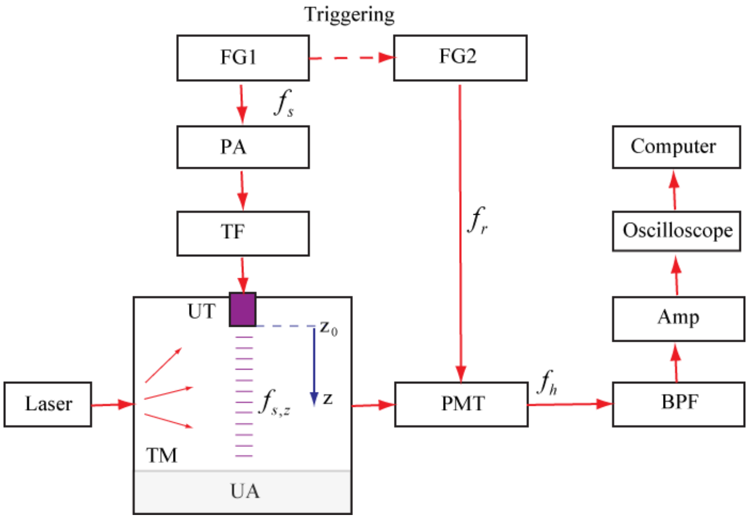

Figure 1.4 Diagram of a frequency-chirped system. TM- turbid medium (liquid); UT- ultrasound transducer; UA- ultrasound absorber; PMT- photomultiplier tube; BPF- band-pass filter; Amp- amplifier; FG1 and FG2- function generator; PA- power amplifier; TF- transformer; f_s - generated (signal) ultrasound frequency (chirped); $f_{s,z}$ - instantaneous signal ultrasound frequency at location z; f_r - reference ultrasound frequency; f_h - heterodyned signal frequency.

The use of a CW ultrasound beam, on the other hand, generated AO interaction throughout the volume of ultrasound field (assuming this volume was completely optically illuminated), which severely limited the spatial resolution along the ultrasound axis. To achieve axial resolution from CW ultrasound exposures, the CW ultrasound source may be frequency "chirped" over a time frame comparable to the ultrasound propagation time through the region of the interest (Wang and Ku 1998; Ku *et al.* 1999) using a scheme shown in Figure 1.4. A frequency chirped signal ($f_s(t) = a_s + bt$, where a_s was the starting frequency and b was the sweeping rate), which was amplified and used to drive the ultrasound transducer placed at z_0. The instantaneous frequency of the ultrasonic modulation at location z therefore could be expressed as: $f_{s,z}(t) = a_s + b(t - \frac{z - z_0}{c_s})$, where c_s was the sound speed in the medium. The scattered light was collected with a PMT, whose gain was modulated for heterodyned detection by a reference signal that was also frequency chirped ($f_r(t) = a_r + bt$, where a_r was the starting frequency of sweeping and different from a_s) and then further processed. The frequency of the heterodyne signal caused by the ultrasound modulation at location z was thus given by $f_{h,z}(t) = \left| f_{s,z}(t) - f_r(t) \right| = \left| a_s - a_r - \frac{b(z - z_0)}{c_s} \right|$, suggesting a specific component in the frequency spectrum of the detected heterodyned signal corresponded to one particular distance from the transducer along the ultrasonic axis. In this way, a 1-D scan along the acoustic axis can be obtained from the time-dependent frequency-domain information, and the resolution is adjustable by altering the bandwidth of the frequency sweep.

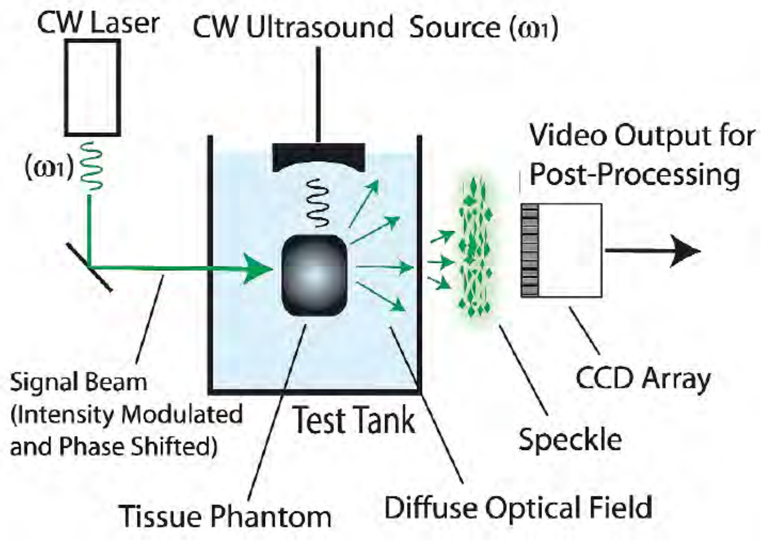
CW Laser
CW Ultrasound Source (ω1)
(ω1)
Video Output for Post-Processing
Signal Beam (Intensity Modulated and Phase Shifted)
Test Tank
CCD Array
Speckle
Tissue Phantom
Diffuse Optical Field

Figure 1.5 Diagram of the system using the CCD array-based parallel speckle modulation processing approach [From Ref. (Murray and Roy 2007)]

In the studies that were previously discussed, single-aperture optical detectors were employed. This had the advantaged of fast response, but also resulted in extremely low light levels if the detector aperture was limited to single or few speckle detection, or in reduced modulation efficiency if the detection aperture was increased to encompass multiple speckles. A study by Leveque *et al.* (1999) developed an array-based parallel speckle detection system (Figure 1.5) in an effort to improve upon the single aperture detector approach. They used a 2-D charge-coupled device (CCD) array with one or a few coherent speckle grains mapped to each pixel of the array. Since the speckle modulation frequency followed the frequency of applied ultrasound field which, being greater than 1 MHz, greatly exceeded the frame rate of a CCD array (200 Hz for the array used in their work), the authors employed a parallel lock-in detection scheme. The laser source was modulated at 2.2 MHz (ω_1 in Figure 1.5, which was the frequency of ultrasound) with a fixed relative phase delay with respect to the ultrasound. The 2-D CCD array functioned as a low-pass filter (50 Hz working bandwidth) and at each pixel four images of the speckle grain were recorded per ultrasound cycle, each corresponding to the modulation during one quarter of the ultrasound period. By computing the linear combination of these four images, one was able to extract the amplitude and phase of the modulation at each pixel. The sum of amplitudes from individual pixels gives the overall AO response. This method allowed for the coherent summation of signals over different speckle grains, yielding an improvement of SNR on the order of $\sqrt{N}$, where N is the number of pixels of the CCD array.

It was shown, however, this parallel detection scheme was sensitive to the speckle decorrelation from environmental vibration and the relatively long time for imaging acquisition. Gross *et al.* (2003) later employed a digital holographic technique (Mach-Zehnder interferometer) to isolate the detected AO signals, combined with a spatial filter system (aperture outside of the sample) to reduce the speckle decorrelation noise caused by environmental sources like room vibrations. To achieve acoustical axial resolution with enhanced sensitivity, Yao *et al.* (2000; Yao and Wang 2000), Forget *et al.* (2003) and Atlan *et al.* (2003) integrated the frequency-chirped ultrasound technique with the CCD-based parallel detection. Specifically, Atlan *et al.* (2005) combined heterodyned detection with this CCD-based parallel detection scheme and a pulsed ultrasound field, resulting in an AO sensing system with improved SNR and spatial resolution along the ultrasound axis.

The developments described above allowed for a significant increase in SNR and a compatibility with different types of ultrasound exposure schemes. The CCD array-based parallel detection scheme, along with its modifications (including using CMOS in place of CCD array (Bossy *et al.* 2007)), were once regarded as "the most efficient technique for ultrasound-modulated optical tomography" (Li and Wang 2002) and have seen widespread use (Leveqe-Fort 2000; Selb *et al.* 2001; Li *et al.* 2002; Li and Wang 2002; Selb *et al.* 2002; Li *et al.* 2003b; Li and Wang 2004; Kim *et al.* 2006; Kim and Wang 2007; Kothapalli *et al.* 2007; Zemp *et al.* 2007; Kim *et al.* 2008; Daoudi *et al.* 2009), and not solely for optical imaging. Using low frequency transient acoustic radiation force (TARF) generated by the intense acoustic bursts (around 1-2 ms in duration), Bossy *et al.* (2007) observed AO sensing based on mechanical (stiffness) contrast. Kim *et al.* (2007) demonstrated the feasibility of using a multiple-optical-wavelength light source to determine both the total dye concentration and the ratio of blue dye to red dye in a phantom, a technique which could potentially be used for optical functional imaging in tissue. Kothapalli *et al.* (2007) demonstrated the capability of AOI to detect optically scattering (as opposed to optically absorbing) targets embedded in diffuse media.

It is important to point out that the speckle decorrelation time associated with physiological motion is on the order of 0.1-1 ms at a depth of 4 cm for *in-vivo* breast (Gross *et al.* 2009). This then requires the imaging acquisition speed (typically limited by the effective frame rate of the CCD array in aforementioned systems) to be at least several kilohertz. Unfortunately most CCD cameras do not have this ability, thus limiting the practicality of this technique. The time required to transfer the enormous amount of data from the array could further compromise the ability to do real time sensing and imaging (Ramaz *et al.* 2004).

As mentioned previously, a CW ultrasound field affords enhanced AO SNR and noise immunity. If the issues with system SNR could be resolved, pulsed ultrasound is preferred since it allows for resolution along the acoustic axis. Moreover, pulsed ultrasound allows for the use of a higher focal pressure amplitude without inducing deleterious thermal bioeffects. Indeed the Food and Drug Administration (FDA) exposure limitations associated with mechanical bioeffects (cavitation) for clinical applications are not violated unless the mechanical index (MI) of the exposure exceeds 1.9 (US Food and Drug Administration 1997), which corresponds to a derated peak-negative acoustic pressure amplitude of 4.25 MPa at a typical imaging frequency of 5 MHz. Since the AO response is quadratic with pressure amplitude, the greater pressure amplitudes normally used in pulsed ultrasound systems allow for improved SNR. In addition, single aperture optical detectors can respond much faster (MHz-GHz order sampling rate) than CCD cameras. If multiple speckle grains could be sensed and summed coherently with one large aperture photodetector without reducing the modulation efficiency, a substantial enhancement in sensitivity and SNR would result.

Photorefractive crystal (PRC)-based interferometry systems have seen widespread use for the optical detection of high frequency vibrations from optically rough surfaces in two-wave-mixing (TWM) (Delaye *et al.* 1997) or four-wave-mixing (FWM) (Hale and Telschow 1996) schemes. In 2004, a PRC-based interferometry system was introduced by Murray *et al*. for the detection of ultrasound-modulated light in diffuse media (Murray *et al.* 2004). By taking advantage of the photorefractive effect (which will be discussed in detail in Chapter 3), the coherent summation of modulated signals from a large number of speckle grains was made possible using a large aperture (10 mm diameter) detector. It was demonstrated that the sensitivity of this approach was sufficient to detect the transient modulated optical signals generated by a pulsed ultrasound source operating at pressures significantly lower that normally used in diagnostic ultrasound imaging; Murray employed 0.65-1 MPa at 1 MHz central frequency. One dimensional images of absorbing targets (5x6x5 mm^3) embedded at a depth of 2-3 cm in tissue mimicking phantoms or *ex-vivo* chicken breast were obtained using time-domain signal averaging (over 1,000-10,000 sweeps for desired SNR). The axial resolution was determined by the acoustic pulse spatial length, which was typically 5-10 cycles. Two- and three-dimensional maps of the optical absorption contrast were also obtained by scanning the ultrasound source with respect to the region of interests (Murray *et al.* 2004; Sui *et al.* 2005; Sui *et al.* 2006).

The use of short ultrasound pulses further motivated a direct integration of this AO sensing approach with a commercial ultrasound imaging machine (AN2300, Analogic Corp., MA, USA), in which the same scan probe was used to *both* pump both B-mode ultrasound imaging and the light modulation. The two types of images could then be automatically co-registered and displayed, yielding the mechanical and optical properties of *ex-vivo* chicken breast and tissue-mimicking phantoms (Bossy *et al.* 2005a; Bossy *et al.* 2005b). This approach demonstrated that AOI could serve as one component of a multi-mode acoustical/optical imaging scheme, and thus supplement existing ultrasound diagnostic modalities such as B-mode and Doppler with additional optical information. For example, the integrated system could be used for breast cancer diagnosis where B-mode ultrasound could image the tumor while a single AO A-line could be launched across the tumor region to assess or monitor the changes in local optical properties (Murray and Roy 2007). The latter could then be used to assess tumor vascularity, blood oxygenation, etc.

Compared with previously developed detection schemes, PRC-based detection allows for high etendue (light collection efficiency, defined by the product of area surface and acceptance solid angle; see more details in Chapter 3), and a fast, larger aperture, single-element photodetector, and thus "the possibility (of observing) signals in real time" (Lesaffre *et al.* 2007). Ramaz *et al.* (2004) also reported a PRC-based detection technique that employed CW ultrasound and a scheme where frequency shifted light was added to both the signal beam and reference beam using acousto-optic modulators (AOM, also referred to as Bragg cell, uses the acousto-optic effect[3] to diffract and shift the frequency of light using acoustic waves). This allowed them to selectively detect the modulated or unmodulated photons. Considering that only approximately 1% of total light collected is "tagged" by the ultrasound field in AOI (Leveqe-Fort *et al.* 1999), selectively detecting only the modulated photons is critical to the reduction of the background noise.

---

[3] This is related to the acousto-optic effect in clear medium mentioned in Footnote 1 on page 11, not the one studied in this work.

Blonigen *et al.* (2005), Gross *et al.* (2005; 2009) and Lesaffre *et al.* (2007) further studied theoretically the principles of PRC-based interferometry in the context of AO sensing. The latter groups also characterized the response time of the crystal as function of light intensity shed on material surface, showing the response time constant of a GaAs crystal can be reduced to less than 200 µs (Gross *et al.* 2009), making it fast enough to overcome the speckle decorrelation effect *in vivo*. Currently PRC-based schemes are used for applications beyond conventional sensing/imaging of optical contrast, such as detecting mechanical stiffness contrast caused by TARF response to millisecond long ultrasound bursts (Xu *et al.* 2007). Despite these advantages, the deployment of a PRC-based scheme for detecting diffused light is ultimately limited by (1) PRC etendue and TWM gain, and (2) the relatively strong reference beam tends to scatter into the aperture of the detector, which increases the system noise (Li *et al.* 2008b).

In 2004, Sakadzic, and Wang employed a long cavity confocal Fabry-Perot interferometer (CFPI)-based detection scheme to obtain high resolution AO signals (Sakadzic and Wang 2004). This scheme is suitable for various wavelengths in the optical therapeutic window. It has a greater etendue than most of CCD-based parallel detection setups and can be set to selectively transmit photons modulated by the ultrasound pulses in real time while tolerating speckle decorrelation due to the environment vibration or physiological motion of the body (Kothapalli and Wang 2008). However, it should be noted that the long cavity length (e.g., 0.5-1 m) results in a relatively small acceptance angle for light collection which in turn limits the system etendue. This approach was proposed for imaging subsurface blood vasculature (2-3 mm deep) with micron-scale resolution (Kothapalli and Wang 2009). More recently, it was incorporated with a high-peak-power short pulsed laser source (Rousseau *et al.* 2009), providing sufficient SNR for imaging a 3x3x3 mm^3 absorbing inclusion embedded in (a) a 3 cm thick phantom without signal averaging, and (b) a 6 cm thick *ex-vivo* chicken breast with signal averaging over only 128 lines.

In 2008, a new detection scheme based on a spectral-hole burning crystal (SHBC) was introduced for the detection of AO signals (Li *et al.* 2008a; Li *et al.* 2008b). The SHBC technique uses a narrowband absorptive filter in the frequency domain that transmitted one frequency sideband of modulated signals but efficiently blocked the unmodulated background and the other sidebands. Preliminary results indicate that this technique affords the largest etendue among the existing AO detection approaches (Li *et al.* 2008b) and its fast response time makes the system inherently insensitive to fast speckle decorrelation, thus potentially allowing for *in vivo* imaging in biological tissues.

In summary, PRC-, CFPI- and SHBC-based schemes are, at present, the most suitable choices for real-time AO detection *in vivo*. Yet, to date, the majority of AO sensing and imaging studies have been performed in tissue-mimicking phantoms or *ex-vivo* tissue samples possessing thicknesses usually less than 40 mm, while clinically applications generally requires explored depths exceeding 50 mm. The critical limitation of AO sensing is the imaging depth attainable given clinically permissible optical and acoustical exposure parameters. However, given recent progress in increasing sensing SNR and penetration depth using pulsed lasers with high peak intensity (1.3 kW) but low duty cycle (<0.3%) (Rousseau *et al.* 2008; Rousseau *et al.* 2009) along with the adoption of fast, efficient demodulators, it is very likely that deeper and real-time deep-tissue AO sensing *in vivo* will soon become a reality.

1.4. Motivation and focus of the work

1.4.1. Understanding the nature of ultrasound-induced modulation on diffuse light

Two mechanisms are believed to generate the phase modulation of diffuse light due to the ultrasound, i.e., periodic scatterer displacement and refractive index variation. In the majority of previous studies, these two effects were treated independently, while assuming no relationship between them. According to these theories, the modulation induced by both mechanisms should increase as the number of scattering events along the optical path increases (i.e. with increasing diffusivity). However, this is contracted by observed experimental results indicating a *reduction* in the modulation depth with increased medium scattering coefficient (Kothapalli *et al.* 2007; Lai *et al.* 2009b; Lai *et al.* 2009a). Building on work from Sakadzic and Wang (2005), we perform an analytical study of the mechanisms of AO interaction starting from the ultrasound-induced phase perturbations in the medium to the corresponding electrical field associated with a single speckle. The influences of acoustical and optical tissue properties on the ultrasound modulation are also investigated, yielding simulation results in agreement with experiment measurements.

1.4.2. Development of a near-infrared (NIR) AOI system

The previous AOI system employed in our laboratory (Sui 2005) achieved a balance between imaging sensitivity and axial resolution using a BSO photorefractive crystal-based scheme, operating at the optical wavelength of 532 nm. However, this system was limited (1) in imaging depth in biological tissues due to high optical effective attenuation coefficient and low optical maximum permissible exposure (MPE) at this wavelength, and (2) in the relatively slow photorefractive response time of a BSO crystal, which was not fast enough to compensate for the environmental vibration and physiological motion *in vivo* (Gross *et al.* 2009). To overcome these challenges, the system was redesigned to operate at 1064 nm, which results in a smaller optical attenuation coefficient and higher MPE in tissue. Moreover, we employed a GaAs PRC capable of offering faster response. The new system was set up, characterized and optimized for the detection of AOI signals in terms of SNR.

1.4.3. Quantitative measurement of local optical properties with AOI

Acousto-optic measurement of quantitative absorption and/or scattering in non-homogeneous media is a challenge that requires an inversion algorithm similar to that employed for diffuse optical tomography. This is due, in large part, to the spatial variability of the illuminating light flux incident on the interaction volume. Motivated by this, we developed a new approach which we refer to as pressure contrast AOI (Lai *et al.* 2009a; Lai *et al.* 2009b). The NIR AOI system is used to measure the AO signals generated by insonifying tissue phantoms with successive, short-duration ultrasound pulses at two different pressure amplitudes. The ratio of the two detected signals is directly related to the optical properties of the target region, independent of the local illuminating light level. It is also demonstrated experimentally that it is feasible to both measure and image the optical properties of embedded optical inclusion, as well as the background medium.

1.4.4. Real time monitoring of HIFU therapy using AO sensing

High intensity focused ultrasound (HIFU) is an important noninvasive tool for targeted tissue ablation and has been successfully used to thermally ablate solid tumors (ter Haar 1995) as well as to promote haemeostasis (Vaezy *et al.* 1998), thrombolysis (Rosenschein *et al.* 2000) and drug/gene delivery (Porter and Xie 2001; Ng and Liu 2002). The ability to monitor and assess HIFU treatment outcomes is essential owing to complex variations in tissue acoustical and thermodynamic properties as well as the mitigating effects of tissue variability in the near field propagation path of the therapy transducer. There is a need for both post treatment imaging techniques for assessing the location, size and shape of the HIFU-induced lesion and real-time monitoring techniques that ensure that a thermally necrosed volume of a desired extent is created, while damage to the surrounding healthy tissue is minimized. This can be achieved with MRI (Gianfelice *et al.* 2003), albeit at great expense. The use of ultrasound imaging (Wu *et al.* 2004; Illing and Chapman 2007) has proven ineffective at sensing purely-thermal lesions as the ultrasound contrast with surrounding tissue is low. However, boiling lesions resulting from overtreatment can be readily detected.

In this study, the NIR AOI system is used (Lai *et al.* 2010) to sense the changes in optical contrast at depth in *ex-vivo* tissue that are associated with the onset, formation and the development of a necrosed region (referred to as a "lesion" in our study). It is found that when a thermal lesion forms in the ultrasound focal zone, the AO signal diminishes in amplitude owing to enhanced optical attenuation, whereas traditional B-mode ultrasound images reveal no change. It is further shown that the reduction of AO signal during an HIFU exposure is correlated with the spatial volume of the ensuing lesion, suggesting that the evolution of AO signal amplitude could be used as a means to predict and monitor and the HIFU treatment processes. Experiments also verified the feasibility of using the observed AO signal change as the criterion to guide the HIFU exposures in real time, achieving improved consistency and repeatability in resulting lesion volumes.

1.5. Dissertation roadmap

The present Chapter presents the background, motivation and focus of the research as well as the roadmap for the Dissertation. A literature review of optical tissue imaging in general, and AO sensing and imaging in particular, was presented in Chapter 1. In Chapter 2, the fundamentals of light interaction with tissue and the nature of acousto-optic interaction in turbid media are discussed, along with relevant theory. Chapter 3 explains the rationale for the transition from our previous 532 nm system to the NIR (1064 nm) arrangement. The design, development, and characterization of this system is discussed. In Chapter 4, we propose a new sensing mechanism, termed "pressure contrast AOI," for the quantitative measurement of local optical properties in diffuse media based on the ratio of two AO signals pumped by two acoustic pressure amplitudes. The feasibility and potential applications of this approach are demonstrated through experiments in tissue-mimicking phantoms. In Chapter 5, the use of the NIR AOI system for monitoring and guiding the HIFU treatment processes in real time is explored, yielding promising experimental outcomes. A summary of work done, conclusions drawn, and suggestions for future study are presented in Chapter 6.

Chapter 2

Light Propagation in Tissue and Mechanisms of Ultrasound-induced Phase Modulation of Diffuse Light

2. 0. Overview

This chapter outlines the theory of light propagation in tissue and ultrasound-induced phase modulation of diffuse light relevant to the research described in this Thesis. The physical principles that govern the interaction of photons with tissue are described in Section 2.1. In Section 2.2 the mechanism of ultrasound-induced phase modulation on diffuse light is discussed and an analytical model, which incorporates ultrasound-induced periodic displacement of scatterers and variations in refractive index, is described.

2. 1. Light propagation in tissue

In turbid media (e.g. biological tissue), optical absorption and scattering are the major phenomena affecting the propagation of light, and they arise from the interaction between incident photons and molecules of the tissue components (Saleh and Teich 1991).

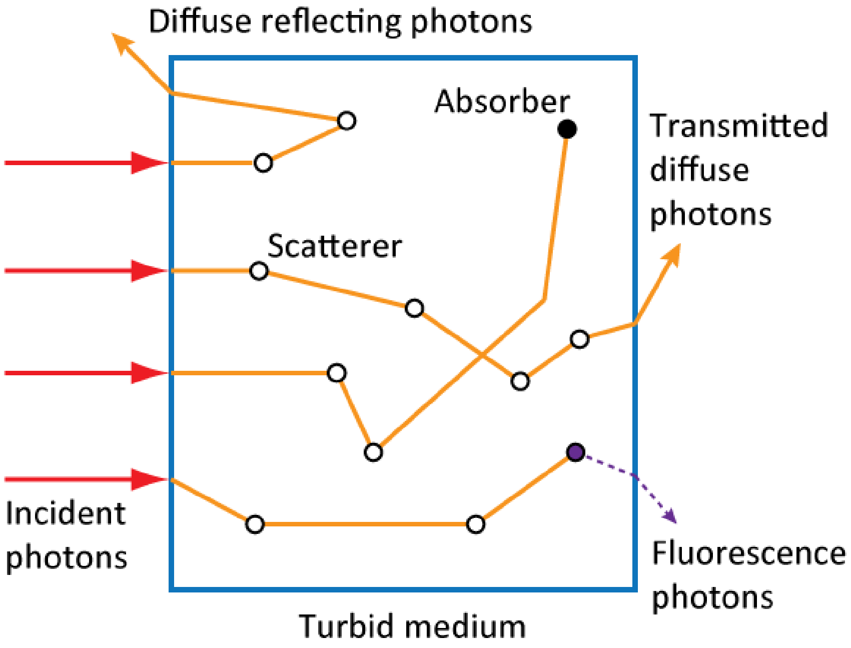
Diffuse reflecting photons
Absorber
Transmitted diffuse photons
Scatterer
Incident photons
Fluorescence photons
Turbid medium

Figure 2.1 A schematic showing the propagation of photons in a turbid medium.

Figure 2.1 is an example depicting light propagation in a turbid medium. When photons are incident on tissue or tissue-like media, a large number of scattering events may take place due to the interactions between photons and cell constituents, tissue fibers, intercellular structures, organelles in the cells and the other structural inhomogeneities. Meanwhile, the photons may be absorbed by "absorbers" (various chromophores) such as water, hemoglobin and melanin, *etc*. As a result, coherent, collimated photons are either transmitted as diffuse photons, totally absorbed inside the tissue, re-emitted as diffuse reflectance, or transformed into fluorescence signals. For a detailed discussion of the various mechanisms governing these phenomena, the reader is directed to Ref. (Saleh and Teich 1991).

2.1.1. Optical absorption

Optical absorption results in a reduction in the intensity of an optical beam, composed of photons traversing the medium. According to the Lambert-Bouguer Law, in a homogeneous, isotropic, uniformly optically absorbing medium, the absorption coefficient, μ_a, can be defined as

$$dI / I = \mu_a dx \tag{2.1}$$

where dI is the differential change in optical intensity I of a collimated optical beam traversing an infinitesimal path length of dx in the medium. For light propagation in solutions, another parameter that is often used to quantify the absorbing feature is the specific extinction coefficient ε_t (in units of μM^{-1}-cm^{-1}), which is related to the absorption coefficient through the expression

$$\varepsilon_t = \mu_a / (2.303 \cdot c_c), \tag{2.2}$$

Where C_c is the concentration of the compound.

In an inhomogeneous turbid medium the total absorption coefficient can be found through a linear superposition of individual absorption coefficients from each component, weighted by their relative concentrations (Kou *et al.* 1993; van Veen *et al.* 2004), *i.e.*,

$$\mu_a(media) = \sum_{i=1}^{N} \mu_{a,i} c_{c,i} , \tag{2.3}$$

where $\mu_{a,i}$ and $c_{c,i}$ represent the absorption coefficient and concentration of constituent i, respectively. For example, the primary chromophores contributing towards absorption in the visible and NIR wavelength in female breast tissue (Pifferi *et al.* 2004) include water (~32% by volume), lipids (~37% by volume), oxy-hemoglobin (HbO_2) (~16.17 μM) and deoxy-hemoglobin (Hb) (~4.83 μM). The contributions from other components of the breast tissue are typically ignored (Heffer and Fantini 2002) due to their low concentrations. This results in the absorption coefficient of this particular breast tissue being expressed as:

$$\mu_a = \mu_a(water)\times 32\% + \mu_a(lipid)\times 37\% + \varepsilon_t(HbO_2)\times 16.17 + \varepsilon_t(Hb)\times 4.83. \qquad (2.4)$$

The absorption spectra of water, lipid, hemoglobin and aorta are shown in Figure 2.2. Figure 2.2(a) shows that water has the lowest absorption for wavelengths below 850 nm and around 1050 nm. The absorption coefficient of fat (Figure 2.2b) is lowest between 600 nm and 850 nm but displays a peak at 930 nm. The vicinity of this peak wavelength (about 900-950 nm) is the only region where lipids have a strong effect on the optical absorption of the breast. Hemoglobin is responsible for delivering oxygen to the peripheral tissue and transporting byproducts to the lungs. Thus, the absorption of hemoglobin changes with the function and metabolism of biological tissues. The absorption spectra of oxy- and deoxy-hemoglobin, expressed in terms of specific extinction coefficient, are shown in Figure 2.2(c). Both kinds of hemoglobin preferentially absorb light at shorter wavelengths, and form the most important contributors to the total absorption of breast within this band. The strong absorption of hemoglobin below 600 nm establishes the short wavelength limit for biomedical optical imaging.

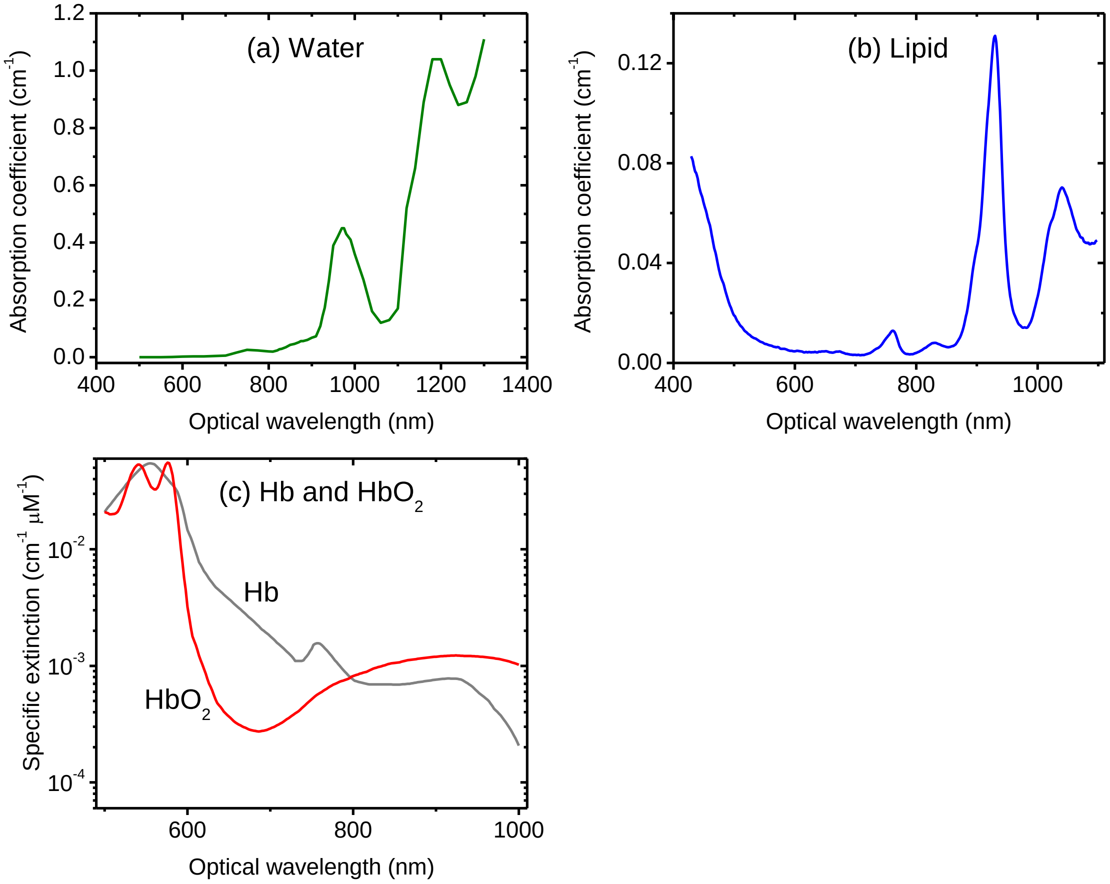

Figure 2.2 Optical absorption spectra of (a) water [Data from Ref. (Hale and Querry 1973)], (b) lipid [Data from Ref. (van Veen *et al.* 2004)], and (c) hemoglobin [Data from Ref. (Prahl 1999)] in the visible and NIR ranges.

In additional to the four components discussed above, there are a number of other tissue chromophores, such as vessel wall tissues, melanin and myoglobin. However, these can be largely ignored in the NIR (but not in the visible) regime due to their extremely low absorption and low constituent concentration.

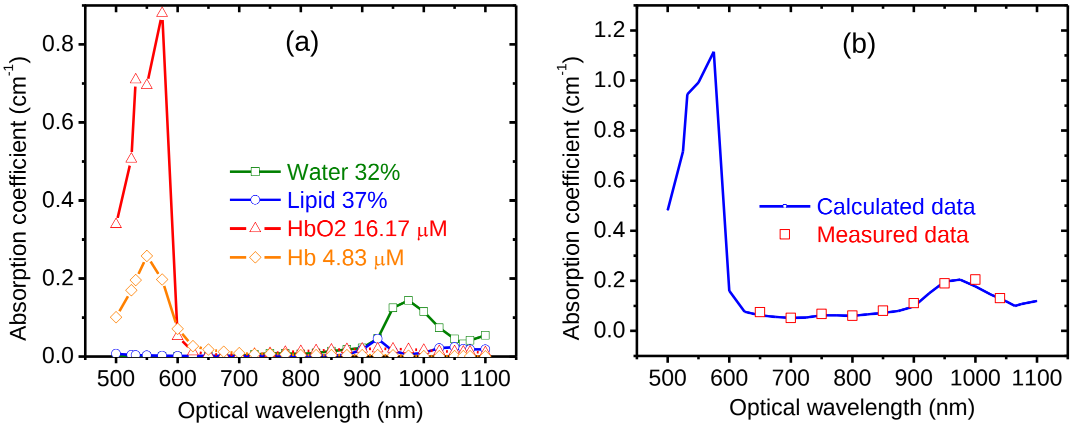

Figure 2.3 (a) The weighted absorption spectra of major chromophores of breast tissue between 500-1100 nm; (b) Absorption spectrum of a whole breast: calculated values (solid line) using Eq. (2.4) versus measured data (squares) extracted from Ref (Pifferi *et al.* 2004).

In Figure 2.3(a), the weighted absorption spectra of the major contributing constitutes are shown, and the calculated absorption spectrum of the whole breast based on Eq. (2.4) is shown along with the measured breast absorption coefficients *in vivo* (Pifferi *et al.* 2004) in Figure 2.3(b). As we can see, light absorption by blood dominates for the wavelengths below 600 nm and absorption by water plays a more important role above 950 nm. The optimal wavelengths for minimal optical absorption exist between 650-900 nm and 1040-1070 nm for whole breast tissue. The former range is often referred to as the "diagnostic and therapeutic window". Taking into account the reduction in scattering as a function of wavelength to be discussed in the next section, the window between 1040-1070 nm may also provide a useful range for optical diagnosis and therapy. This will be discussed in further detail in Chapter 3.

2.1.2. Optical scattering

Optical scattering usually dominates over absorption for visible and NIR light in biological tissues, complicating the photon paths and blurring the optical images. Scattering of light arises from either discrete scatterers or spatial fluctuations in the refractive index within a medium. Ordered by increasing size, sources of scatterers in tissue include membranes, macromolecular aggregates, collagen fibers, and cell organelles such as nuclei, cell, microstructures and ultrastrucutres. These are shown as a function of size in Figure 2.4. Among these, constituents with sizes comparable to the optical wavelength, such as lipids and collagen fibers, scatter light most effectively. This type of scattering is referred to as Mie scattering, which can be approximately calculated using Mie scattering theory (Prahl 1998). Scattering of light off structures much smaller than the light wavelength is usually referred to as the Rayleigh limit of Mie scattering, or simply, Rayleigh scattering (Saleh and Teich 1991).

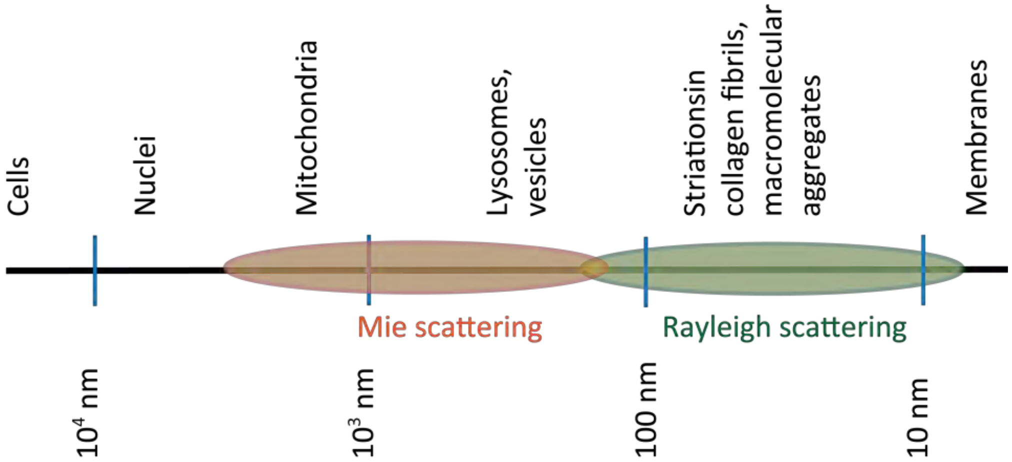
Cells
Nuclei
Mitochondria
Lysosomes, vesicles
Striationsin collagen fibrils, macromolecular aggregates
Membranes
Mie scattering
Rayleigh scattering
10^4 nm
10^3 nm
100 nm
10 nm

Figure 2.4 Tissue ultrastructures affecting visible and NIR light by Mie and Rayleigh scattering [Reproduced from Ref. (Prahl 2002)].

In an analog to absorption, one can define the scattering coefficient, μ_s, as

$$dI / I = \mu_s dx , \tag{2.5}$$

where dI / I is the scattered component of light after traversing a non-absorbing sample of infinitesimal path length dx. The sum of the absorption and scattering coefficients is termed as the total attenuation coefficient, and its reciprocal, $l = 1/(\mu_a + \mu_s)$ is called the scattering mean free path, which describes the average distance between consecutive scattering events.

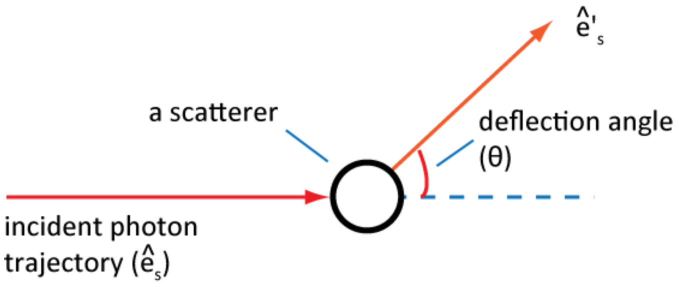

Figure 2.5 A schematic of a scattering event causing the deflection of a photon

Figure 2.5 shows when an incident photon propagating along a unit vector $\hat{e}_s$ encounters a scattering site, it is redirected at a new angle, θ. The angular probability of the photon being deflected into the direction of $\hat{e}_s^{'}$ can be expressed with a phase function $f(\hat{e}_s, \hat{e}_s^{'})$ which is usually expressed as

$$f(\hat{e}_s, \hat{e}_s^{'}) = f(\cos\theta) . \tag{2.6}$$

The mean value of the cosine of θ is defined as the anisotropy factor, g:

$$g = < \cos\theta > = \int_{-1}^{1} \cos\theta f(\cos\theta) d\cos\theta . \tag{2.7}$$

g is a measure of the amount of forward direction retained after a single scattering event and ranges from a value of 0 for perfectly isotropic (equi-directional) scattering to 1 for purely forward scattering.

The scattering coefficient and the anisotropic factor are often combined to define a new parameter called the reduced scattering coefficient, $\mu_s^{'}$:

$$\mu_s^{'} = \mu_s(1-g)\,. \tag{2.8}$$

Four more parameters are frequently used in depicting the optical properties of tissue. The list consists of transport coefficient ($\mu_t^{'} = \mu_a + \mu_s^{'}$), reduced (transport) mean free path ($l_{tr} = 1/\mu_t^{'}$), diffusion coefficient ($D = 1/[3(\mu_a + \mu_s^{'})]$) and effective attenuation coefficient ($\mu_{eff} = \sqrt{3\mu_a(\mu_a + \mu_s^{'})}$).

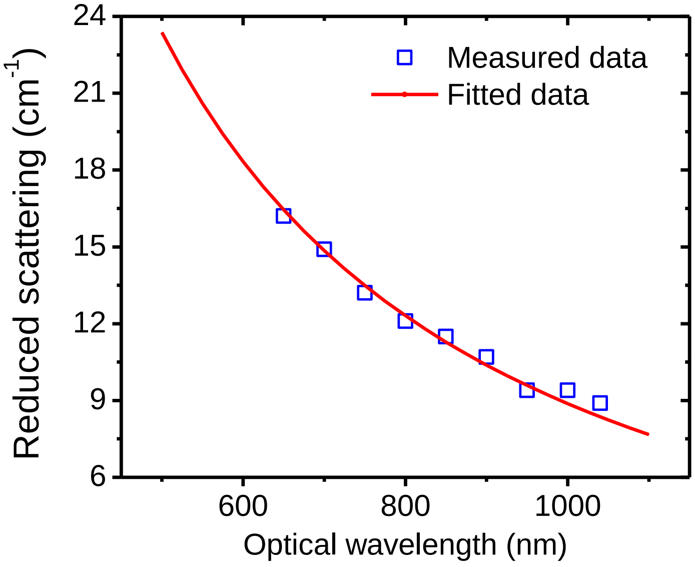

Figure 2.6 The measured (Pifferi *et al.* 2004) and theoretical (Mourant *et al.* 1997; Nilsson *et al.* 1998) values for the reduced scattering spectrum of human breast tissue.

Figure 2.6 shows the measured (squares) (Pifferi *et al.* 2004) reduced scattering spectrum of breast tissue *in vivo*, which is fitted (line) using an empirical function based on the Mie scattering theory (Mourant *et al.* 1997; Nilsson *et al.* 1998):

$$\mu_s'(\lambda) \approx a\lambda^{-b} , \qquad (2.9)$$

where a is the scattering prefactor mainly affected by the scatterer density, λ is the optical wavelength, and b is the scattering power related to the scatterer average size. A higher value of b corresponds to smaller scatterer size, characterized by a steep slope of the spectrum. It is shown in Figure 2.6 that the reduced scattering coefficient of breast tissue reduces as a function of optical wavelength. This indicates that, for optical imaging of deep regions in soft tissues like breast, longer wavelengths are preferred in terms of less light diffusion.

2.1.3. Modeling of light propagation in tissue: a brief introduction

NIR light propagation in a turbid medium is dominated by multiple scattering events. This process can be approximated using a radiative transport equation (RTE) (Chandrasekhar 1950; Ishimaru 1978):

$$\frac{1}{c}\frac{\partial I(\vec{r},t,\hat{e}_s)}{\partial t} + \hat{e}_s \cdot \nabla I(\vec{r},t,\hat{e}_s) + \mu_t I(\vec{r},t,\hat{e}_s) = \mu_s \int_{4\pi} f(\hat{e}_s,\hat{e}_s')I(\vec{r},t,\hat{e}_s')d^2\hat{e}_s' + q(\vec{r},t,\hat{e}_s) , \qquad (2.10)$$

where c is the speed of light in the medium, $I(\vec{r},t,\hat{e}_s)$ is the energy radiance for photons traveling at point $\vec{r}$ in direction $\hat{e}_s$ at time t, and $q(\vec{r},t,\hat{e}_s)$ is the energy source (power) into a unit solid angle centered on $\hat{e}_s'$ in a unit volume at position $\vec{r}$ at time t.

While exact solutions of the RTE exist for simple cases, such as for purely absorbing media, there is no general solution. Instead, further approximations or numerical algorithms are required. The diffusion approximation (DA) is one such approximation that assumes $\mu_s^{'} \gg \mu_a$ and neglects the higher order source terms. This leads to the diffusion equation (DE) (Patterson *et al.* 1989; Contini *et al.* 1997; Wang 1998):

$$\frac{1}{c}\frac{\partial \Psi(\vec{r},t)}{\partial t} - D\nabla^2\Psi(\vec{r},t) + \mu_a\Psi(\vec{r},t) = q_0(\vec{r},t)\,, \tag{2.11}$$

where $\Psi = \int_{4\pi} I(\vec{r},t,\hat{e}_s)d^2\hat{e}_s$ is the photon density and q_0 represents the optical source term.

In the steady state where a CW laser is used, Eq. (2.11) can be further reduced to

$$[\nabla^2 - \mu_{eff}{}^2]\Psi(\vec{r}) = -q_0(\vec{r})/D\,. \tag{2.12}$$

Analytical solutions to Eq. (2.12) in a homogeneous medium have been obtained for simple geometries such as infinite and semi-infinite media and slabs. These solutions are relevant to clinical applications and help in interpretation of the detected AO signals. The details of these solutions can be found in Ref. (Sui 2005).

2. 2. Mechanisms for ultrasound-induced modulation of diffusive light

2. 2. 1. A general review of mechanisms of ultrasound-induced phase modulation

It is currently assumed that two primary physical mechanisms contribute to AO interaction. The first is associated with the optical phase variation of the partial wave fronts (that form the diffuse optical field in tissue) due to the ultrasound induced periodic spatial displacement of the optical scatterers. This was first modeled and verified experimentally (Leutz and Maret 1995) by Leutz and Maret in 1995 in the weakly scattering regime (*i.e.*, the scattering mean free path is much greater than the acoustic wavelength). As the ultrasound wave propagates in a diffuse medium, scatterers residing within the path of the ultrasound beam are periodically displaced due to the compression and rarefaction of ultrasound waves. This displacement field is found by integrating the ultrasound velocity field, which in turn is related to the pressure field via the acoustic impedance. Thus, particle displacements are temporally coherent with pressure variations and, for linear acoustic waves, the displacement amplitude is linearly related to the pressure amplitude. The optical path length therefore changes when light propagates through a medium in which there is also an acoustic field. For an individual photon, the time it takes to traverse the acoustic field is very short compared with the acoustic period, thus the medium is essentially "frozen". However, subsequent photons experience somewhat different path-length perturbations, in part because their trajectories are different and in part because the scattering sites have moved. The net effect, when summed over a large number of photons traversing an optically diffuse region over acoustically relevant time scales, is a modulation in the effective optical path length – leading to a concomitant modulation in phase, at the ultrasound frequency.

The second mechanism is tied to optical phase variations in the wave fronts caused by periodic changes in the optical index of refraction. Acoustic pressure and density perturbations are related by the bulk modulus. Changes in density lead to changes in the refractive index as will be discussed in detail later. The result is a shift in the path length that accumulates along each partial wave. This mechanism was first proposed by Kemp *et al.* in 1997 (Kempe *et al.* 1997) and later modified to incorporate analytical and Monte Carlo analysis by Wang in 2001 (Wang 2001a; Wang 2001b).

The exploitation of both mechanisms mentioned above requires a coherent laser light source and it is assumed that the transport mean free path is greater than or equal to the acoustic wavelength (λ_a). This condition is required to ensure that the acoustically induced fluctuations in scatterer positions are uncorrelated with any random motion or flow which may occur within the sample (Kempe *et al.* 1997). In other words, the phase increments associated with different scattering events are of random ultrasound phase and weakly correlated. Previous studies further assumed that the phase modulations due to both mechanisms are independent of each other. These studies suggest that the modulation will be increased with higher reduced scattering coefficients where one has more scattering events. This is, however, contrary to experimental observations (Lai *et al.* 2009a; Lai *et al.* 2009b).

In 2005, Sakadzic and Wang (Sakadzic and Wang 2005) extended and modified their original model to account for correlations between the phase increments from scatterer displacement and optical refractive index variations. Drawing from this study, the following Section discusses in greater detail the principles of ultrasound-induced phase modulation of diffuse light.

2. 2. 2. Speckle intensity and ultrasound-induced phase modulation

For the model presented below, the following assumptions were made:

a) The optical wavelength in the medium is much smaller than the scattering mean free path l, meaning the optical scatterers are sufficiently separated to ensure that there is no systematic phase relation between scattering events (Mishchenko *et al.* 2000);

b) The phase perturbation induced by the ultrasound is very weak, much smaller than one radian (Wang 2001a);

c) Ultrasound- and Brownian motion-induced phase variations are distinguishable; and

d) Acoustic streaming is not considered.

Figure 2.7 illustrates a partial wave front in a diffuse medium experiencing N scattering events at positions $\vec{r}_1$, …., $\vec{r}_N$ under the influenced of an ultrasound field propagating along the Z axis. E_s is the resulting electrical field at the distal side of medium and $\vec{k}_a$ is the wave vectors of the ultrasound field. $\vec{l}_{i+1} = \vec{r}_{i+1} - \vec{r}_i$ is defined as the vector connecting two successive scatterers. θ_{i+1} is the angle between $\vec{k}_a$ and $\vec{l}_{i+1}$, and $\chi_{i+1} = \cos\theta_{i+1}$. $\varepsilon_i(t)$ is the projection of the ultrasound induced scatter displacement of the ith scatterer at time t along the ultrasound propagation direction.

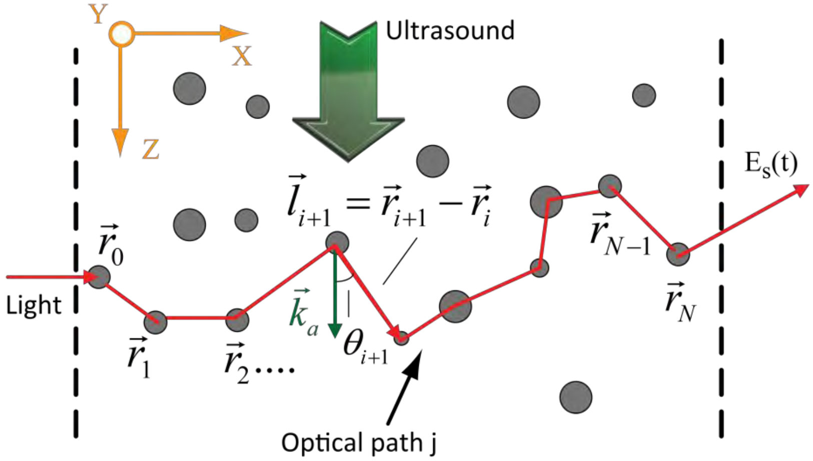

Figure 2.7 Ultrasound-modulation of multiply scattered light in a diffuse medium

Supposing the partial wave front shown in Figure 2.7 has an initial phase of φ_0, the phase of this wave front after traversing the turbid medium becomes

$$\varphi = \varphi_0 + \Delta\varphi_s + \Delta\varphi_{s,B} + \Delta\varphi_{s,U}, \tag{2.13}$$

where $\Delta\varphi_s = \sum_{i=1}^{N} \vec{k}_i \cdot \vec{l}_i$ is the random accumulated phase from the multiple scattering along paths s that is independent of the ultrasound perturbations. $\Delta\varphi_{s,B}$ is the phase increments associated with the Brownian motion, which can be assumed to be constant for all different optical paths. $\Delta\varphi_{s,U}$ is the additional phase increments due to the presence of ultrasound modulation, which can be written as

$$\Delta\varphi_{s,U} = \Delta\varphi_{s,n} + \Delta\varphi_{s,d}, \tag{2.14}$$

where $\Delta\varphi_{s,n}$ and $\Delta\varphi_{s,d}$ represent the terms associated with the accumulative variations of refractive index and the accumulative displacement of optical scatterers.

The electrical field of the speckle corresponding to this partial wave can be written as

$$E_s = \left|E_{s,0}\right| \exp[i(\varphi_0 + \varphi_{s,B})] \cdot \exp(i\varphi_s) \exp[i(\Delta\varphi_{s,n} + \Delta\varphi_{s,d})]\,, \tag{2.15}$$

where $\left|E_{s,0}\right|$ is the magnitude of E_s in the absence of ultrasound modulation. Drawing from the analysis of Sakadzic and Wang (2005), the resulting intensity of this speckle is proportional to

$$I_s \propto 1 + i2[\langle \Delta\varphi_{s,n} \rangle_{t,H} + \langle \Delta\varphi_{s,d} \rangle_{t,H}] - 2[\langle (\varphi^2_{s,n} \rangle_{t,H} + \langle \Delta\varphi^2_{s,d} \rangle_{t,H} + \langle 2\Delta\varphi_{s,n}\Delta\varphi_{s,d}) \rangle_{t,H}]\,. \tag{2.16}$$

Hence, the speckle intensity is directly modulated by (1) the ultrasound-induced displacement of the optical scatterers, (2) variations in optical index of refraction, and (3) the cross correlation between these two mechanisms. By computing the modulation terms in Eq. (2.16), we hope to be able to understand the influence of ultrasound modulation on the intensity of the diffuse partial wave front.

By assuming that the ultrasonic plane wave is propagating along the Z axis in a lossless sample (Figure 2.7), the *in situ* acoustic pressure is given by

$$P(z,t) = P_0 f(z,t)\,, \tag{2.17}$$

where P_0 is the peak focal pressure, and $f(z,t)$ is the pressure propagation temporal and spatial function. By assuming that the pressure propagation function corresponds to an infinite train of ultrasound pulses (Zitter 1968; Neighbors and Mayer 1983), $f(z,t)$ can be defined as follows

$$f(z,t) = \sum_{m=-\infty}^{+\infty} f_0(z - \upsilon_a t - m\upsilon_a T)\,, \tag{2.18}$$

where υ_a is the sound speed in the medium. T is the time period between ultrasonic pulses, and $f_0(z-\upsilon_a t)$ represents the shape of a single ultrasonic pulse. The strain in the medium, at position z and time t, generated by the ultrasound field is given by

$$\zeta(z,t)=\zeta_0\cos(\omega_a t-k_a z), \tag{2.19}$$

where $\omega_a=2\pi f_a$ is the angular frequency of the ultrasound (f_a is the ultrasound frequency), k_a is the wave number of the ultrasound ($k_a=\omega_a/\upsilon_a$), and ζ_0 is the amplitude of the strain, equaling to $\zeta_0=P^2/(2\rho\upsilon_a)$ (Saleh and Teich 1991), where ρ is the mass density of the medium.

This induced strain causes a spatial variation in refractive index (Saleh and Teich 1991) of the form

$$\Delta n(z,t)=-\frac{1}{2}\eta\zeta_0^3 f(z,t), \tag{2.20}$$

where η is the photoelastic constant (or strain-optic coefficient) of the medium. Thus, the optical index of refraction of the medium has a form of the incident ultrasonic field

$$n(z,t)=n_0+\left|\Delta n(z,t)\right|\cos(\omega_a t-k_a z), \tag{2.21}$$

with an amplitude of

$$\left|\Delta n(z,t)\right|=\frac{1}{2}\eta n_0^3\zeta_0=\frac{1}{2}n_0 Mf(z,t), \tag{2.22}$$

where n_0 is the equilibrium state index of refraction of the medium, and $M=\dfrac{\eta n_0^2 P_0}{\rho\upsilon_a^2}$.

Therefore, the phase increments resultant from variations in medium refractive index can be expressed as (Wang 2001a; Sakadzic and Wang 2002)

$$\Delta\varphi_{s,n} = \sum_{i=0}^{N}\int_{\vec{r}_i}^{\vec{r}_{i+1}} k_0 \Delta n dr = \frac{1}{2}k_0 n_0 M \sum_{i=0}^{N}\int_{\vec{r}_i}^{\vec{r}_{i+1}} \Delta f(\vec{r},t,\tau)dr\,, \tag{2.23}$$

where $\Delta f(\vec{r},t,\tau) = f(\vec{r},t+\tau) - f(\vec{r},t)$. Similarly, the phase increments from the displacement of scattering sites can be expressed by

$$\Delta\varphi_{s,d} = k_0 n_0 \sum_{j=1}^{N}(\chi_j - \chi_{j+1})\Delta\varepsilon_j(t,\tau)\,, \tag{2.24}$$

with $\Delta\varepsilon_j(t,\tau)$ defined by $\varepsilon_j(t+\tau) - \varepsilon_j(t)$.

The acoustic pressure propagation function, $f(z,t)$ shown in Eq. (2.18), can be expressed in terms of its Fourier spectral components

$$f(z,t) = \frac{1}{\upsilon_a T}\sum_{m=-\infty}^{+\infty}\tilde{f}_0\left(\frac{m}{\upsilon_a T}\right)\exp[-im(k_a z - \omega_a t)]\,, \tag{2.25}$$

where the Fourier transform $\tilde{f}_0(\nu)$ of the ultrasound pulse shape function $f_0(z-\upsilon_a t)$ is

$$\tilde{f}_0(\nu) = \int_{-\infty}^{+\infty} f_0(u)\exp[i2\pi u\nu]du\,. \tag{2.26}$$

The particle (scatterer) velocity $\tilde{\upsilon}(f)$ is related to the background medium velocity $\tilde{u}(f)$ by (Siegel and Plueddemann 1991; Sakadzic and Wang 2005)

$$\tilde{\upsilon}(f) = \tilde{u}(f)S_m\exp(i\phi_m)\,, \tag{2.27}$$

where S_m and ϕ_m represent the amplitude and the phase of the particle velocity deviation from that of the fluid. Since the velocity of the background fluid is given by $P(z,t)/(\rho\upsilon_a)$, the displacement of the j th scatterer by the ultrasound field can thus be expressed by

$$\varepsilon_j(t) = -\frac{iP_0}{2\pi\rho\upsilon_a^2}\sum_{\substack{m=-\infty \\ m\neq 0}}^{+\infty}\tilde{f}_0\left(\frac{m}{\upsilon_a T}\right)\frac{S_m\exp(-i\phi_m)}{m}\exp[-im(k_a z-\omega_a t)]\,. \tag{2.28}$$

In this equation, any acoustic streaming in the fluid is neglected, thus excluding the spectral component associated with $m = 0$.

Through the combination of Eqs. (2.23)-(2.25) and (2.28), the phase increment terms can be written as

$$\begin{aligned}\Delta\varphi_{s,n} = i\frac{\Lambda}{4\pi}\sum_{\substack{m=-\infty \\ m\neq 0}}^{+\infty}\{&\frac{\eta}{m}\tilde{f}_0\left(\frac{m}{\upsilon_a T}\right)\exp(im\omega_a t)[\exp(im\omega_a\tau)-1] \\ &\times\sum_{j=0}^{N}\frac{1}{\chi_{j+1}}[\exp(-imk_a z_{j+1})-\exp(-imk_a z_j)]\}\end{aligned} \tag{2.29}$$

$$\begin{aligned}\Delta\varphi_{s,d} = -i\frac{\Lambda}{4\pi}\sum_{\substack{m=-\infty \\ m\neq 0}}^{+\infty}\{&\frac{S_m\exp(-i\phi_m)}{m}\tilde{f}_0\left(\frac{m}{\upsilon_a T}\right)\exp(im\omega_a t) \\ &\times[\exp(im\omega_a\tau)-1]\sum_{j=1}^{N}(\chi_j-\chi_{j+1})\exp(-imk_a z_j)\}\end{aligned} \tag{2.30}$$

where $\Lambda = \dfrac{2n_0 k_0 P_0}{\rho\upsilon_a^2}$.

The linear term in Eq. (2.16) is zero for any pulse shape function $f_0(u)$, i.e., $\left\langle\Delta\varphi_{s,n}\right\rangle_{t,H} = \left\langle\Delta\varphi_{s,d}\right\rangle_{t,H} = 0$.

As a result, the speckle intensity (Eq. (2.16)) becomes

$$I_s \propto 1-2[\left\langle(\Delta\varphi_{s,n}^2\right\rangle_{t,H}+\left\langle\Delta\varphi_{s,d}^2\right\rangle_{t,H}+\left\langle 2\Delta\varphi_{s,n}\Delta\varphi_{s,d})\right\rangle_{t,H}]\,. \tag{2.31}$$

Through further manipulations (Sakadzic and Wang 2002; Sakadzic and Wang 2005), the terms in Eq. (2.31) can be expressed as

$$\left\langle \Delta\varphi_{s,n}^2 \right\rangle_{t,H} = \sin^2(\frac{1}{2}\omega_a\tau)C_{s,n}, \tag{2.32}$$

$$\left\langle \Delta\varphi_{s,d}^2 \right\rangle_{t,H} = \sin^2(\frac{1}{2}\omega_a\tau)C_{s,d}, \tag{2.33}$$

$$\left\langle 2\Delta\varphi_{s,n}\Delta\varphi_{s,d} \right\rangle_{t,H} = \sin^2(\frac{1}{2}\omega_a\tau)C_{s,nd}, \tag{2.34}$$

where the C terms are expressed by

$$C_{s,n} = \Lambda^2 \frac{\eta^2}{k_a^2}(k_a l)^2[(\frac{s}{l}+1)\frac{G}{1-G} - \frac{G(1-G^{s/l-1})}{(1-G)^2}], \tag{2.35}$$

$$C_{s,d} = \Lambda^2 \frac{S^2}{k_a^2}[\frac{1}{3}\frac{s}{l} - \frac{1-G^{s/l-1})}{(k_a l)^2}], \tag{2.36}$$

$$C_{s,nd} = \Lambda^2 \frac{2\eta S\cos(\phi)}{k_a^2}[-\frac{s}{l} - \frac{G(1-G^{s/l})}{(1-G)}], \tag{2.37}$$

with $G = \arctan(k_a l)/(k_a l)$. The net magnitude of the modulation due to the ultrasound on optical path s is thus

$$C_{s,U} = C_{s,n} + C_{s,d} + C_{s,nd}. \tag{2.38}$$

And the intensity of the speckle in Eq. (2.31) can be expressed by

$$I_s \propto 1 - 2C_{s,U}. \tag{2.39}$$

It should be noted that we focus on a single frequency component ($m = 1$), corresponding to the use of single-frequency CW ultrasound to generate the AO interaction. This analysis, however, can also be extended for broadband conditions (Sakadzic and Wang 2005).

2. 2. 3. The physical significance of $C_{s,U}$

In the absence of ultrasound modulation, i.e., $C_{s,U} = 0$, the diffuse light intensity is maximum, possessing a value of, say, $I_{s,0}$. When the ultrasound field is applied to the target region, the speckle intensity is proportional to $I_{s,0}(1-2C_{s,U})$. Hence, the modulation depth (MD, defined by the ratio between the observed intensity change and the initial intensity, Wang 2004) on the speckle is

$$MD = \frac{I_{s,0} - I_s}{I_{s,0}} = 2C_{s,U}\,. \tag{2.40}$$

Thus $C_{s,U}$ provides a measure of the strength of ultrasound-induced signal modulation, with higher $C_{s,U}$ representing stronger modulation of diffuse light.

It should be noted that such $C_{s,U}$ only corresponds to the contribution of the signal modulation due to the ultrasound from a single partial wave front with path length s as shown in Figure 2.7. If a large aperture optical sensor is used to detect light from multiple wave fronts, the term φ_s in Eq. (2.15), which relies on the specific optical path length that each partial wave front travels, causes a reduction in the net modulation depth on the diffuse light. To overcome this, as suggested in Chapter 1, one has to either employ an array-based detector where each pixel is matched to one speckle grain and then coherently sum over all pixels, or incorporate a heterodyne scheme to help make the detection independent of any incoherence between speckles. For both cases, the detected intensity of all the wave fronts in the absence of ultrasound modulation can be written as

$$I_0 = \sum_s \zeta I_{s,0} = \zeta \sum_s I_{s,0} \, , \tag{2.41}$$

with ζ representing the effect of optical attenuation or magnification associated with the specific detection scheme employed, which is path independent. Thus, the light intensity in the presence of ultrasound modulation is proportional to $I_0^{'} \propto \zeta \sum_s I_{s,0}(1-2C_{s,U})$, and the strength of modulated AO signal can be written as

$$\Delta I_0 = I_0^{'} - I_0 \propto -2\zeta \sum_s I_{s,0} C_{s,U} \, . \tag{2.42}$$

2. 2. 4. The influence of acousto-opto-tissue properties on modulation

Eqs. (2.35)-(2.37) show that the modulation due to refractive index variations and scatterer displacement are not perfectly linear with s/l (the average number of scattering events) and for smaller values of $k_a l$ (low ultrasound frequency and/or large optical absorption and scattering), phase increments from consecutive scattering events are not totally independent of each other. Moreover, there is an interaction between phase increments from these two mechanisms. This is attributed to the fact that at each scattering position, the phase increment due to the scatterer displacement can be approximated as a sum of the two terms (Eq. (2.24)), which are associated with the incoming and outgoing scattering directions, while each free path (affecting the refractive index variations) between two consecutive scatterers is associated with two such displacements (Eq. (2.23)). The phase accumulation of these displacement terms differ from the phase of the index of refraction term associated with the corresponding free path by exactly $\pi + \phi$. Therefore, the strength of the product between the two mechanisms is proportional to $-\cos(\phi)$.

Next let us look at how each of the C terms is influenced by the ultrasound field and optical properties within the acousto-optic interaction region.

2.2.4.1 Contribution from scatterer displacement

For very small values of $k_a l$, the change in ultrasonic phase is negligible for two consecutive scatterers that are located on the same optical path. These scatterers will undergo displacements in the same direction, leading to non-random phase increments, and the phase increments from scattering displacements among different scattering events will be correlated. As a result, there is a destructive interference term in the expression in Eq. (2.36). Conversely, when $k_a l$ is large enough, each scattering event is located at a different phase of the ultrasound field, and these increments are independent and uncorrelated. In this case, $\frac{1-G^{s/l-1}}{(k_a l)^2} \to 0$, and $C_{s,d}$ can be approximated as

$$\Lambda^2 \frac{S^2}{k_a^2} \frac{1}{3} \frac{s}{l} = \frac{1}{3} \left(\frac{2 n_0 k_0}{\rho \upsilon_a^2} \right)^2 S^2 P_0^2 \left(\frac{s}{l} \right) \frac{1}{k_a^2}. \tag{2.43}$$

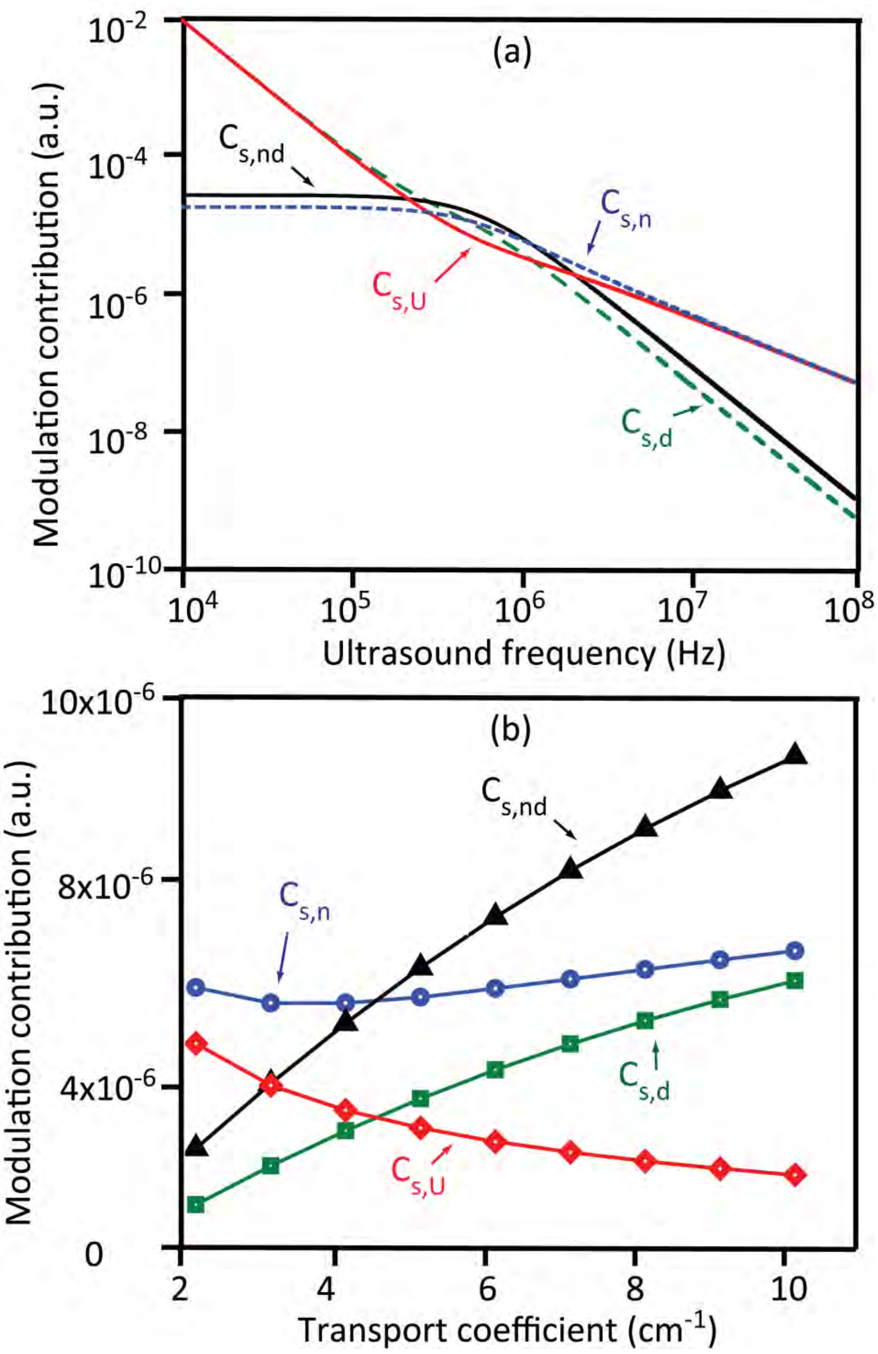

Figure 2.8 Dependence of all C terms as a function of (a) ultrasound frequency and (b) transport coefficient computed with parameters listed in Table 2.1. Green (squared) line is for $C_{s,d}$, blue (circled) for $C_{s,n}$, black (triangular) for $C_{s,nd}$, and red (diamond) for the net contribution $C_{s,U}$.

Table 2.1 Parameters used for the simulations in Figure 2.8

Symbol	n_0	η	P_0	S	ϕ	λ_0	υ_a	ρ	s
Value	1.33	0.32	1 MPa	1	0	1064 nm	1.5 mm/µs	1000 kg/m^3	2 mm

Symbol	$^{\dagger}\mu_a$	$^{\dagger}\mu_s'$	$^{\dagger}f_a$	$^{\ddagger}\mu_a$	$^{\ddagger}\mu_s'$	$^{\ddagger}f_a$
Value	0.14 cm^{-1}	5 cm^{-1}	10-10^5 kHz	0.14 cm^{-1}	2-10 cm^{-1}	1 MHz

* Assuming the scatterers exactly follow the displacement of the background medium (Siegel and Plueddemann 1991; Leutz and Maret 1995).

† Used for Figure 2.8(a) only.

‡ Used for Figure 2.8 (b) only.

Figure 2.8 presents the dependence of the modulation contribution due to the scatterer displacement ($C_{s,d}$) on ultrasound frequency (f_a) (green line in Figure 2.8a) and on transport coefficient ($\mu_t' = \mu_a + \mu_s'$) (green squares in Figure 2.8b) with parameters given in Table 2.1 that approximate the real conditions in our experiments.

From Eq. (2.43) we can see that $C_{s,d}$ increases quadratically with ultrasound focal pressure. In Figure 2.8, the signal modulation contributed from the scatterer displacement is reduced when the ultrasound center frequency is increased. For increased medium optical absorption and/or scattering coefficients within the AO interaction region, modulation contribution from the scatterer displacement is increased.

2.2.4.2 Contribution from refractive index variation

Modulation from the refractive index variation (Eq. (2.35)) can be approximated as

$$C_{s,n} \approx \Lambda^2 \frac{\eta^2}{k_a^2}(k_a l)^2 \frac{s}{l} G \approx \Lambda^2 \frac{\eta^2}{k_a^2}(k_a l)^2 \frac{s}{l} \frac{\arctan(k_a l)}{k_a l}, \tag{2.44}$$

for high $k_a l$ values where $G \rightarrow 0$ and $\frac{G}{1-G} \rightarrow G$. Considering $\arctan(k_a l) \rightarrow \pi/2$ for very high $k_a l$ values, Eq. (2.44) can be further approximated as

$$C_{s,n} \approx \frac{\pi}{2} \Lambda^2 \eta^2 s \frac{1}{k_a}. \tag{2.45}$$

This equation shows that $C_{s,n}$ is quadratically dependent on ultrasound pressure amplitude but linearly proportional to f_a^{-1} which is illustrated in Figure 2.8(a). In a more diffusive medium (say, $\mu_t^{'} \geq 4\,cm^{-1}$ as in Figure 2.8b), the modulation contribution from the refractive index variation increases with higher medium absorption and/or scattering within the AO interaction region.

2.2.4.3 Contribution from the cross correlation between two mechanisms

It is shown in Eq. (2.37) that the cross correlation effect constitutes a destructive interference that is quadratically dependent on ultrasound pressure amplitude. For high $k_a l$ values,

$$C_{s,nd} \approx -\Lambda^2 \frac{2\eta S \cos(\phi)}{k_a^2} \frac{s}{l}, \tag{2.46}$$

showing the magnitude of the correlation effect is proportional to f_a^{-2} and proportional to the number of scattering events as illustrated in Figure 2.8(a) and (b).

2.2.4.4 The net modulation due to the ultrasound

The description above suggests that, for the parameters considered here, $C_{s,d}$ dominates over the other two effects for small values of $k_a l$. The magnitude of the correlation effect from all contributions decreases with ultrasound frequency, where $C_{s,n}$ is proportional to f_a^{-1} while the other two effects are proportional to f_a^{-2} and negate each other. Ultimately, $C_{s,n}$ is the primary effect among the three and determines the net modulation at high $k_a l$. For $f_a = 1$ MHz used for this study, the magnitude of all three contributions are found to increase with increased transport coefficient, *i.e.*, the incorporation of more scattering events ($C_{s,n}$ is only valid for $s/l \geq 5$). However, the net modulation experiences a decrease with increased $\mu_t^{'}$, which agrees with experimental results indicating a reduction in the strength of ultrasound modulation for higher medium absorption and/or scattering coefficients within the AO interaction region. This will be further discussed in Chapter 4.

2. 3. Summary

In Section 2.1, an introduction to the concepts of optical absorption and scattering properties in diffuse media was given in the context of light propagation in human breast tissue. The wavelength dependence of these parameters indicates that to achieve optical imaging deep (several cm) within breast tissue, the optimal wavelength ranges are between 700-900 and 1040-1070 nm. Section 2.2 described the principles of ultrasound-induced phase modulation on diffuse light in turbid media. It was shown that phase increments due to scatterer displacement and refractive index variation from consecutive scattering events are correlated with each other when $k_a l$ value is small. It was also shown that the modulation from scatterer displacements actually interferes destructively with that from refractive index variations, yielding a third mechanism for influencing the modulation of diffuse light from the ultrasound field. The resulting net signal modulation for one speckle shows an inverse dependence on both ultrasound frequency and medium transport coefficient. The latter is one of the two physical processes providing optical sensing contrast in AOI, where instantaneous AO signal strength reduces with increased optical absorption and/or scattering within the AO interaction region. The other principle source of contrast in AOI is due to the fact that changes in optical properties can vary the amount of photons available to be "tagged" by the ultrasound field, and hence affect the AO signal strength.

It should be noted at this point that the signal modulation ($C_{s,U}$) corresponds only to one speckle grain, which is only several microns in diameter (Selb *et. al* 2001) and thus not easily detected in the presence of noise. In order to sense a sufficient number of modulated photons, a detection aperture subtending multiple speckles is called for. Problem is, the phase of modulation varies randomly from speckle to speckle (the term φ_s in Eq. (2.15) is optical path dependent). When summed coherently, the result is compromised modulation efficiency. Thus far, two types of approaches have been proposed to tackle this limitation. One is the CCD array-based parallel detection scheme (Leveqe-Fort *et. al* 1999) that allows for coherent summation of signal amplitudes from individual pixels. However, this approach is limited by array frame rate in terms of sensing speed and by the time required to transfer large data sets from the array to the computer. The second solution is to incorporate an interferometric scheme employing, e.g. a photorefractive crystal, that allows for greater etendue, the use of a large, single aperture optical detector, and coherent signal summation over multiple speckles. In Chapter 3, we describe an AO imaging/sensing system based on a 7x7x7x mm^3 GaAs crystal, which is capable of coherently summing light from more than half a million speckles, each possessing an average diameter of only 10 μm.

Chapter 3

Acousto-Optic Imaging System in the Near-Infrared Using the Photorefractive Effect

3. 0. Overview

Herein is described the development and characterization of a GaAs photorefractive crystal-based AO imaging system operating at 1064 nm optical wavelength. In Section 3.1, the motivation behind the transition from 532 to 1064 nm operating wavelength is described. The experimental setup is presented in Section 3.2, and following that in Section 3.3, we detail the characterization of the system, which includes the measurement of the incident optical beam, ultrasound transducer calibration, quantitative estimates of optical properties of tissue phantoms, the principle and optimization of PRC effect in the context of AO sensing, and lastly, characterization of system noise.

3. 1. System design: the rationale for employing a 1064 nm optical wavelength

Several years ago, our laboratory developed an AOI system employing a photorefractive crystal (PRC) designed to work at an optical wavelength of 532 nm (Sui 2005). It used a bismuth silicon oxide ($Bi_{12}SiO_{20}$, or BSO for short) crystal at the core of a PRC-based interferometry scheme to detect the transient bursts of ultrasound-induced modulated light generated by short ultrasound pulses in turbid media. However, the application of the system to sensing and imaging in soft tissues was limited by two major technical barriers: (a) the imaging depth in biological tissues was limited (around two centimeters in chicken breast with reasonable SNR) due to the high optical effective attenuation coefficient (μ_{eff}) and restricted optical maximum permissible exposure (MPE) in tissue at this wavelength (~200 mW/cm^2) (American National Standards Institute 2000); (b) the photorefractive response time of the BSO crystal (~150 ms) was to slow to compensate for environmental vibration and physiological motion *in vivo* (on the order of 100 us - 1ms) (Gross *et al.* 2009). Therefore the earlier system needed to be redesigned to employ a longer optical wavelength (near-IR, or NIR for short) that allowed for a minimal μ_{eff} but elevated MPE in soft tissues such as breast. This called for a photorefractive crystal at near-IR possessing sufficient sensitivity (defined as the refractive index change per photon being absorbed) and adequately fast response time.

The optical absorption and reduced scattering spectrum of human female breast tissue are given in Figures 2.3 and 2.6, from which the effective attenuation coefficient spectrum of breast is calculated ($\mu_{eff} = \sqrt{3\mu_a(\mu_a + \mu_s^{'})}$) and shown in Figure 3.1(a). Table 3.1 lists the laser exposure MPE for different wavelengths and Figure 3.1(b) shows the relative optical fluence rate (weighted by the MPE value) as a function of depth and wavelength in breast tissue.

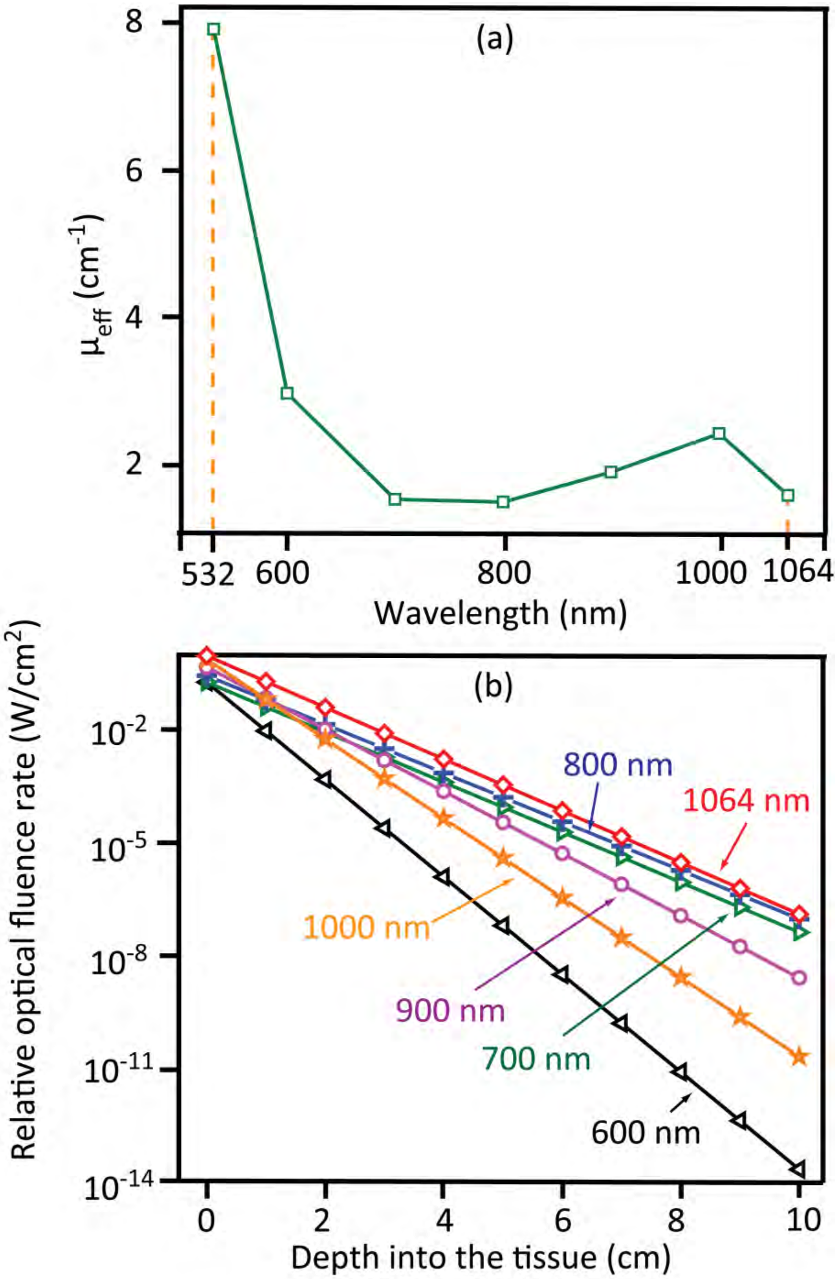

Figure 3.1 (a) Effective attenuation coefficient of human breast as a function of optical wavelength in the visible and near-infrared regime; (b) The decay of the optical field as a function of depth into the tissue for wavelengths between 600-1064 nm, weighted by the MPE level at each individual wavelength (Table 3.1).

Table 3.1 MPE for skin exposure (10-30,000 seconds) to a laser beam (American National Standards Institute 2000).

Optical wavelength (nm)	532	600	700	800	900	1000	1064
MPE (W/cm^2)	0.2	0.2	0.2	0.3	0.5	0.8	1

Figure 3.1 shows that μ_{eff} are minimal at 700, 800 and 1064 nm wavelengths, and at 1064 nm one can have maximum MPE that is 5 times of that at 532 nm. As a result, 1064 nm is the optimum choice in terms of maximum allowable optical fluence in breast tissue (Figure 3.1b). We chose to employ a 1064 nm Nd:YAG laser source and a gallium arsenide (GaAs) photorefractive crystal possessing a response time on the order of 1 ms when illuminated by light with an incident intensity of 100 mW/cm^2 (or even faster with stronger optical intensity) (Gross *et al.* 2009), potentially making it sufficiently fast to counterbalance the physiological speckle decorrelation. However, it must be kept in mind that the optical absorption due to water at 1064 nm is much stronger than visible wavelengths (Figure 2.2a), making 1064 nm not ideal option in environments with higher concentration of water.

3. 2. Experimental arrangement

A diagram of the experimental setup of the NIR system used for AO sensing at 1064 nm is given in Figure 3.2. A CW Nd:YAG laser (IRCL-700-1064-S, CrystaLaser, CA, USA) at 1064 nm is used as the light source. The output of the laser is split into a signal beam and a reference beam (also called pump beam) by a variable beam splitter composed of a half-wave plate and a beam splitter. The signal beam is expanded by a beam expander and directed along the Y-axis through the transparent walls of the water-filled test tank and sample holder. This beam illuminates the front surface of the sample with an optical intensity of approximately 200 mW/cm^2 (the measurement will be addressed in the next section). The incident light is scattered in the sample and phase modulated by the applied focused ultrasound field. The resulting diffused *signal beam* includes both the "tagged" and "untagged" photons and is collected at the distal side of the sample by a lens and focused onto the PRC, where it interferes with the reference beam guided around the water tank.

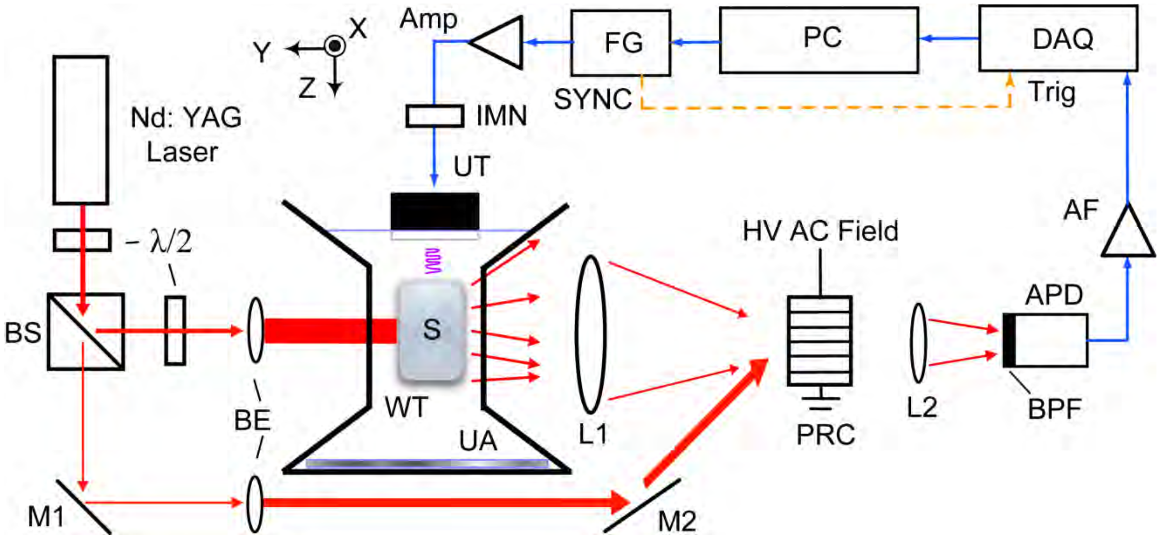

Figure 3.2 Schematic of the experimental setup. $\lambda/2$ - half-wave plate; BS- beam splitter; M_1, M_2- mirror; BE- beam expander; WT- water tank; S- tissue-mimicking phantom or *ex vivo* tissue sample; UA- ultrasound absorbing material; L_1, L_2- lens; HV AC- high voltage AC electrical field; PRC- photorefractive crystal; BPF- band-pass filter; APD- avalanche photodiode; AF- Active filter; DAQ- data acquisition device; Trig- external trigger terminal on the DAQ; PC- personal computer; FG- function generator; AMP- amplifier; IMN- impedance matching network; UT- ultrasound transducer; XYZ- system coordinate (Z is the vertical axis).

The intensity of the reference beam at the PRC is approximately 15 mW/cm^2. A 7x7x7 mm^3, GaAs crystal (MolTech GmbH, Berlin, Germany) is used in the demodulating interferometer in the study. This PRC is holographically cut along (001), (110), and $(1\bar{1}0)$, and it is optically polished and AR-coated at 1064 nm on both $(1\bar{1}0)$ faces. To enhance the efficiency of two-wave-mixing (TWM, also referred to as beam coupling) in the PRC, a 2.1 kHz, 7.14 kV/cm (peak-to-peak) high voltage AC electrical field is applied across the crystal. The response time of the crystal is a function of incident light intensity from both the reference beam and collected signal beam, and is around 10-15 ms under our experimental conditions. The principle of operation of the photorefractive effect used for the detection of AO signals is described in detail later in this Chapter.

Light exiting the PRC is band-pass filtered at 1064 nm and directed into the 5-mm diameter sensing aperture of an avalanche photodiode (APD, APD50, Pacific Silicon Sensor, CA, USA). The electrical signal from the APD is preamplified (20 dB) and low-pass filtered (at 500 kHz) using an active filter (Model 3940, Krohn-Hite, MA, USA). The signal is then digitized on an USB digitizer (NI USB-5132, 8 bit, 50 MS/s sample rate, National Instruments, TX, USA) which is triggered by the SNYC signal from the function generator. The SYNC signal is also used to trigger the ultrasound source). Finally, the digital signal is downloaded to a personal computer (PC, Dimension 4600, Dell, TX, USA) for further processing.

A function generator (33120A, Agilent, CA, USA), controlled by the PC, generates a sine-burst waveform with specific properties (frequency, pulse duration, PRF, etc.) determined by the specific imaging/sensing requirements. This wave form is attenuated 20 dB before being sent to a power amplifier (55 dB, A150, ENI, NY, USA), whose output is fed to an impedance matching network (IMN) to match the 50-ohm output impedance of the amplifier to the reactive (capacitive) impedance of the acoustic source. The output from the IMN drives an ultrasound transducer whose front face is submerged in water. A single element focused transducer with a 70 mm diameter and a 63-mm focal length (H101, Sonic Concepts, WA, USA) is used as the ultrasound source in the system. The acoustic axis (the Z direction) is aligned vertically downward and perpendicular to the incident laser beam such that the focal point intersects with the center of the incident signal beam. During the experiments, the IMN output is monitored with a high-impedance probe (x10, 10 MΩ), which feeds into an oscilloscope (LC334A, LeCroy, NY, USA). This is used to directly monitor the driving voltage into the ultrasound transducer, which can be mapped to the acoustic pressure using a calibration procedure described below.

The water tank was constructed of acrylic glass and possessed a contoured shape intended to allow for unimpeded ultrasound transmission while minimizing the optical propagation path of NIR light in water, thereby minimizing absorption losses. The bottom of the tank was lined with an absorber sheet (Aptflex F28, Precision Acoustics, Surrey, UK) to absorb ultrasound and minimize reflection.

3. 3. System calibration

3. 3. 1. Measurement of the expanded signal beam incident on sample surface

The size and power density of the expanded signal beam incident on the front surface of the sample is measured using a knife-edge technique (Khosrofian and Garetz 1983) and the setup illustrated in Figure 3.3.

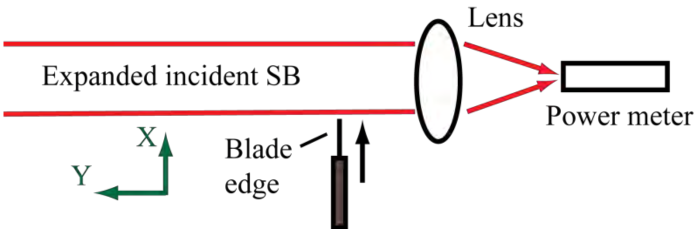

Figure 3.3 Setup of measuring the expanded signal beam

The measurement is performed with the tank and the sample in Figure 3.2 removed, and a lens is used to focus the expanded signal beam onto the aperture of a power meter (13PEM001, Melles Griot, NM, USA), which records the power of the unblocked (by the knife-edge) portion of the signal beam. By scanning the blade edge across the beam along X direction in small increments, we obtain a power distribution as a function of blade edge position (Figure 3.4a). A Gaussian fit to the derivative of Figure 3.4(a) yields the shape of the signal beam (Figure 3.4b), which has a FWHM of 16.1 mm. Accounting for the additional optical attenuation in our experimental system due to the tank/holder walls and the water (measured and/or calculated), the signal beam incident on the sample front surface in our study has an intensity of approximately 200 mW/cm^2.

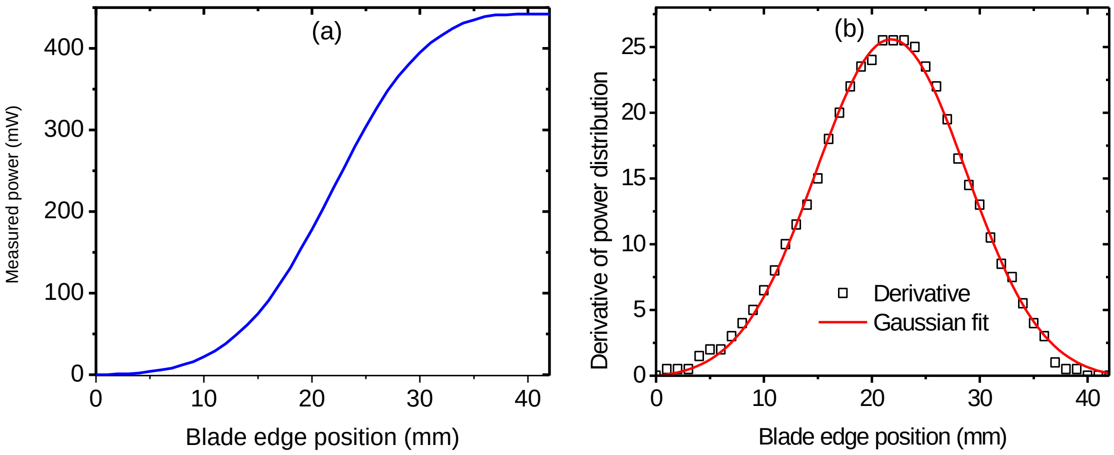

Figure 3.4 (a) Optical power as a function of blade edge position; (b) Differentiation over power distribution yields the beam shape (squares- derivative data; line- Gaussian fit).

3. 3. 2. Calibration of the ultrasound transducer

The ultrasound fields driven with sine bursts at a central frequency of 1 MHz under moderated pressures (0.1-1.5 MPa) are measured in clean, degassed water using a calibrated PVDB membrane hydrophone (MH, 0.2 mm diameter, SN1502-31, Precision Acoustics, Surrey, UK).

Figure 3.5 shows the schematic of the calibration system. By adjusting the driving signal amplitude at the function generator, the acoustic field generated by the transducer is changed which is recorded with the MH. The signal from the MH is preamplified, digitized and time-averaged (100 sweeps) on an oscilloscope (LT224, LeCroy, NY, USA). The averaged waveform is transferred via GPIB into the PC. The transducer electrical drive signal is also recorded at the output of the IMN. The MH is mounted on an XYZ gantry (not shown) that is driven by stepper motors (Velmex, NY, USA) controlled by the PC.

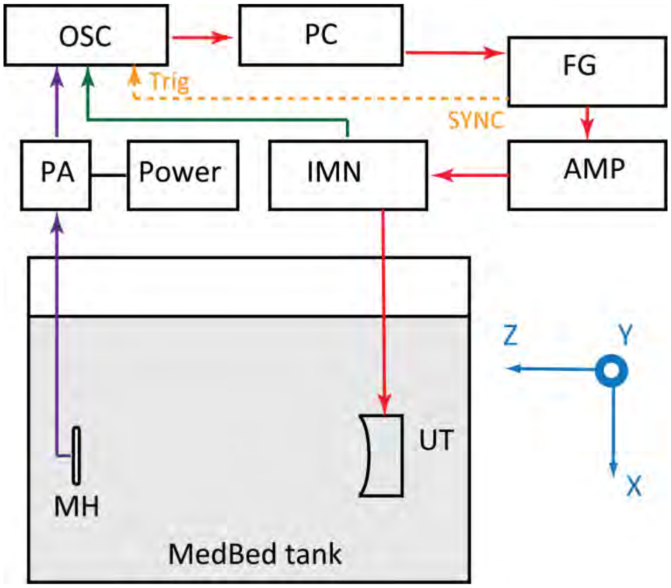

Fig. 3.5 Experimental setup to calibrate the ultrasound transducer in water. MedBed Tank- a big water tank filled with degassed water; MH- membrane hydrophone (placed in the XY plane); PA- MH integrated preamplifier; Power- DC power supply for the PA (0-28 volts); OSC- oscilloscope; other abbreviations please refer to Figure 3.2.

Figure 3.6 shows the normalized peak pressure (mean value of the magnitudes of peak-positive and peak-negative pressures) along the acoustic axis and the radial direction in the focal plane. As seen, the ultrasound focal position is 63 mm away from the transducer, and the FWHM of the focal region is 9x1.5x1.5 mm^3.

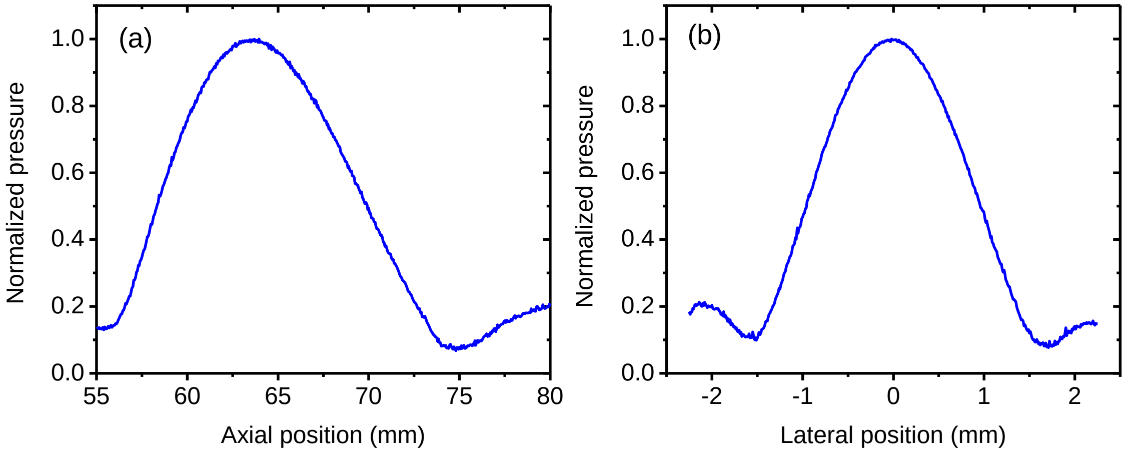

Figure 3.6 Normalized peak pressure (a) along the ultrasound axis and (b) a function of radial distance in the focal plane.

Figure 3.7 shows the acoustic pressure waveforms generated in the focus when the HIFU transducer is driven with sine bursts of varying duration. The transducer reaches a steady state output condition after approximately 7-10 cycles. Because the pulse durations employed in the experiments were often 10 cycles or less, the transducer output had to therefore be calibrated for each pulse duration. With 10 cycle bursts, the focal pressure is shown as a function of IMN output voltage in Figure 3.8 fit by

$$P_{focal} = 0.05746 \cdot V_{IMN} - 0.004336. \qquad (3.1)$$

Note the onset of acoustic nonlinearity for pressure amplitude greater than about 0.9 MPa. With this P-V curve, one is able to monitor and control the focal pressure from the IMN output read on the oscilloscope. Similar calibration curves were produced for all the pulse durations employed in the research.

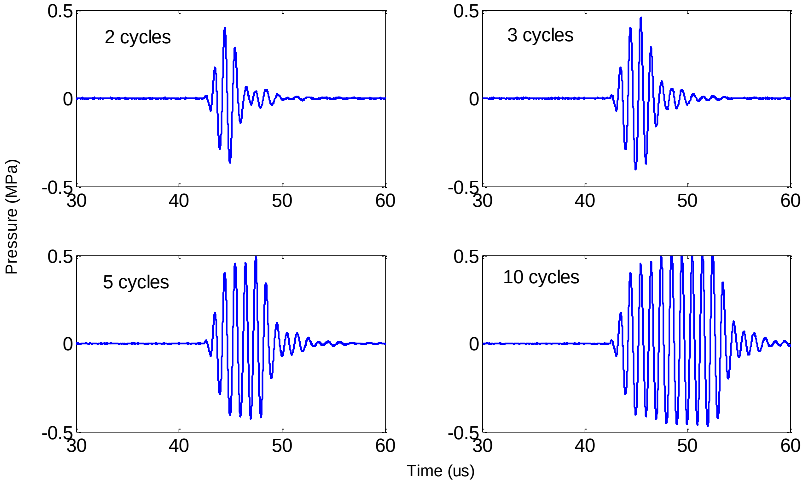

Figure 3.7 Response on the membrane hydrophone at the focal position when driving the HIFU transducer with different cycle numbers bursts at 1 MHz center frequency.

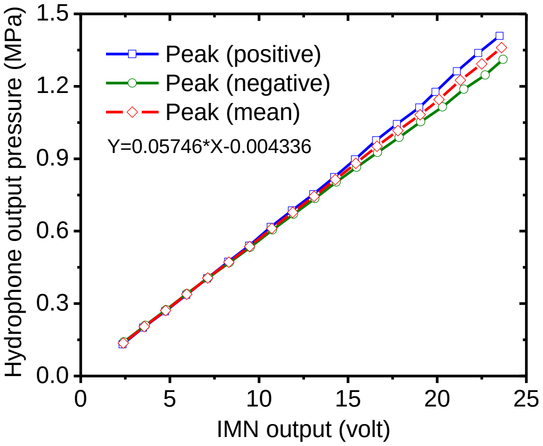

Figure 3.8 Focal pressure amplitude as a function of IMN output voltage (10 cycle pulse).

3. 3. 3. Tissue-mimicking phantoms

In vivo soft biological tissue is the ultimate intended media for AO sensing and imaging. For the early-development experiments described in the sections to follow, tissue-mimicking phantoms and exercised tissues are used for expediency, precise control, and cost.

Tissue phantoms are easily fabricated with controllable geometries, homogeneities and physical properties, and they usually do not deteriorate or age like real tissues. Therefore, phantoms are used for system calibration, optimization, stability and repeatability testing, as well as for quantitative sensing and imaging studies (Pogue and Patterson 2006). However, some important characteristics such as blood/mass flow and inhomogeneities due to microstructures are difficult to duplicate. In an AOI phantom, it is essential that one accurately controls phantom optical properties (μ_a and $\mu_s^{'}$) and acoustical properties (mass density, speed of sound). We use a phantom recipe modified from Ref. (Sathyam and Prahl 1997; Viator and Prahl 1999), where a mixed solution of acrylamide and bisacrylamide is used as the gel matrix material, polystyrene microspheres (Pogue and Patterson 2006) as the optical scatterer, and India ink as the optical absorber. Macroscopic optical inhomogeneities (imaging targets, if you will) are fabricated from the same gel matrix material as the background and infused with differing concentrations of particles and/or ink to produce contrast in optical scattering and/or absorption, respectively. The next two Sections provide details of this procedure.

The addition of either the microspheres or ink does not substantially alter the acoustic properties at 1 MHz, which are summarized in Table 3.2 (Sui 2005). Note that phantoms made from this recipe possess lower acoustic attenuation than human breast, a limitation that is not deemed significant to the work reported herein. Moreover, we make no attempt to reproduce the microstructural heterogeneities or vasculature of real tissues.

Table 3.2 Measured acoustic properties of made phantom versus human breast tissue

Parameter	**Tissue phantom**	**Breast tissue (Duck 1990)**
Mass density (Kg/m^3)	1045	990-1060
Sound speed (m/s)	1515	1450-1570
Attenuation (Np/m/MHz)	0.2	3.4-7.4

3.3.3.1 Scatterer concentration required to achieve a desired phantom $\mu_s^{'}$

The scattering of the phantom in the recipe is determined by the concentration of polystyrene microspheres (07759-15, 0.792 μm of diameter, 1.08x10^{11} spheres/ml, Polysciences, PA, USA) employed in the mixture, which is computed using an online Mie scattering calculator (Prahl 2007).

Table 3.3 Parameters to perform the Mie scattering calculation

Parameter	**Input**
Optical wavelength in vacuum	1064 nm
Refractive index of medium (water)	1.33
Sphere diameter	0.792 μm
Real index of sphere	1.576
Imaginary index of sphere	0
Sphere concentration	C_m spheres/ μm^3

Table 3.3 lists the parameters required to perform the calculation. The resulting anisotropic factor is 0.8, and the reduced scattering coefficient (in units of cm^{-1}) induced by the introduction of microspheres is expressed, given by

$$\mu_s^{'} = 59.0319 \cdot C_m , \qquad (3.2)$$

where C_m (unit: spheres/μm^3) is the microsphere concentration in phantom (solution). It should be noted that the absorption effect due to the polystyrene microspheres is assumed negligible (Passos *et al.* 2005), thus, the imaginary index is listed as zero in Table 3.3.

3.3.3.2 Absorber concentration required to achieve a desired phantom μ_a

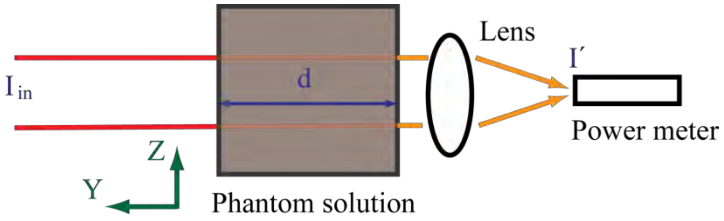

Figure 3.9 Setup to measure the absorption coefficient as a function of India ink concentration in the phantom solution (scatterers are not added).

Fountain pen India ink (Item 46030, Sanford Corp, Ill, USA) is used as the absorber in our study. An arrangement illustrated in Figure 3.9 is used to measure the optical absorption of a phantom “solution” consisting of water (no scattering particles) doped with different concentrations of India ink. According to the Beer’s law, the quantity of light absorbed by the water/ink mixture is directly proportional to the absorption coefficient and the light path length through the sample. Thus we have

$$A = \frac{I_{in} - I'}{I_{in}} = \exp(-\mu_a d)\,, \tag{3.3}$$

where A is the absorbance, I_{in} is the incident light intensity, I' is the transmitted light intensity measured after the sample and d is the path length, which is the Y dimension of the acrylic container holding the sample (21.68 mm). The attenuation due to the acrylic walls of the container and water were measured beforehand and taken into account when calculating the absorption coefficient due to the India ink ($\mu_{a,ink}$). Figure 3.10 shows the measured results and the resulting linear fit, given by

$$\mu_{a,ink} = 32.47 \cdot C_{ink} - 0.014\,, \tag{3.4}$$

where C_{ink} is the volume concentration of ink. With this expression, one is able to accurately determine the amount of India ink required to achieve a desired absorption coefficient within the gel phantom.

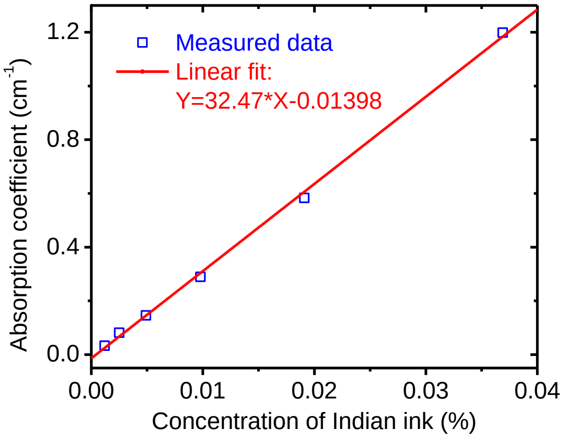

Figure 3.10 Absorption coefficient due to the India ink as a function of ink concentration (squares- experiment data; line- the linear fit).

It should be pointed out that one usually needs to dilute the ink in two steps to achieve a small yet precise concentration. For example, to obtain a C_{ink} of 0.0012%, 0.1 ml ink is first diluted in 20 ml water (giving a C_{ink} of 0.4975%), and then 0.1 ml from the diluted solution is added in another 40 ml water. Moreover, Passos *et al.* (2005) reported that adding India ink for absorption also causes the scattering to change ($\mu_s^{'}$ of 2 cm^{-1} for a μ_a of 90 cm^{-1}). However, since our ink concentrations are much lower than Passos *et al.* ($\mu_a < 5\, cm^{-1}$), this effect is not deemed important.

3. 3. 4. Principle of PRC and its usage for the detection of AO signals

A brief overview of the principle of PRC interferometry for the detection of ultrasound-induced phase modulated light is presented here. Further details can be found in the literature (Saleh and Teich 1991; Solymar *et al.* 1996; Murray *et al.* 2004; Gross *et al.* 2005; Sui 2005; Sui *et al.* 2005).

The photorefractive crystal (PRC) is a material whose index of refraction adaptively varies according to the spatial distribution of incident optical illumination, following procedures shown in Figure 3.11.

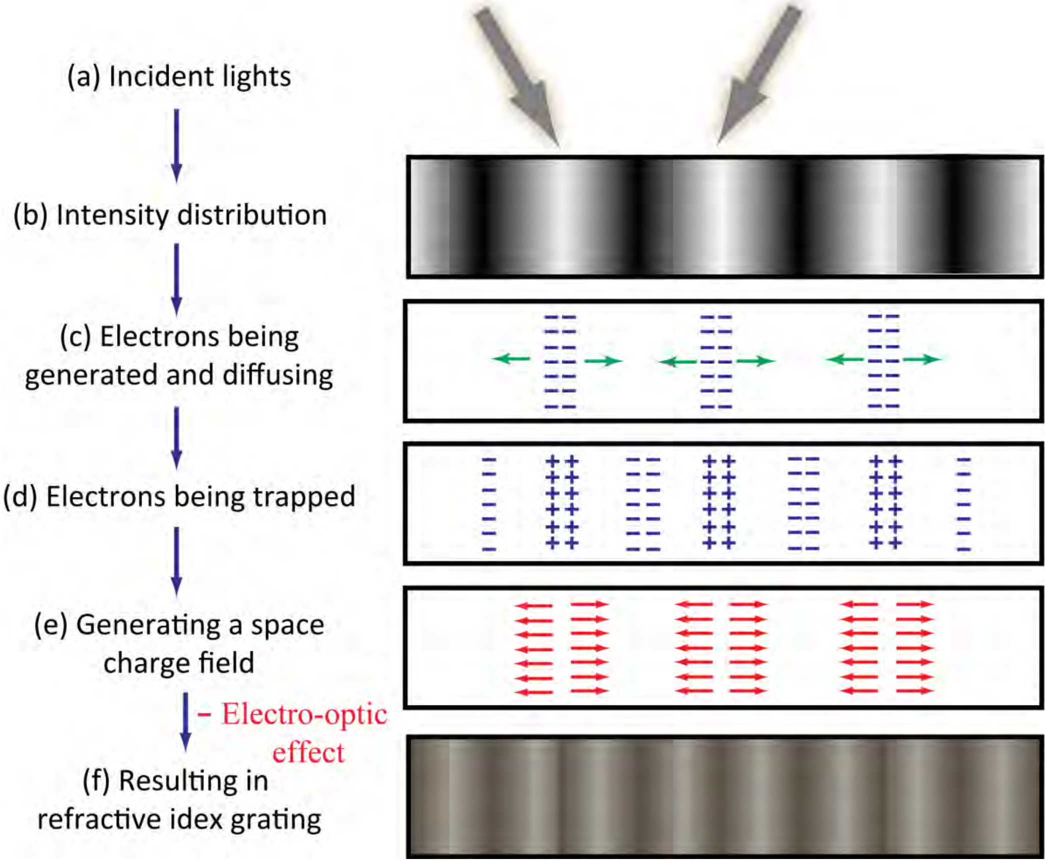
(a) Incident lights
(b) Intensity distribution
(c) Electrons being generated and diffusing
(d) Electrons being trapped
(e) Generating a space charge field
Electro-optic effect
(f) Resulting in refractive idex grating

Figure 3.11 The process that mediates the photorefractive effect by which the spatial distribution of optical illumination alters the refractive index grating of the photorefractive material. [Modified from (Saleh and Teich, 1991)]

A simplest case of two plane waves interfering within the crystal is considered here (Figure 3.11a), which forms a sinusoidal intensity distribution pattern in the material (Figure 3.11b). Light is absorbed in the PRC, and in the bright regions (with high intensities), free carriers like electrons are generated in a process called photogeneration (Figure 3.11c). Because of concentration differences, these electrons diffuse and/or drift from the bright regions (Figure 3.11c)[1], and are trapped in the dark regions (Figure 3.11d), resulting in a non-uniform (periodic) space-charge distribution and an electric field (Figure 3.11e). The time required for the formation of this space charge field is referred to the PRC response time (Millerd *et al.* 1999). Since the material is electro-optic, the internal electric field locally modifies the index of the refraction, forming a refractive index grating inside the crystal (Figure 3.11f), which stores the unique magnitude and phase information of the incident beam regardless of its complexity.

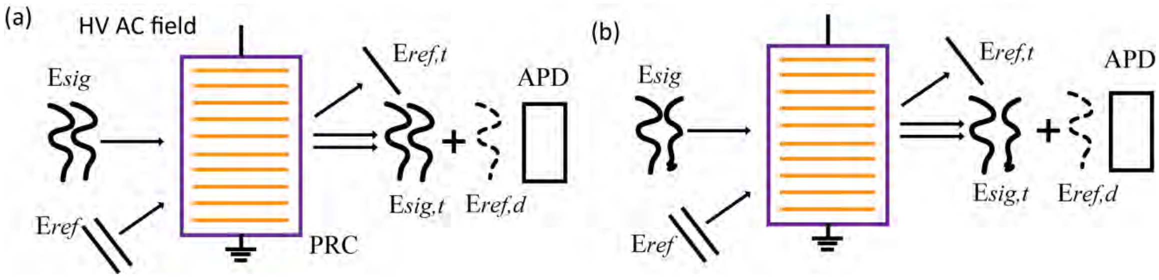

Figure 3.12 Photorefractive two-wave-mixing (TWM) effect with (a) the absence and (b) the presence of the ultrasound modulation. E_{sig} is the scattered (signal) beam collected from the diffuse sample, E_{ref} is the reference beam, $E_{sig,t}$ and $E_{ref,t}$ are the transmitted signal and reference beams through the PRC, respectively, and $E_{ref,d}$ is the reference beam energy diffracted into the direction of signal beam.

Figure 3.12 illustrates the usage of PRC for the detection of ultrasound-induced modulation on diffuse light. The incident signal beam is multiply scattered and phase modulated by the ultrasound in the turbid medium, and then it is collected and sent to the PRC, where it is written as E_{sig} and interferes with the reference beam (E_{ref}). These two beams set up an interference pattern, which is recorded in the PRC in a form of index of refraction grating. Off this grating, two beams exchange energy, a process usually referred to as TWM or two-beam-coupling. As a result, part of E_{ref} is diffracted into the direction of the transmitted signal beam ($E_{sig,t}$). The index grating adapts itself to low frequency variations in the signal beam. Therefore in the absence of ultrasound modulation (Figure 3.12a), the diffracted reference beam ($E_{ref,d}$) is an exact replica of E_{sig}. Thus, $E_{sig,t}$ and $E_{ref,d}$ are perfectly in phase and interfere constructively, obtaining a maximum optical intensity voltage at the photodetector positioned in the direction of E_t. In the presence of ultrasound modulation (Figure 3.12b) and if the temporal duration of AO interaction (which is determined by ultrasound pulse as light is continuously on in the study) is short with respect to the crystal response time, the perturbations in the signal beam are not "written" into the grating because the PRC (charge field formation) cannot respond fast enough. Thus the index grating inside the PRC remains stationary, and so does the diffracted reference beam ($E_{ref,d}$). Since E_{sig} is partially phase shifted due to the ultrasound, $E_{sig,t}$ and $E_{ref,d}$ in this case are therefore no longer in phase, and the interference between them results in a reduction in the light detected by the APD.

---

[1] The application of an external electrical field can enhance this process and subsequently the formation of the index grating (Millerd *et al.* 1999).

It should be emphasized at this point that the PRC's adaption in the index grating to low frequency disturbances is key to AOI for i*n vivo* applications. If the PRC response time is relatively slow, e.g. on the order of 150 ms for BSO (Sui 2005), the 0.1-1 ms-scale physiological motions *in vivo* (Gross *et al.* 2009) could induce extra phase shifts to the signal beam that are also "written" into the PRC index grating, causing a speckle de-correlation on AO signals. Therefore, a faster response time is required, which is feasible by choosing the right photorefractive material and increasing the intensity of the incident beams (Millerd *et al.* 1999).

The collected scattered field outside the sample from one speckle corresponding to optical path s is given by

$$E_{sig,s} = E_s + [E_s \exp(i\Phi_s) - E_s], \tag{3.5}$$

where we explicitly separate the stationary contribution (E_s) from the bracketed terms that are modulated by the ultrasound on a time scale of one microsecond or less, depending on the acoustic frequency. In the crystal, only the stationary contribution is amplified with a TWM gain of γ as the reference beam is diffracted into the signal beam direction, as discussed above, whereas the other terms in Eq. (3.5) is not amplified because it fluctuates over a time scale that is much shorter than the response time of PRC (between 10-20 ms in our setup); on the microsecond time scale, the PRC refractive index grating is essentially "frozen". Considering the absorption due to the PRC, the field after passing through the PRC can be written as

$$\begin{aligned} E_{sig,s} &\to \exp(-\alpha L/2)\left\{E_s \exp(\gamma L) + [E_s \exp(i\Phi_s) - E_s]\right\} \\ &= \exp(-\alpha L/2) E_s \left\{\exp(\gamma L) + [\exp(i\Phi_s) - 1]\right\} \end{aligned} \tag{3.6}$$

with α and L representing the absorption coefficient and optical length of the crystal, respectively. Therefore, when a large-aperture detector (such as the 5-mm diameter avalanche photodiode used in this study) is used to detect light from multiple speckles, the resulting detected signal can be expressed by (Delaye *et al.* 1995; Murray *et al.* 2004; Blonigen *et al.* 2005)

$$I_{SE} = \exp(-\alpha L)\sum_{s} \left|E_s\right|^2 \left(\left|\exp(\gamma L)\right|^2 + 2\,\mathrm{Re}\{[\exp(\gamma L) - 1]^*[\exp(i\Phi_s - 1)]\} \right), \qquad (3.7)$$

where the TWM gain coefficient in the signal beam is defined as $\gamma = \gamma^{'} + i\gamma^{"}$, with $\gamma^{'}$ and $\gamma^{"}$ representing the real and imaginary parts. The quantity $\left|E_s\right|^2$ is the light intensity contribution from one speckle following optical path s in the absence of ultrasound modulation. The quantity Φ_s is the accumulated phase shift from optical path s given by

$$\Phi_s = -\left|\Phi_s\right| \sin(\omega_a t - \chi_s) = \mathrm{Re}\left\{-i\left|\Phi_s\right| \cdot \exp[-i(\omega_a t - \chi_s)]\right\} , \qquad (3.8)$$

where the magnitude $\left|\Phi_s\right|$ is related with phase increment terms due to ultrasound-induced perturbation ($\Delta\varphi_{s,U}$ in Eq. 2.14) and the optical path s -dependent term χ_s (related with φ_s in Eq. 2.13) is distributed *randomly* between 0 and 2π for different paths in highly diffuse medium.

Returning to Eq. (3.7), the first term in the bold parentheses under summation represents the background optical signal that would be measured in the absence of ultrasound modulation, and the remaining terms are dependent on the ultrasound-induced phased shifts and the specific optical path, which is referred to as modulated signal (MS). When multiple speckles from different optical paths are detected with one large aperture photodetector, signals from different speckles are not expected to sum coherently. Instead there is a reduction in modulation depth (MD) as discussed in Chapter 2. Equation (3.7) also shows that PRC is essential to the detection of ultrasound-induced modulation of diffuse light in that the modulated signal increases in proportion to $\exp(\gamma L)$ as PRC TWM gain increases, and it vanishes when there is no TWM effect ($\gamma = 0$).

By calculating the Bessel series expansion of $\exp(i\Phi_s)$ and retaining the lowest-order terms, Eq. (3.7) can be expressed as the sum of the following two terms (Blonigen *et al.* 2005):

$$I_{SE}^{AC} = 4\exp(-\alpha L)\exp(\gamma' L)\sin(\gamma'' L)\sum_s |E_s|^2 J_1(|\Phi_s|)\sin(\omega_a t - \chi_s)\,, \tag{3.9}$$

$$I_{SE}^{DC} = 2\exp(-\alpha L)\exp(\gamma' L)\cos(\gamma'' L)\sum_s |E_s|^2 \left[J_0(|\Phi_s|) - 1\right]. \tag{3.10}$$

Note that presence of both time independent and time dependent terms. Equation (3.9) describes the "AC" component of the signal, which is modulated at the ultrasound frequency, ω_a. This vanishes quickly for, when light propagates through turbid media, the path-dependent variable χ_s is randomly distributed between 0 and 2π. Equation (3.10) describes the additional "DC offset" component to the signal that is independent of the path and depends only on the magnitude of ultrasound-induced phase modulation. This allows for coherent summation of individual contributions from different optical paths. *It is this DC component (Eq. (3.10)) that we term the "AO signal" used for sensing and imaging in our study.*

To maximize the magnitude of AO signal, the signal beam and reference beam are set to be in phase, giving a pure (real) photorefractive gain, i.e., $\gamma'' = 0$ and $\gamma = \gamma'$. Thus, the AC component of the detected signal becomes zero, and the DC component can be written as

$$I_{AOS} = 2\exp(-\alpha L)\exp(\gamma L)\sum_s |E_s|^2 \left[J_0(|\Phi_s|)-1\right]. \tag{3.11}$$

When there is no ultrasound modulation ($|\Phi_s|=0$), $J_0(|\Phi_s|)-1=0$, there is no AO signal. In the presence of ultrasound modulation, I_{AOS} is negative, suggesting a DC offset in light intensity with respect to I_0. The stronger is the ultrasound modulation, the larger is the magnitude of I_{AOS}.

3. 3. 5. Optimization of PRC TWM gain and diffuse light collection

In accordance with Eq. (3.11), optimizing the PRC TWM gain and diffuse light collection is critical for the detection of the AO signal.

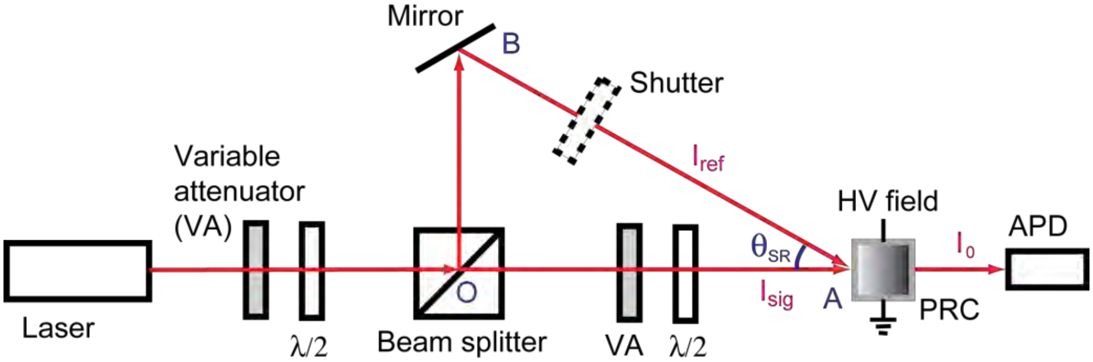
Mirror
B
Shutter
I_{ref}
Variable attenuator (VA)
HV field
APD
θ_{SR}
I_0
O
I_{sig}
A
PRC
Laser
λ/2
Beam splitter
VA
λ/2

Figure 3. 13 Schematic diagram to characterize the TWM gain coefficient

The setup illustrated in Figure 3.13 is used to characterize the PRC TWM gain coefficient in the air, which is measured from the ratio of intensity of the detected signal beam (I_0) with and without the reference beam in the absence of ultrasound modulation:

$$\Gamma = \frac{I_{0,\text{reference ON}}}{I_{0,\text{reference OFF}}} = e^{\gamma L}. \tag{3.12}$$

A series of measurements were taken to characterize the TWM gain as a function of θ_{SR} (angle between the signal and reference beam), β (beam ratio, I_{ref}/I_{sig}), I_{ref} and E_{ext} (applied electrical field voltage, peak to peak). During the measurements, I_{sig} and I_{ref} was adjusted through a combination of variable attenuators, half-wave plates and a beam splitter. The distance between the beam splitter and the surface of the crystal ($|OA|$) is fixed at 17 inches, and the distance between the beam splitter and the mirror ($|OB|$) is made variable in order to alter the angle θ_{SR}. A camera shutter is used to control the ON/OFF of the reference beam (and ON/OFF of TWM) at a shitter speed of 0.14 ms. Other parameters used in the experiment are listed in Table 3.4, and the measured results are shown in Figure 3.14 (a)-(d).

Table 3.4 Experiment parameters for PRC TWM characterization

Figure	I_{sig} (mW/cm^2)	I_{ref} (mW/cm^2)	θ_{SR} (^{0})	HV AC electrical field	
				Frequency (kHz)	Voltage (kV/cm, p-p)
(a)	1.18	320	Varied	2.1	7.14
(b)	Varied	31	5	2.1	7.14
(c)	1.18	Varied	5	2.1	7.14
(d)	1.18	320	5	2.1	Varied

Figure 3.14(a)-(c) show that the application of an external high voltage AC electric field greatly enhances the TWM gain effect, and this enhancement increases with the voltage of the external field applied across the PRC as Figure 3.14(d) shows. However, there is an upper limit to the voltage we can apply while avoiding overheating or unstable beam coupling over a long time scale. In our system, a electric field strength of 7.14 kV/cm (peak-to-peak) is used. Under such an external field, as shown in Figure 3.14 (b) and (c), the TWM gain increases proportionally with β and I_{ref}. This suggests that pumping more optical power into the reference beam will help to increase the TWM gain, and sequentially, the sensitivity to AO signals in AOI. In addition, more optical power on the PRC will also speed up the temporal response of the crystal. However, we have limited power output from the laser source and we wish to retaining sufficient energy in I_{sig}. Therefore, I_{ref} is set ~15 mW/cm^2 in our system unless otherwise mentioned.

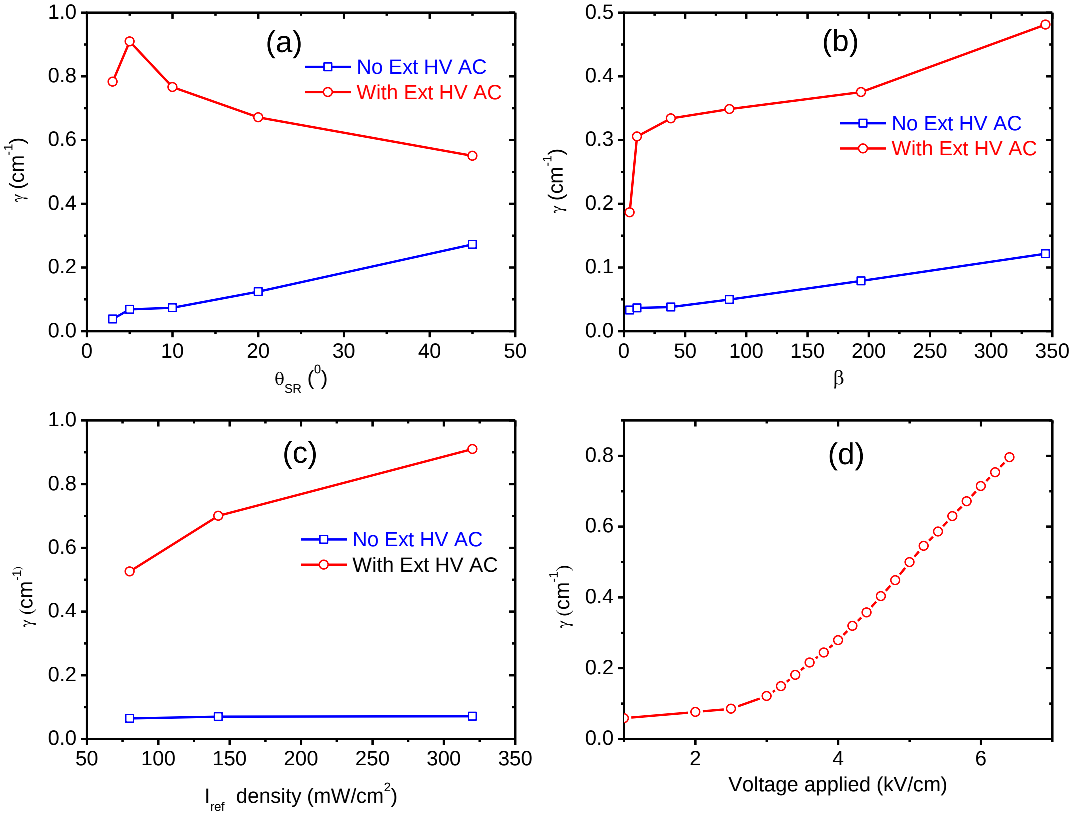

Figure 3.14 TWM gain coefficient as a function (a) θ_{SR} (b) β (c) I_{ref} and (d) E_{ext}. The squares are the data when no external high voltage field is applied across the PRC and the circles correspond to the data with external high voltage field.

We can see from Figure 3.14(a) that when signal and reference beams have an interfering angle around 5^0, one obtains optimum TWM gain, which is also indicated in Figure 3.15(a). This, however, should be balanced with the efficiency of diffuse light collection, which is governed by the theory of etendue, which specifies the geometric capability of an optical system to transmit and accept light. Light collection efficiency is constrained by the least optimized segment in an entire optical system (Cassarly 2002;

Lerner and Thevenon 2010). For a conical beam normal to a source of area S, etendue can be expressed as

$$G = \pi S \sin^2 \Omega . \tag{3.13}$$

It is found the etendue of the PRC is the smallest among all the components in our optical detection scheme, and thus limits the diffuse light collection capability of the whole system. In our setup, θ_{SR} and the half of the solid angle ($\Omega / 2$) for the PRC are identical, which means a small θ_{SR} for optimum TWM effect results in a correspondingly low collected light intensity. It is thus a trade-off between optimum TWM effect and maximum light collection efficiency.

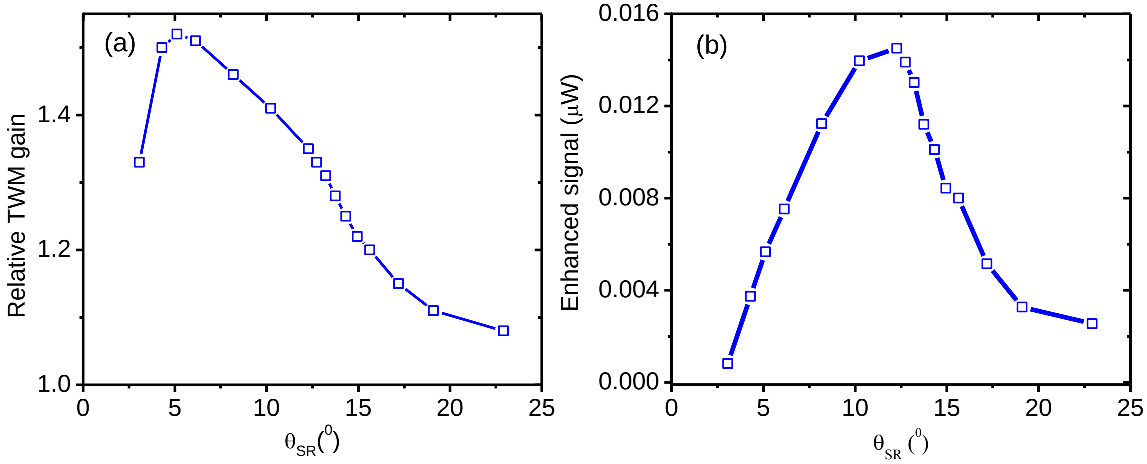

Figure 3.15 (a) The relative TWM gain coefficient (Γ) and (b) enhanced signal beam intensity as a function of θ_{SR}.

We measure the enhanced signal beam due to the TWM, i.e., $I_{ref,d}$ in Figure 3.12, as a function of θ_{SR} (Figure 3.15b). As we can see, the best response is achieved using an angle of 10-13^0. This value is therefore used in the system.

3. 3. 6. System noise characterization

As mentioned earlier in the dissertation, the ambient vibrations and physiological motions *in vivo* induce extra speckle de-correlation to the AO interaction. Beyond that, the potential noise sources in the experimental setup include contributions from both the optical and the ultrasound systems. Shot noise and thermal noise determine the limit of detection and are inherent within the electronic devices. We measure the variance of transmitted signal beam (in the absence of ultrasound modulation) into the APD using the Krohn-Hite active filter (Figure 3.2). The variance is defined by

$$\sigma^2 = \sum_{i=1}^{M} (\bar{X} - X_i)^2 / M , \tag{3.14}$$

where $\bar{X}$ is the mean value of a time domain intensity (voltage) sequence X , X_i is the value of the ith element in the sequence, and M is the total number of elements in the sequence.

Figure 3.16 shows the variance as a function of light intensity through diffuse media with attenuation and scattering coefficients $\mu_a = 0.14\,cm^{-1}$ and $\mu_s^{'} = 8\,cm^{-1}$. As we can see, when light intensity is smaller than 0.007 µW (highlighted with the circle), thermal noise dominates in the system; above this intensity, shot noise (including laser noise) increases approximately linearly which can be fitted as

$$N_{sig} = 2.9\times10^{-6} + 3.5\times10^{-5} \times (I'_{sig,t} - 0.007), \qquad (3.15)$$

where $I'_{sig,t}$ is the amplified $I_{sig,t}$.

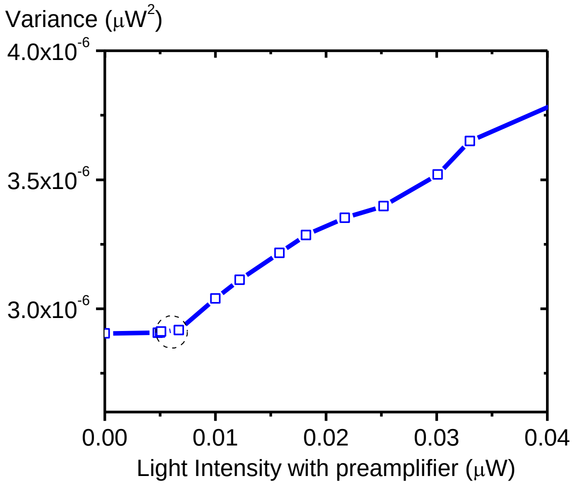

Figure 3.16 Light variance as a function of amplified $I_{sig,t}$

From Eq. (3.15), one is able to estimate the variance of the optic signals through a diffuse sample based on the signal beam intensity that can be computed from the aforementioned diffusion equation (DE) provided sample geometry and optical properties.

In order to reduce the noise level, in our study the optical table is isolated by air from the environment vibrations. When pulsed ultrasound is applied to generate the AO interaction, the collected AO signals are averaged coherently over many (typically 1,000-10,000) acoustic sweeps to achieve AO signals with reasonable SNR (Sui 2005, Lai *et al.* 2009).

Chapter 4

Quantitative Measurement of Optical Properties in Diffuse Media Using Pressure Contrast Acousto-Optic Imaging

4. 0. Overview

A new approach, referred to as pressure contrast AOI, is proposed in this chapter to quantify the measurement of optical properties using acousto-optic imaging. In Section 4.1, several examples of general AOI scan lines obtained with the system developed in Chapter 2 are illustrated, showing that relating standard AO signal with optical properties of the sample is challenging. The concept of studying the ratio of signals generated at two different ultrasound pressure amplitudes is proposed in Section 4.2. In Section 4.3, we detail the related methods and materials, and experimental results demonstrating the feasibility of this new approach for quantitative optical characterization are given in Section 4.4. Discussions of pressure contrast AOI, and its relation to ultrasound modulation mechanisms, are given in Section 4.5 and 4.6, respectively.

4. 1. Introduction

In Chapter 2, we showed that by employing the PRC as the interferometer to demodulate the ultrasound-induced phase modulation, one obtains an “intensity” modulation expressed by Eq. 3.10. The magnitude of this AO signal strength is rewritten in the form

$$\left|I_{AOS}(t)\right| = \chi\left(\eta(z,t)\right)\left(\nu(\alpha,\gamma)\right)\frac{1}{N}\sum_{s=1}^{N}\left[1-J_0\left(\left|\Phi_s(P(P_f,z,t),l_{tr})\right|\right)\right], \tag{4.1}$$

where χ is a constant and $\eta\left(z,t\right)$ gives the intensity of modulated light reaching the detection system and depends on the spatial extent of the ultrasound pulse, the amount of light reaching the interaction region, and the probability that the modulated light will be collected. The third term, $\nu(\alpha,\gamma)$, characterizes the detection efficiency of the photorefractive crystal and is a function of the absorption in the crystal (α) and TWM gain coefficient (γ). The forth term, N , represents the total number of optical paths. Referring to the term in the brackets, Φ_s gives the accumulated phase shifts over propagation path s through the interaction region, which, as discussed in Chapter 2, is affected by, among other factors, the *in situ* pressure amplitude and the local optical transport mean free path ($l_{tr} = 1/(\mu_a + \mu_s^{'})$). The *in situ* pressure amplitude, P , is a function of focal pressure amplitude (P_f) , spatial position along the vertical axis with respect to the transducer (z), and time (t). $t = 0$ corresponds to the moment when the ultrasound pulse is generated at the transducer. In stating the magnitude of general AO signals in this form (Eq. (4.1)), we assume that light incident on the AO interaction region is relatively uniform with respect to ultrasound field distribution and the contributions to the total light intensity from each individual optical paths that eventually enter the photodetector are approximately even.

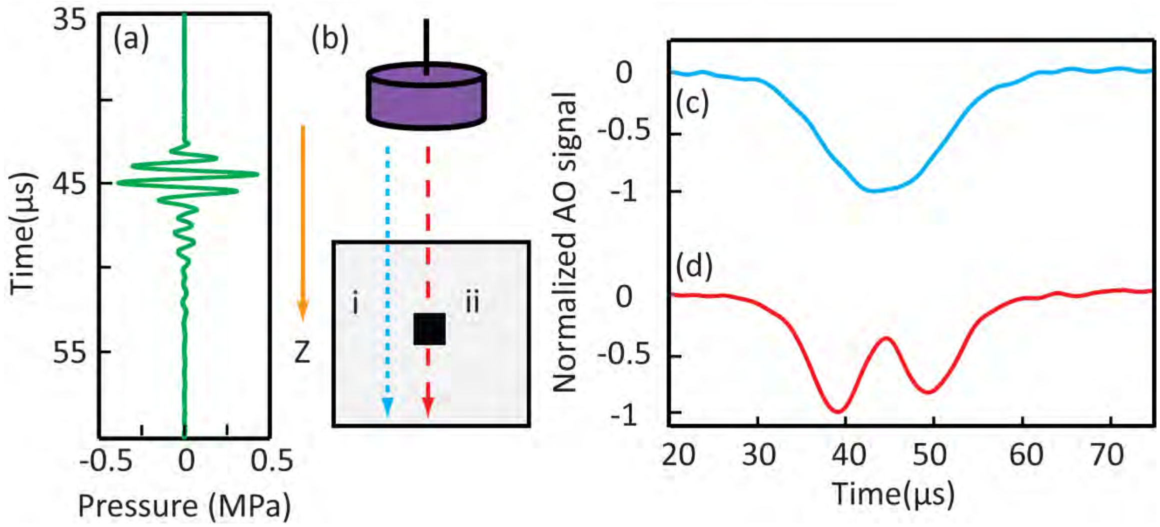

Figure 4.1 (a) The 2-cycle, 1MHz ultrasound pulse used to generate the AO response around the focal position; (b) The ultrasound pulse propagates along the Z direction across the phantom portion (i) without and (ii) with an optically absorbing inclusion; (c) and (d) AO signal waveforms corresponding to scenario (i) and (ii), respectively.

The two-cycle, 1.0 MHz ultrasound pulses with 0.4 MPa focal pressure [1] shown in Figure 4.1(a) were used to generate the AO interaction in a diffuse phantom dimensioned $40\times23\times40$ mm^3 along XYZ-axes with $\mu_a = 0.14\,cm^{-1}$ and $\mu_s^{'} = 4\,cm^{-1}$, which is embedded with an optically absorbing inclusion ($5\times5\times5\,mm^3$, $\mu_a = 3\,cm^{-1}$, $\mu_s^{'} = 4\,cm^{-1}$) at its center (see Figure 4.1 (b)). Figure 4.1 (c) shows a typical AO signal when the ultrasound pulses propagate through the phantom outside of the inclusion (scenario i in Figure 4.1b). The signal was coherently averaged over 10,000 sweeps to improve the SNR. As we can see, the light intensity at the detector is reduced whenever/wherever there is overlap of light and sound. When time is around 45 μs, corresponding to the focus of the ultrasound field, the modulation is highest because both *in situ* light and sound are strongest. Thus one gets minimum light intensity at the detector forming the valley of the "V-shaped" AO signal in response to an optically homogenous region. In the signal shown, the background light level was subtracted and the displayed scan line is normalized to the minimum value.

---

[1] Unless otherwise noted, peak positive pressures are referred to in this chapter.

In comparison, Figure 4.1(d) shows a (normalized) AO scan line obtained when the ultrasound pulses are scanned over a portion of the same phantom containing an absorbing inclusion (scenario ii in Figure 4.1b). A rise in the signal is observed around 45 μs, indicating that the strength of AO modulation is diminished when the ultrasound pulse traverses the center of the absorbing target. This occurs because the total number of photons within the AO interaction volume that are modulated by the ultrasound field and eventually enter the photodetector is greatly reduced due to the high absorption coefficient. It is this "W-shaped" AO signal that is used as the signature of the absorbing inhomogeneity in AOI. In addition, according to the study in Chapter 2, the magnitude of the phase modulation is also reduced for increased absorption and/or scattering. These are the essential mechanisms for the detection of optical inhomogeneities within scattering media in AOI.

Relating the strength of AO signal to the exact optical properties of the interaction region is, however, complicated by the fact that besides local optical properties the signal strength is also affected by many other factors as discussed in reference to Eq. (4.1). In order to extract *quantitative* information about the local optical properties based on standard AO response, Bal and Schotland (2010) proposed an inversion algorithm based on the diffuse approximation (DA) to the light radiative transport equation (RTE, briefly introduced in Chapter 2), which is similar to those employed for diffuse optical tomography (Arridge 1999; Arridge and Schotland 2009; Bal 2009). Another potential solution is to measure the AO signals at multiple optical wavelengths and use the spectral information to infer, for example, the composition of the media within the AO interaction region (Kim and Wang 2007).

4. 2. Pressure contrast AOI

Focusing on a different aspect, the role of ultrasound pressure in the ultrasound-induced modulation, we propose a new sensing mechanism in this chapter to quantify the optical measurement based on the general AO signals.

Eq. (4.1) shows that only the last term, the accumulative phase shift along the specific optical path s, is affected by the ultrasound field pressure and optical properties within the AO interaction region. So, if we generate the AO interaction with two different ultrasound focal pressure amplitudes of P_{f1} and P_{f2} ($P_{f1} < P_{f2}$), two AO signals such as those shown in Figure 4.2 can be obtained.

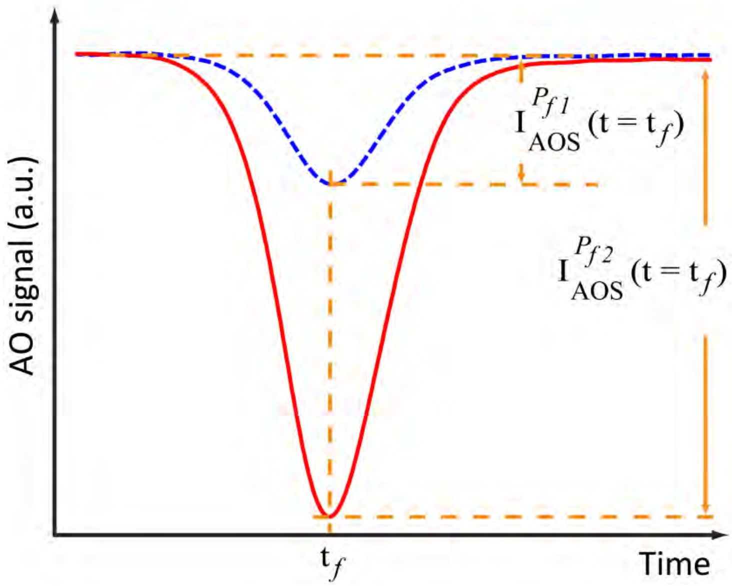

Figure 4.2 Two AO signal waveforms generated with two different ultrasound focal pressure amplitudes (dashed curve for lower pressure, P_{f1}, and real curve for higher pressure, P_{f2}) within a diffuse phantom ($\mu_s^{'} = 5\,cm^{-1}$). Both waveforms were averaged over 10,000 times with a PRF of 1 kHz.

The two AO signals shown in Figure 4.2 are denoted as $\left|I_{AOS}^{P_{f1}}\right|$ and $\left|I_{AOS}^{P_{f2}}\right|$. The division of them yields a ratio, which is given by:

$$\frac{\left|I_{AOS}^{P_{f2}}\right|}{\left|I_{AOS}^{P_{f1}}\right|} = \frac{\sum_{s=1}^{N}\left[1 - J_0\left(\left|\Phi_s(P(P_{f2}, z, t), l_{tr})\right|\right)\right]}{\sum_{s=1}^{N}\left[1 - J_0\left(\left|\Phi_s(P(P_{f1}, z, t), l_{tr})\right|\right)\right]}. \qquad (4.2)$$

As we can see, this ratio is independent of the intensity of modulated light reaching the detection system (η) and the characteristics of the detection scheme itself (ν), but is rather only dependent on the shape of the ultrasound pulse and the local optical properties

(l_{tr}) of the AO interaction region. The spatial distribution of ultrasound pressure changes as the pulse propagates along the Z axis, resulting in the temporal variations in the AO signal shown in Figure 4.2. For quantitative measurements, in this study we consider the ultrasound pressure distribution at time t_f when pulse is centered about the focal plane at z_f. The ratio of two AO signal amplitudes at this position, is defined as the pressure contrast signal (PCS) :

$$PCS = \frac{\left| I_{AOS}^{P_{f2}}(t = t_f) \right|}{\left| I_{AOS}^{P_{f1}}(t = t_f) \right|}. \tag{4.3}$$

In the following sections, we will show that such PCS may be calibrated at a particular set of P_{f1} and P_{f2} with a constant ultrasound pulse shape, which allows for (a) quantitative measures of optical properties of homogeneous media, (b) detection and imaging of embedded optical inhomogeneities in turbid media, and (c) quantitative measures of optical properties of the embedded inclusions without *a priori* knowledge of the background media.

4. 3. Methods and materials

4.3.1. AOS strength dependence on ultrasound focal pressure

The AOS strength measured as a function of ultrasound focal pressure across a homogenous phantom (40x25x40 mm^3 along the XYZ-axes) with a reduced scattering of 7 cm^{-1} is shown in Figure 4.3. For this experiment, three-cycle, 1 MHz ultrasound pulses were used to elicit the AO response with focal pressure amplitude increased from 0.3 MPa to 1.5 MPa in steps of 0.1 MPa. At each pressure, the AO waveforms were averaged over 20,000 sweeps and this process was repeated 8 times to obtain a mean AO scan line, from which the AOS strength was recorded.

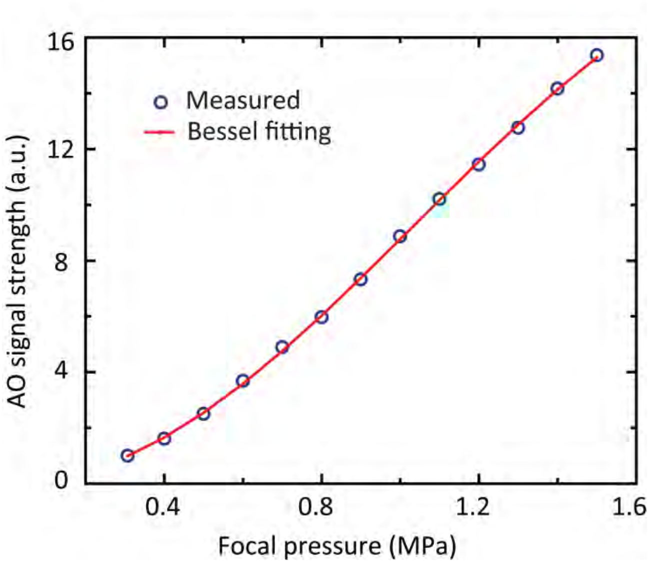

Figure 4.3 Measured AO signal strength as a function of applied ultrasound focal pressure amplitude in a homogeneous phantom ($\mu_s^{'} = 7\,cm^{-1}$). The discrete circles are the measured data and the real line is the curve fit using the function $S = \kappa\left[1 - J_0(\beta P_f)\right]$.

Assuming the phase shift due to the ultrasound in Eq. (4.1) is linearly proportional to the applied focal pressure, this phase shift around the focal position for optical path s is written as

$$\Phi_s = \beta P_f , \tag{4.4}$$

with β being directly related to the optical properties (l_{tr}) within the AO interaction region, and a larger value of β indicating higher phase shifts induced by the same ultrasound field. Thus, the experiment data shown in Figure 4.3 is fit with a model:

$$S = \kappa\left[1 - J_0(\beta P_f)\right], \tag{4.5}$$

where constant κ is used to represent the terms of $\chi\left(\eta(z,t)\right)\left(\nu(\alpha,\gamma)\right)$ in Eq. (4.1). As shown in Figure 4.3, Eq. (4.5) shows excellent agreement with the experiment data, despite it is just an empirical function and it is only equivalent to Eq. (4.1) under the condition that

$$\frac{1}{N}\sum_{s=1}^{N}\left[1 - J_0\left(\left|\Phi_s(P, l_{tr})\right|\right)\right] \approx 1 - J_0\left(\beta P_f\right), \tag{4.6}$$

meaning that the accumulated phase shifts along each optical path contribute equally to the net phase shift of the whole collected scattered light, i.e., $\Phi_s = \Phi = \beta P_f$. Nevertheless, Eq. (4.5) provides a simple but useful means for interpreting the strength of direct AOSs, and more importantly, for interpreting the measurements in pressure contrast AOI in terms of the constant β

$$PCS = \frac{1 - J_0\left(\beta P_{f2}\right)}{1 - J_0\left(\beta P_{f1}\right)}. \tag{4.7}$$

4.3.2. The selection of ultrasound focal pressure amplitudes

To study how PCS is affected by ultrasound pressure amplitudes, the zero-order Bessel function shown in Eq. (4.7) is expanded under the assumption of moderate ultrasound modulation (stated in Chapter 2), written by

$$J_0(x)=\sum_{m=0}^{\infty}\frac{(-1)^m}{m!\Gamma(m+1)}(\frac{x}{2})^{2m}\ , \tag{4.8}$$

where the Gamma function $\Gamma(n)=(n-1)!$. Therefore, the zero-order Bessel function can be expressed as

$$J_0(x)=1-\left(\frac{x}{2}\right)^2+\frac{1}{4}\left(\frac{x}{2}\right)^4-\frac{1}{36}\left(\frac{x}{2}\right)^6+....\ , \tag{4.9}$$

and

$$1-J_0(x)=\left(\frac{x}{2}\right)^2-\frac{1}{4}\left(\frac{x}{2}\right)^4+\frac{1}{36}\left(\frac{x}{2}\right)^6+.....\tag{4.10}$$

Referring this back to Eq. (4.7), it is evident that if only the first nonzero term in the expansion series of $1-J_0(x)$ is kept, the PCS is independent of β, and the concept of pressure contrast AOI is no more applicable. Instead, the expansion terms beyond the second order are required to retain the PCS dependence on β and local optical properties, which suggests one (at least) of the two pressure amplitudes has to be sufficiently high (but without exceeding the safety guidelines by US Food and Drug Administration regulation (1997)) so that the higher order terms in Eq. (4.10) are non-negligible.

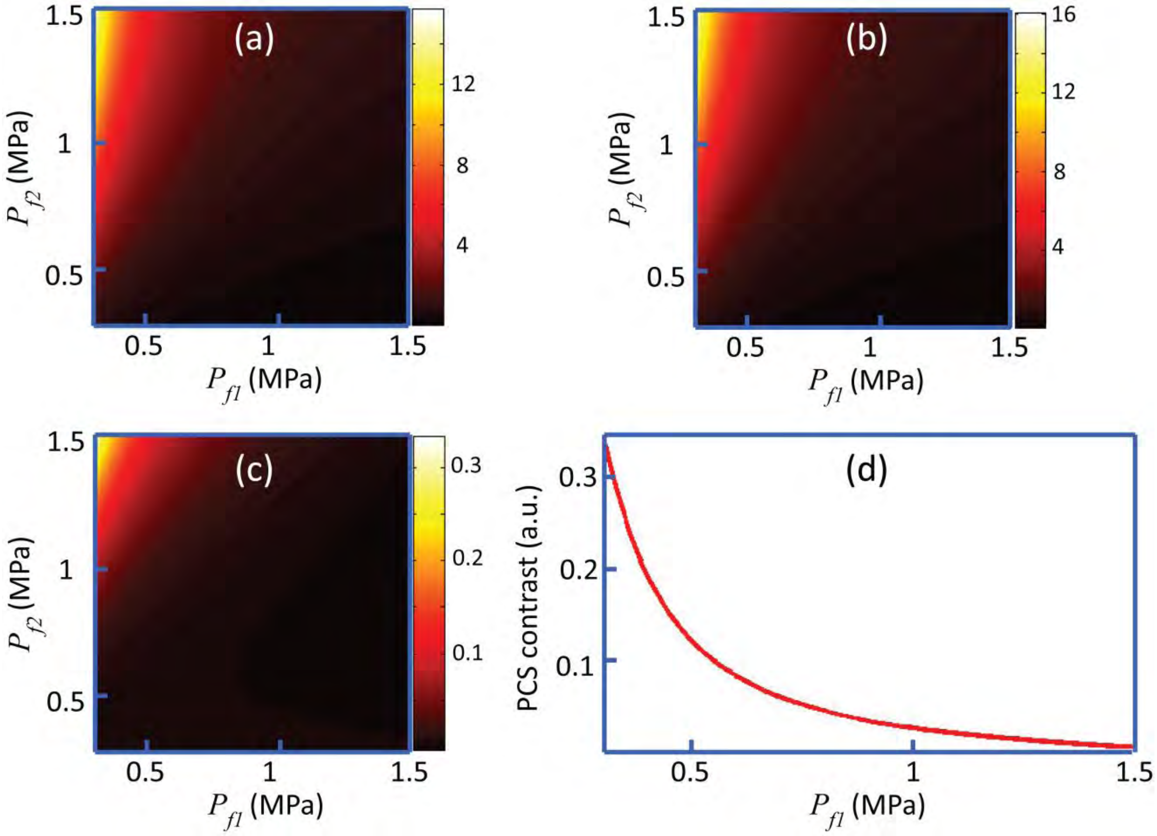

Figure 4.4 Simulated PCS as a function of focal pressure amplitude pair for reduced scattering coefficient of (a) 6 cm^{-1} and (b) 7 cm^{-1}(same absorption of 0.14 cm^{-1}). The color bar corresponds to the PCS value. (c) Simulated PCS contrast between small optical changes in diffusivity (7 cm^{-1} and 6 cm^{-1}) as a function of pressure amplitude pair, and in (d) the PCS contrast is plot as a function of lower pressure amplitude when the higher pressure amplitude is fixed at 1.5 MPa.

Meanwhile, we performed numerical simulations of PCS as a function of selected pressure amplitudes with β values estimated from experimental data in diffuse homogeneous media. Figure 4.4(a) and (b) show the simulated PCS as a function of focal pressure amplitude pair in phantoms with reduced scattering coefficients of 6 and 7 cm^{-1}, respectively. The color bar indicates the value of PCS computed at each point between a higher pressure amplitude (along the Y axis) and a lower pressure amplitude (along the X axis). Figure 4.4(c) illustrates the differences in simulated PCS, referred to as PCS contrast, between 7 and 6 cm^{-1} as a function of pressure amplitude pair, and in Figure 4.4(d) the obtained PCS contrast is plot as function of the lower pressure amplitude (P_{f1}) from 0.3-1.5 MPa when the higher pressure amplitude (P_{f2}) is fixed at 1.5 MPa.

These simulations suggest that the highest sensitivity of detection using the PCS among small changes in optical properties occurs when the higher pressure is as high as possible (limited by the safety considerations (US Food and Drug Administration 1997)) while the other pressure should be as low as possible (limited by the dynamic range of the detection system and noise source). In our study, focal pressures of 1.5 and 0.3 MPa are used respectively as the higher and lower pressures.

4.3.3. Determination of PCS experimentally

In order to perform PCS measurements experimentally, a user-defined pulse shown in Figure 4.5(a), with the inset showing the excited pulse from the function generator shown in Figure 3.2, which is amplified and used to drive the ultrasound transducer to generate an ultrasound field to pump the AO interaction. This pulse contains two tone bursts, one with 3 cycles of 1 MHz sine waves at a lower focal pressure P_{f1} (0.3 MPa), and the other with the same parameters except at a higher pressure P_{f2} (1.5 MPa). These two bursts are separated temporally by 97 μs as shown in Figure 4.5(a). The short separation in time between pulses ensures that the effects of instability and noise from the environment vibrations that are longer than this duration can be effectively reduced in experiment.

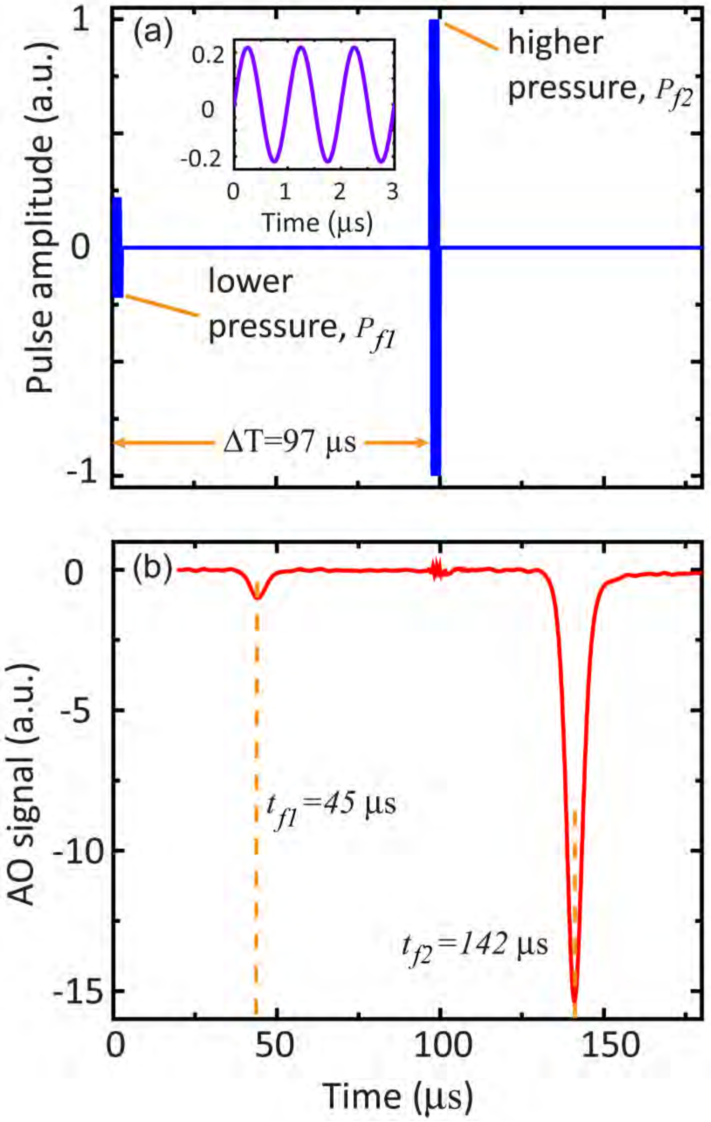

Figure 4.5 (a) The user-defined pulse excited by the function generator and used for driving the ultrasound transducer. The inset shows the zoom-in of the 3-cycle sine waves at 1.0 MHz with the lower amplitude. (b) The resulting AO (averaged) scan line obtained within a homogenous phantom ($\mu_a = 0.14\,cm^{-1}$, $\mu_s^{'} = 7\,cm^{-1}$).

A time-dependent (averaged) AO scan line generated under these conditions within a homogenous phantom ($\mu_a = 0.14\,cm^{-1}$, $\mu_s^{'} = 7\,cm^{-1}$) is shown in Figure 4.5(b), which shares the same time base (X axis) with Figure 4.5(a). As we can see, the first arrival at approximately 45 μs is the AO signal generated by the 0.3 MPa pulse and the latter arrival at 142 μs is generated by the 1.5 MPa pulse. The PCS is then determined by dividing the AO signal amplitude measured at t_{f2} and t_{f1}:

$$PCS = \frac{\left|I_{AOS}(t = t_{f2})\right|}{\left|I_{AOS}(t = t_{f1})\right|}. \tag{4.11}$$

4.3.4. Experiment samples

17 acrylamide gel tissue-mimicking phantoms were used for the study in this chapter. These phantoms were fabricated with a range of optical absorption and scattering properties following the method described in Chapter 2. Table 4.1 lists the optical characteristics of these phantoms with exterior dimensions of $40 \times 25 \times 40\,mm^3$ (along the X, Y, and Z axes, respectively). The phantoms are divided into 5 groups.

Table 4.1 The optical features of phantoms used in this chapter

Group	Quantity	Background medium	Inclusion
I	7	$\mu_s^{'} = 4-10\,cm^{-1}$, $\mu_a = 0.14\,cm^{-1}$	
II	4	$\mu_s^{'} = 4\,cm^{-1}$, $\mu_a = 0.14\,cm^{-1}$	6x6x20 mm^3, $\mu_s^{'} = 4\,cm^{-1}$, $\mu_a = 0.14/1/2/3\,cm^{-1}$
III	4	$\mu_s^{'} = 5\,cm^{-1}$, $\mu_a = 0.14\,cm^{-1}$	6x6x20 mm^3, $\mu_s^{'} = 5\,cm^{-1}$, $\mu_a = 0.14/1/2/3\,cm^{-1}$
IV	1	$\mu_s^{'} = 6\,cm^{-1}$, $\mu_a = 0.14\,cm^{-1}$	6x6x20 mm^3, $\mu_s^{'} = 5/7\,cm^{-1}$, $\mu_a = 0.14\,cm^{-1}$ (2 inclusions)
V	1	$\mu_s^{'} = 7\,cm^{-1}$, $\mu_a = 0.14\,cm^{-1}$	5x6x20 mm^3, $\mu_s^{'} = 10\,cm^{-1}$, $\mu_a = 0.14\,cm^{-1}$

Among them, phantoms in Group I had the identical absorption but different scattering coefficients by changing the concentration of polystyrene microspheres, and these were used for measuring the PCS as a function of optical scattering in homogeneous media. Phantoms in Group II and III were embedded with an optical absorption inclusion at the center as shown in Figure 4.6(a). The inclusions were made of the same material as the background except that extra amount of Indian ink was added during the fabrication to exhibit different absorption coefficients. These phantoms were used for measuring the PCS as a function of absorbing contrast with ultrasound pulses traversing the center of the inclusion, the results of which were compared with those obtained from Group I phantoms. The phantom in Group IV was embedded with two inclusions with different scattering coefficients in contrast with the background (Figure 4.6b) and used for demonstrating the feasibility of using pressure contrast AOI for the detection and quantification of optical inhomogeneities. The last phantom (Group V) had a scattering inclusion at its central position (as Group II/III phantoms) and it was used to demonstrate 2-D quantitative imaging of an optical heterogeneity.

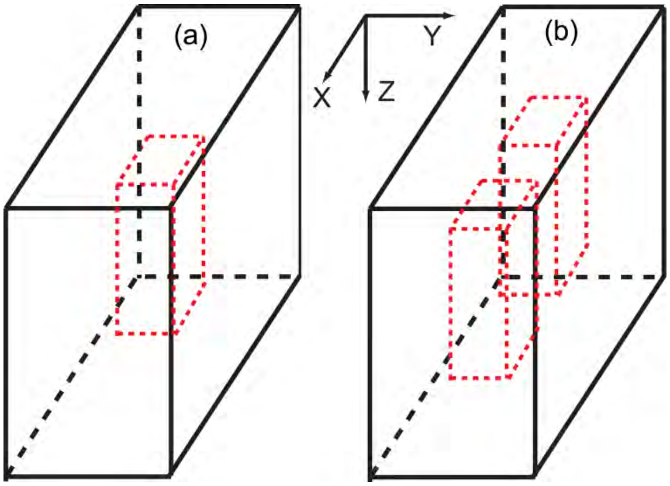

Figure 4.6 Illustration of phantoms embedded with (a) one inclusion at the center and (b) two inclusions positioned at the same Z position in the X-Z plane and separated by 15 mm along the X axis. XYZ is the system coordinate.

During the experiment, the ultrasound pulses were fired from the top of the phantoms and travelled along the Z axis (Figure 4.6). The center of the acoustic focal region was placed in the middle of the phantom (and the inclusion if embedded) along the Z direction. The inclusion lengths along the Z direction were made sufficiently long with respect to the ultrasound pulse axial length (around 5-6 mm) to ensure when the ultrasound pulse traversed the center of the inclusion, that entire ultrasound pulse packet would be inside of the inclusion. This was done to ensure that the detected PCS at the focus is solely determined by the inclusion material, but not affected by the background medium.

4. 4. Experiment results

4.4.1. Correlation between PCS and optical properties

In order to measure the dependence of PCS on optical properties, each of the phantoms in Group I was sonified by the aforementioned user-defined ultrasond pulses at a repetition rate of 4 kHz. The ultrasound transducer was aligned in advance such that the focal region intersected the center of the incident optical beam as well as the center of the phantoms. 10,000 time-domain AO signals were acquired and averaged, yielding a single scan line from which both AO signal amplitudes at the focus corresponding to the two pressure amplitudes were obtained. The PCS was then determined through Eq. (4.11). This process was repeated 80 times to obtain a mean PCS for an improved measurement precision (low standard errors). The same procedures were followed for all the phantoms.

The resulting mean PCSs are illustrated in Figure 4.7 (squares) as a function of the transport coefficient of each individual homogeneous phantom, where the error bars depict the stand error from the 80 times of repetition. As we can see, the PCS increases monotonically from approximate 14.4 to 16.1 when $\mu_t^{'}$ (sum of optical absorption and scattering coefficients) is increased from 4.14 cm^{-1} to 10.14 cm^{-1}.

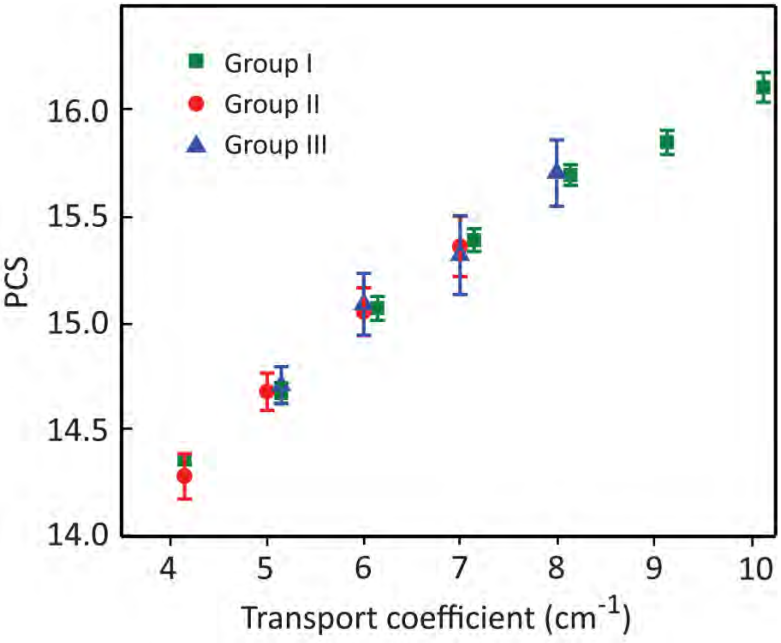

Figure 4.7 PCS as a function of transport coefficient in homogeneous media (Group I) or in embedded inclusions (Group II and III).

Same measurements of PCS were also performed in group II and III phantoms, where the ultrasound pulses traversed through the center of the embedded absorption inclusions in a way outlined in Section 4.3.4. As shown in Figure 4.7, the obtained PCSs are consistent in general with those in homogeneous (Group I) phantoms. This finding shows the correlation between PCS and optical properties is not affected by the media surrounding the AO interaction volume.

4.4.2. Dependence of PCS on ultrasound field focus position with respect to the light illumination

From Group I, two phantoms were selected, one with $\mu_s^{'} = 5\,cm^{-1}$ and the other with $\mu_s^{'} = 7\,cm^{-1}$.The transducer was positioned such that the focus of the ultrasound pulse met with the signal beam center, and this position was denoted as $(X = 0, Z = 0)$. Then, the transducer was scanned from -5 mm to 5 mm along the X and Z directions, respectively, while the phantoms and optical beam were kept stationary (Figure 4.8). At each position, the PCS was measured with previously described procedures, except that the measurements were repeated 40 times instead of 80 to obtain a mean PCS.

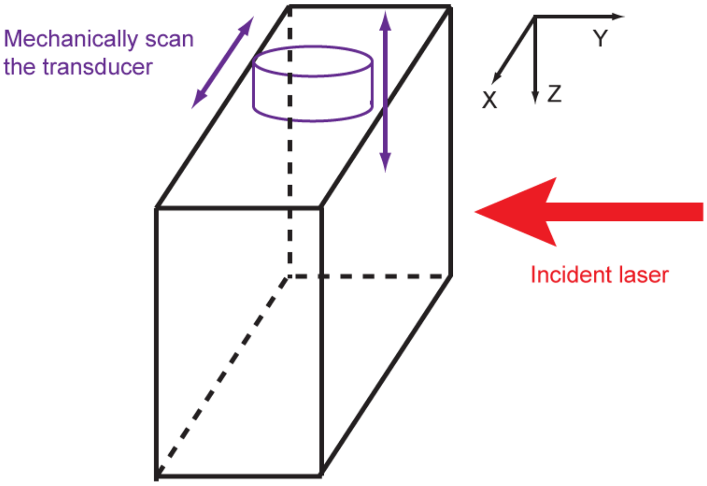

Figure 4.8 The schematic configuration of mechanically scanning the ultrasound transducer along the X and Z directions respectively.

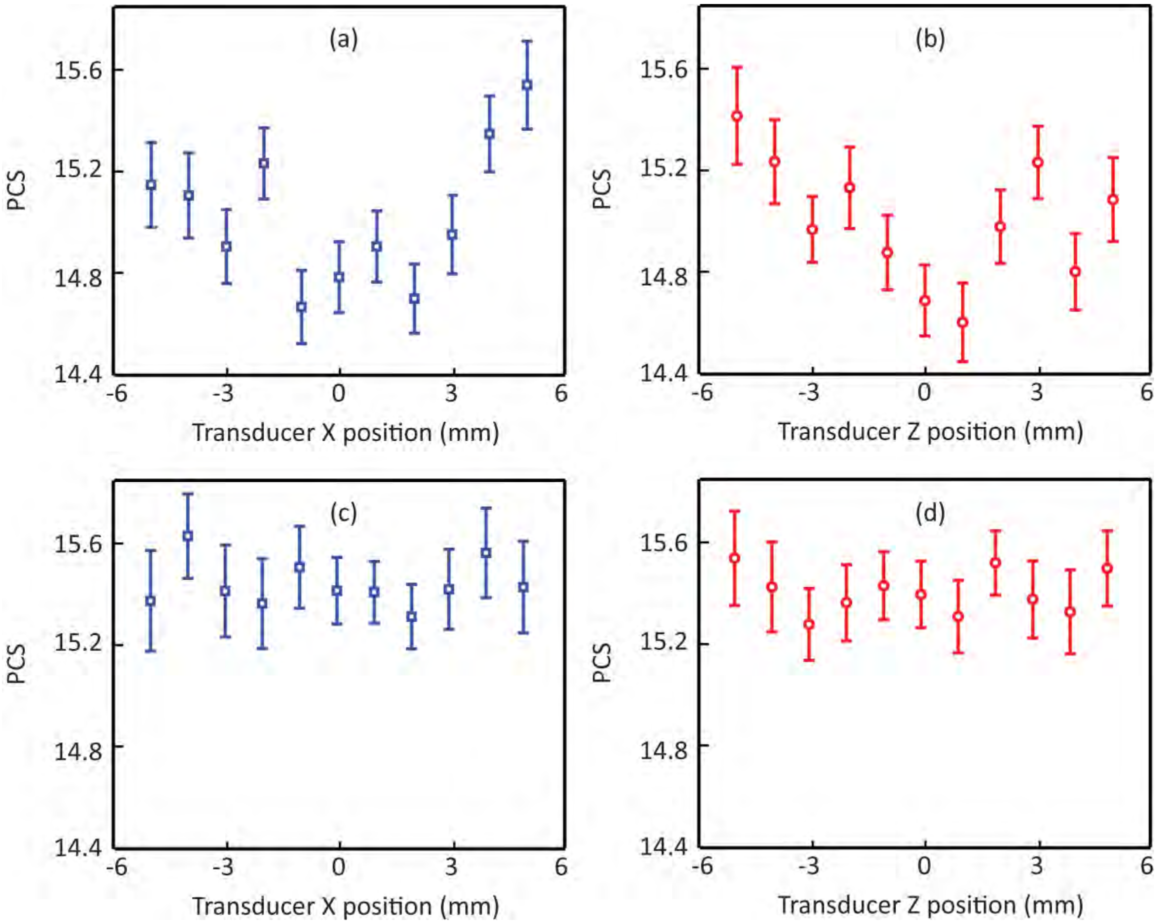

Figure 4.9 PCS dependence on ultrasound transducer position for (a) $\mu_s^{'} = 5\,cm^{-1}$ along the X direction, (b) $\mu_s^{'} = 5\,cm^{-1}$ along the Z direction, (c) $\mu_s^{'} = 7\,cm^{-1}$ along the X direction, and (d) $\mu_s^{'} = 7\,cm^{-1}$ along the Z direction.

The scanning results are shown in Figure 4.9. As we can see the values of PCS at the central positions are approximately consistent with those in Figure 4.7, which have the same transport coefficients. In the less diffuse ($\mu_s^{'} = 5\,cm^{-1}$) phantom, the value of PCS, however, increases when the ultrasound beam focus is off the light illuminating center. In comparison, within the phantom with a higher diffusivity ($\mu_s' = 7\,cm^{-1}$), the measured PCSs are relatively uniform, showing less dependence on the exact position of the ultrasound beam focus.

4.4.3. Application of pressure contrast AOI for the detection and quantification of optical heterogeneities

We have shown in the previous sections that the PCS is directly related with the μ_t' of the local medium, which is consistent in either homogeneous or inhomogeneous highly diffuse media. In this section, the pressure contrast approach was used to detect and characterize the optical properties of inhomogeneities embedded in another diffuse medium.

The phantom in Group IV (Table 4.1), embedded with two optical scattering inclusions as illustrated in Figure 4.6 (b), was used in this experiment. The user-defined ultrasound pulses were generated over the phantom and propagated downwards along the Z direction. The focus of the ultrasound field was positioned around the middle of the phantom as described earlier. During the experiment, the phantom was scanned from -15 mm to 15 mm in 1 mm steps along the X direction (transducer and optical beam were stationary). At each position, the PCS was obtained with the aforementioned procedures outlined for the measurements for Figure 4.7.

The scanning result is in shown in Figure 4.10, where the PCS is plotted as a function of phantom position. The two inclusions are clearly evident in the figure, with one centered about $X = -7.5\,mm$ and the other around $X = 7.5\,mm$. The dimension of these two inclusions and the spacing between them in the X direction seen from the figure agree quite well with the actual values. Moreover, as we can see the mean PCS at the centers of the inclusions are approximately 14.66 and 15.39, respectively. Outside of the inclusions, pressure ratio values around 15.0 are observed. Returning to the PCS values calibrated in Figure 4.7, these values of PCS are nearly identical to those measured for transport coefficients of 5, 7 and 6 cm^{-1}, respectively. It once again confirms that the PCS is not influenced by the fact the inclusions are embedded in another medium possessing scattering contrast, indicating that the pressure contrast AO response potentially can be used for the local and quantitative measurement of transport coefficients.

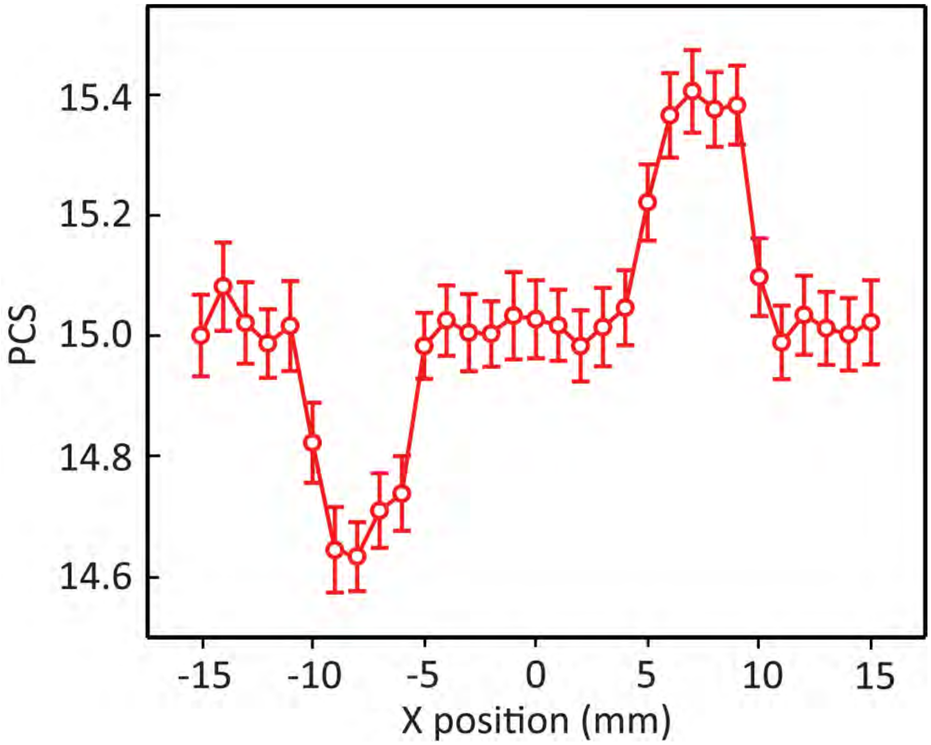

Figure 4.10 PCS as a function of phantom position along the X direction revealing the presence and diffusivity of the embedded optical inhomogeneities.

To further demonstrate the feasibility of pressure contrast AOI for the quantitative optical measurement of embedded optical inhomogeneity, the PCS measurements were performed within the phantom in Group V (Table 4.1) that was embedded with a scattering inclusion ($\mu_s^{'} = 10$ cm^{-1}) in the middle. As in previous experiments, the transducer focal zone was positioned at the center of the phantom (and the inclusion) in the Z direction. During the measurement, the transducer was scanned in the XY plane with a step size of 0.5 mm along both directions. At each position, the PCS was measured with experiment settings identical to those outlined previously except the total number of repetitions to obtain a mean PCS at each position was reduced by a factor of ten.

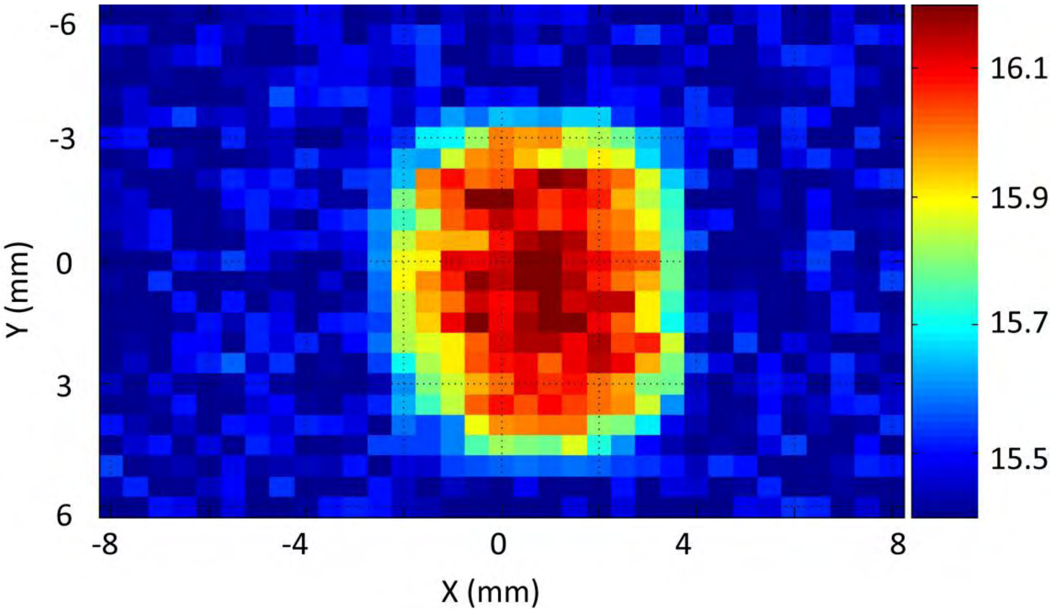

Figure 4.11 An XY-plane pressure contrast AO image of an optically scattering inclusion ($\mu_a = 0.14\,cm^{-1}$, $\mu_s^{'} = 10\,cm^{-1}$) embedded in a highly diffuse phantom ($\mu_a = 0.14\,cm^{-1}$, $\mu_s^{'} = 7\,cm^{-1}$). The color bar corresponds to the measured value of mean PCS.

Figure 4.11 shows the XY-plane pressure contrast AO image of the embedded inclusion. Each pixel in the image represents one measuring position, and the value of measured mean PCS is indicated by the color bar. With this image, one can readily tell the existence, location and dimensions of the inclusion. Furthermore, the mean PCS values at the center of the inclusion and the background are around 16.1 and 15.1, respectively. Again, referring back to the calibration (Figure 4.7), these values correspond to $\mu_t^{'}$ of 10 and 7 cm^{-} that were measured in homogeneous media. This finding, as well as that from Figure 4.10, shows that an inclusion gives a similar pressure contrast response as a homogeneous medium as long as they have the same transport coefficient, irrespective of the drastic difference in direct AOS strengths.

4. 5. Discussion

The objective of this chapter was to develop an approach to measure the optical properties of scattering media quantitatively based on the general AO response. In Section 4.2, it was shown theoretically that the ratio of two AO signal amplitudes under different ultrasound focal pressures depended solely on the local optical transport coefficients within the AO interaction volume with given ultrasound pulse shape and pressure pair.

Through experiments it was found that the measured PCS increased approximately linearly with the transport coefficient in homogeneous media. In Eq. (4.7), this PCS is related with the coefficient β. Using the measured PCS data shown in Figure 4.7 and the and known P_{f1} and P_{f2}, the coefficient β can be found. A plot of β as a function of medium optical transport coefficient is given in Figure 4.12(a). According to Eq. (4.5), the value of $1-J_0(\beta P_f)$ provides a measure of the modulated signal strength. In Figure 4.12(b), $1-J_0(\beta P_f)$ is plot as a function of $\mu_t^{'}$ with a focal pressure of 1 MPa.

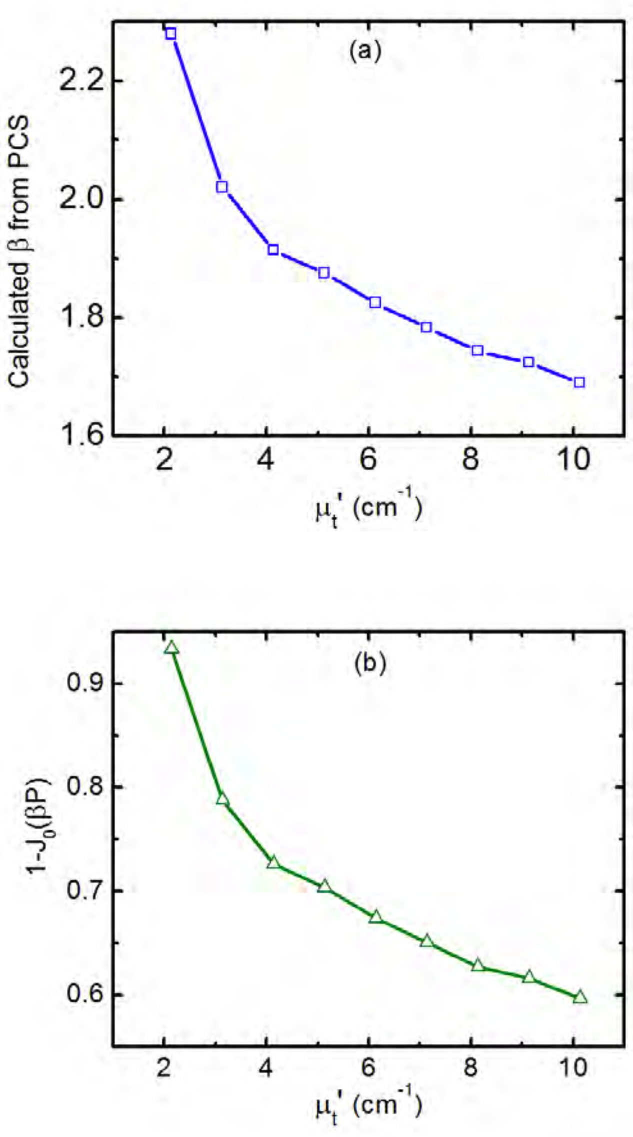

Figure 4.12 (a) Calculated β from the measured PCS and (b) $1-J_0(\beta P_f)$ as a function of medium optical transport coefficient.

As we can see from Figure 4.12, in response to increased PCS, the values of β and $1-J_0(\beta P)$ are reduced with increased medium optical absorption and/or scattering, which can be interpreted as a decrease in the mean phase shift imparted on the diffuse light due to the ultrasound modulation as the $\mu_t^{'}$ is increased. This finding is consistent with Figure 4.13 that is derived from Figure 2.8(b), highlighting that the net signal modulation from the ultrasound ($C_{s,U}$, which was described in Chapter 2) decreases with increased $\mu_t^{'}$. Similar experimental observations were also reported (Kim and Wang 2007; Kothapalli *et al.* 2007; Kothapalli and Wang 2008).

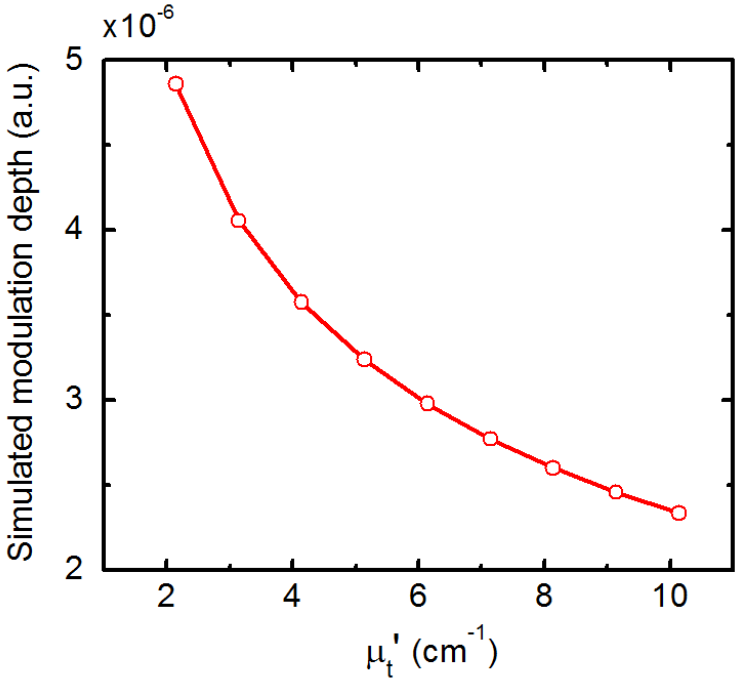

Figure 4.13 Simulated modulation depth as a function of optical transport coefficient based on the mechanisms of AO interaction discussed in Chapter 2.

Figure 4.7 also shows that detections in embedded inclusions afford similar PCS values as those obtained in homogenous media, and the value of PCS is consistent for scattering or absorbing contrast. These, along with the observed independence of PCS on ultrasound transducer position relative to the light illumination in highly diffuse media (Figure 4.9), suggest that the PCS is not dependent on the characteristics of the optical path that the light follows or the amount of light collected, but rather is dictated by the optical properties within the region where light and sound interact under the assumption that any spatial variations in the light distribution within the media are large with respect to the ultrasound pulse (i.e., the ultrasound pulse should be uniformly illuminated). This indicates that the PCS can be potentially used as a relatively simple means for the quantitative measurement of optical properties for embedded optical inhomogeneities, the feasibility of which was demonstrated experimentally (Figures 4.10 and 4.11). Therefore, pressure contrast AOI opens up the possibility of quantitative measurement of optical properties of inhomogeneities buried in turbid media with no *a priori* knowledge of the optical features of the background media.

Lastly, it should be pointed out that the detection contrast in PCS is quite small. The SNR in the measurement system ultimately limits the ability to distinguish two media with similar optical properties. In the experimental results shown here, a substantial number of averages were taken. Figure 4.14 shows a series of PCS scanning of Group IV phantom that have been repeated over differing times (denoted as N_{rep}). In Figure 4.14(a), five measurements were repeated to obtain a mean value of PCS at each position. It is apparent that the *SNR* of the PCS detection[2] in this case is too poor to reveal the location or dimensions of the embedded targets. Needless to say, quantitative measures of the optical properties are impossible in this case. However, as N_{rep} is increased, the error bar of the PCS measurements decreases approximately by a factor of $1/\sqrt{N_{rep}}$, as expected for coherent averaging of uncorrelated measurements. With $N_{rep} = 40$ and 80, as illustrated in Figure 4.14(e) and (f), the embedded scattering inclusions can be clearly identified in terms of location, dimension and quantitative $\mu_t^{'}$ with Figure 4.7 as reference.

---

[2] The *SNR* of the PCS detection is defined here as the ratio between the signal amplitude (PCS value differences between diffusivity of 6 cm^{-1} and 5/7 cm^{-1} from Figure 4.7) and the rms value of the error bars.

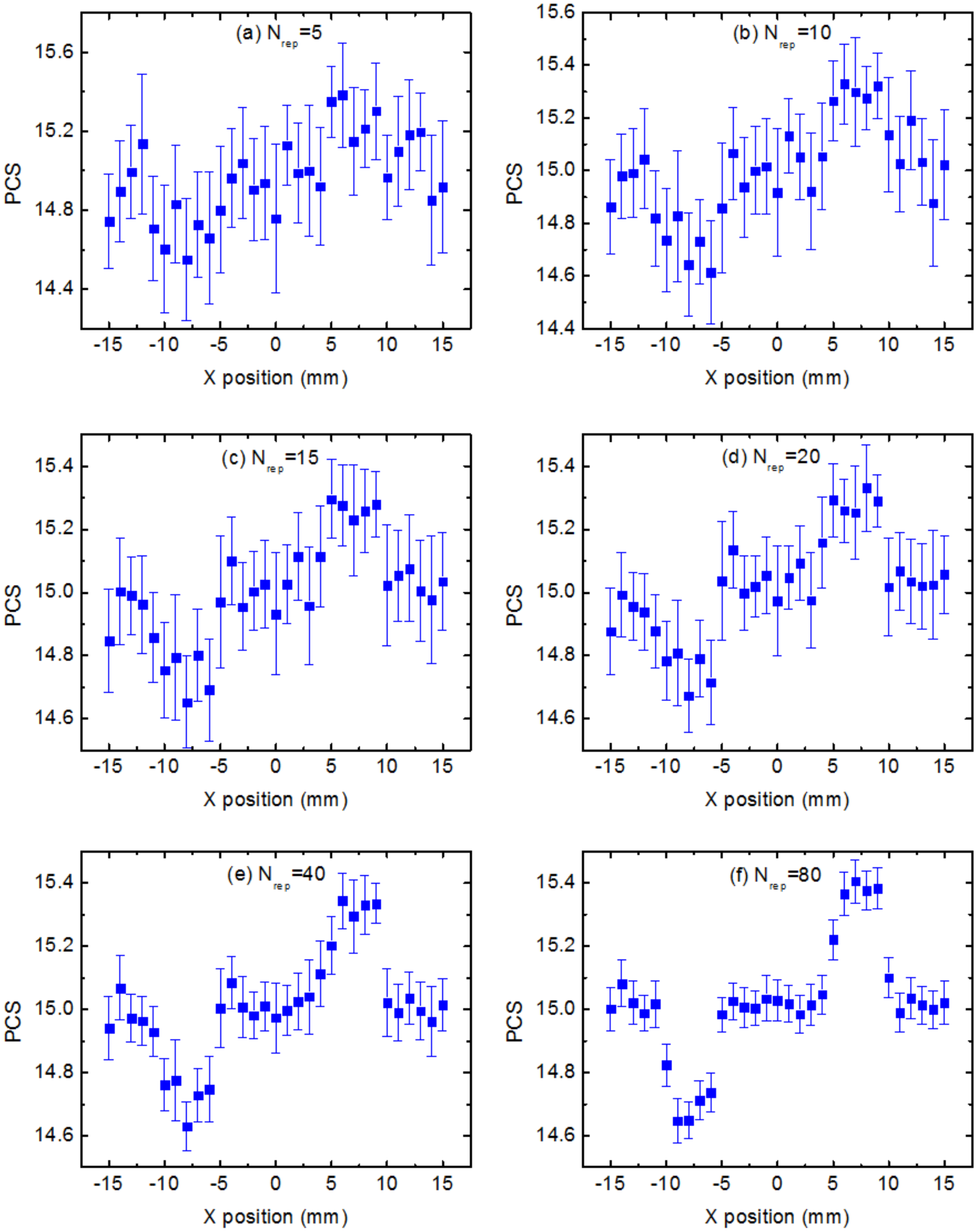

Figure 4.14 PCS detection of two embedded inhomogeneities in Group IV phantom with the same procedure but different numbers of repetition on PCS computation. The error bars represent the levels of standard error.

4. 6. Summary

This chapter describes an extension of AOI for the local and quantitative measurement of optical properties within diffuse media. The GaAs crystal based AOI system built in Chapter 3 is used to detect direct AO signals generated at ultrasound focal pressures of 0.3 and 1.5 MPa when an ultrasound pulse traverses its focus. The ratio of the magnitudes of the two AO signal strengths, denoted as PCS in the study, is shown to be solely dependent on the mean phase shift imparted on the light by the ultrasound in highly diffuse media, which is closely related to the local optical properties within the AO interaction region. It is shown experimentally that the PCS increases with the *optical transport coefficient* (sum of absorption and scattering coefficients) of the medium, and this increase is related to a decrease in the modulation depth induced by the ultrasound as optical absorption and/or scattering is increased. This agrees qualitatively with the theoretical simulations and other experimental observations reported in literature. It is also demonstrated that it is feasible to use the proposed pressure contrast AOI to both image and quantify the optical properties of the inhomogeneities buried in turbid media without *a priori* knowledge of the background media in which the heterogeneities are embedded.

Chapter 5

Monitoring High Intensity Focused Ultrasound (HIFU) Treatment in Real Time Using Acousto-Optic Sensing

5. 0. Overview

In this Chapter, we propose to use AO sensing to monitor the real-time changes in the optical properties of tissue associated with the formation of thermally necrosed tissue regions under the high intensity focused ultrasound (HIFU) exposure. In Section 5.1, a general introduction of HIFU and HIFU treatment monitoring is given, showing that real-time treatment monitoring poses a significant challenge. The concept of using the AO response to monitor the lesion formation is presented in Section 5.2. In Section 5.3, the methods and materials used in the study are detailed. In Sections 5.4 and 5.5, experimental results obtained using *ex vivo* chicken breast demonstrate the feasibility of using AO sensing to identify the onset and growth of lesion formation in real time, and to guide the HIFU exposure for more predictable lesion formation. A brief summary of this Chapter is given in Section 5.6.

5. 1. Introduction

5.1.1. High intensity focused ultrasound

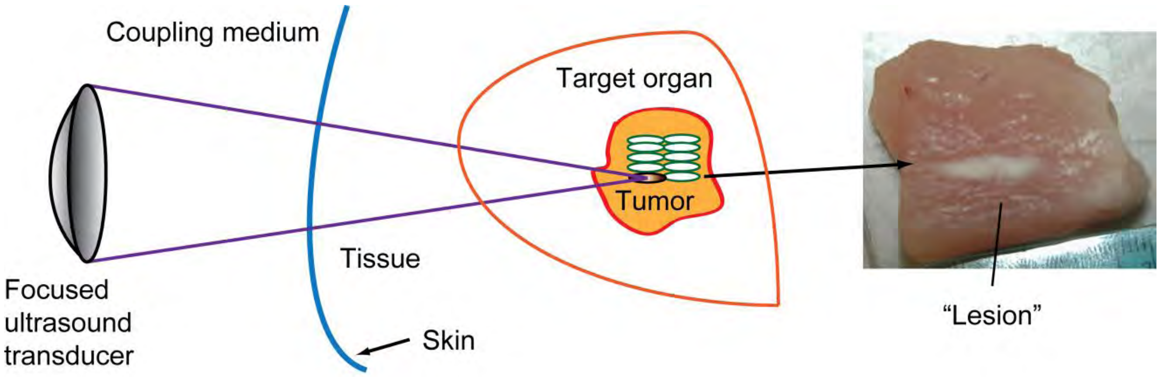

Figure 5.1 A schematic diagram showing the basic principle of HIFU treatment of a tumor in a target organ. By scanning the focal position of the HIFU field, a series of adjacent "lesions" can be created as shown to obtain the ablation of the whole tumor volume. Cross-section of a formed necrosed region (lesion) in exercised chicken breast is shown on the right.

High intensity focused ultrasound (HIFU) is a promising non-invasive technique that is used for the thermal damage of soft tissue tumors, while minimizing damage to outlying regions (ter Haar 1995). Figure 5.1 shows a schematic diagram of the basic principles of HIFU treatment of a solid tumor in a target organ. In HIFU therapy, a continuous wave (CW) or pulsed modulated CW ultrasound field, usually with a center frequency between 1 and 5 MHz, is generated by a focused transducer, penetrates through a coupling medium (usually water or gel), skin and soft tissue, and is focused to a relatively small volume (order of 0.01 cm^3) with intense *in situ* acoustic power density (order of kW/cm^3) (Watkin *et al.* 1996). Sound absorption by tissue results in a temperature elevation locally within the focal region. If the temperature, for example, is raised above 55-56 °C for more than 1 s (Dewhirst *et al.* 2003; Hill *et al.* 2004), this heating causes irreversible tissue necrosis, where the volume of the destroyed tissue is commonly referred to as a "lesion". Since the heating is spatially confined within the ultrasound focal region, the volume of one lesion formed from a single HIFU exposure is usually ellipsoidal and order 1-2 mm in diameter and 1 cm in length; the specific dimensions depend on the acoustic frequency and the dimension of the HIFU source. Therefore, to ablate a whole region of tumourous tissue, as shown in Figure 5.1 the ultrasound focus needs to be scanned over the required volume to generate a series of adjunct lesions in 2- or 3-D.

HIFU was first proposed by Lynn *et al.* (1942) 68 years ago, and presently HIFU has been investigated for many applications, such as haemeostasis (Vaezy *et al.* 1998), thrombolysis (Rosenschein *et al.* 2000), drug/gene delivery (Porter and Xie 2001; Ng and Liu 2002) and the clinical treatment of tumors in liver (ter Haar *et al.* 1989; Kennedy *et al.* 2004), kidney (Kohrman *et al.* 2002; Wu *et al.* 2003b), prostate (Gelet *et al.* 2000; Thuroff *et al.* 2003), uterus (Chan *et al.* 2002; Stewart *et al.* 2003), breast (Gianfelice *et al.* 2003a; Wu *et al.* 2003a), and pancreas (Wu *et al.* 2005; Xie *et al.* 2008).

5.1.2. Clinical monitoring of HIFU treatment

The variations in physical properties of the tissue layers (e. g., fat and muscle) in the acoustic path between the transducer and the focal region, however, limit the reliability in estimating the HIFU intensities *in situ* (Maleke and Konofagou 2008) and the resulting heating. This, along with uncertainty in the degree of tissue cooling from blood flow, serves to complicate treatment planning. In order to improve the efficacy and safety of HIFU treatments there is a need for reliable real-time feedback techniques that correspond to the lesioned tissue *in situ*. This would allow for the implementation of precise protocols to provide the optimum treatment of the tumourous region (Rivens *et al.* 2007). A number of non-invasive techniques have been developed to tackle this problem, for example magnetic resonance imaging (MRI) (Cline *et al.* 1993; Gianfelice *et al.* 2003a), diagnostic ultrasound (ter Haar *et al.* 1989; Illing and Chapman 2007), magnetic response elastography (MRE) (Lewa 1991), radiation force elastography (RFE) (Lizzi *et al.* 2003) and vibroacoustography (Konofagou *et al.* 2003). Among these, MRI and diagnostic ultrasound are the only methods that are currently used clinically.

5.1.2.1 Magnetic resonance imaging

Magnetic resonance imaging (MRI) has been used to delineate tissue types and map the temperature change resulting from HIFU exposures with millimeter spatial and 2°C temperature resolution *in vivo* (Tempany *et al.* 2003; Rivens *et al.* 2007). An example of a magnetic resonance image of a lesion is given in Figure 5.2, where one is able to identify the shape, extent and boundary of the lesion evidently. Currently MRI is the “gold” standard for HIFU guidance (Cline *et al.* 1993; Hynynen *et al.* 1996; McDannold *et al.* 1998; Furusawa *et al.* 2006) and has been used clinically in the treatment of breast carcinoma (Gianfelice *et al.* 2003b) and uterine fibroids (Stewart *et al.* 2003). A significant disadvantage of this imaging technique, which is particularly pertinent for temperature imaging, is that each image frame can take up to several seconds to acquire and process (Vaezy *et al.* 2001; Kopelman *et al.* 2006) not allowing for real-time monitoring. Furthermore, the high cost of the apparatus, the lack of portability, and requirement for a magnetically compatible HIFU system further increases the design complexity and cost, ultimately limiting the accessibility of this modality (Kennedy 2005).

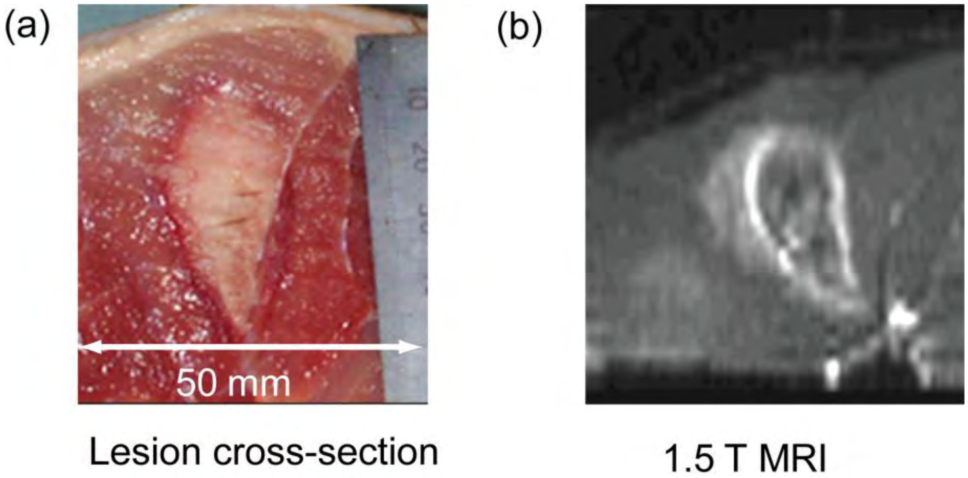

Figure 5.2 An example of magnetic resonance image of a lesion sample (Courtesy of Dr. Ian Rivens, Institute of Cancer Research, UK).

5.1.2.2 Diagnostic ultrasound

In contrast with MRI, diagnostic ultrasound is comparatively inexpensive, portable, and capable of imaging in real time with reasonable spatial resolution. Ultrasound-guided HIFU has been implemented clinically, for both extracorporeal (Wu *et al.* 2004; Wang *et al.* 2009) and transrectal (Uchida *et al.* 2002; Illing and Chapman 2007) treatments.

When using diagnostic imaging in conjunction with HIFU it is necessary to temporally interleave the imaging and therapy beams in order to avoid acoustic interference in the B-mode images (Vaezy *et al.* 2001). However, insufficient acoustic contrast between necrotic and normal tissue results in the inability to reliably visualize lesions on B-mode images (Hill and ter Haar 1995) unless the exposure possesses the intensity and duration needed to generate actual boiling within the lesion, leading to a “hyperechoic” response in the HIFU focal region (Vaezy *et al.* 2001; Rabkin *et al.* 2005; Rabkin *et al.* 2006; Coussios *et al.* 2007) as shown in Figure 5.3b. Studies (Meaney *et al.* 1998; Meaney *et al.* 2000; Bailey *et al.* 2001; Khokhlova *et al.* 2009) show that cavitation and/or boiling may distort the lesion location, shape and size. On the other hand, the formation of cavitation and/or boiling is hard to predict and control, and the occurrence of boiling may imply an overtreatment for a particular region. More importantly, bubbles and lesion don’t necessarily coincide. These complicating factors highlights the fact that boiling may want to be avoided during treatments, even though this will result in no feedback mechanism from exposures.

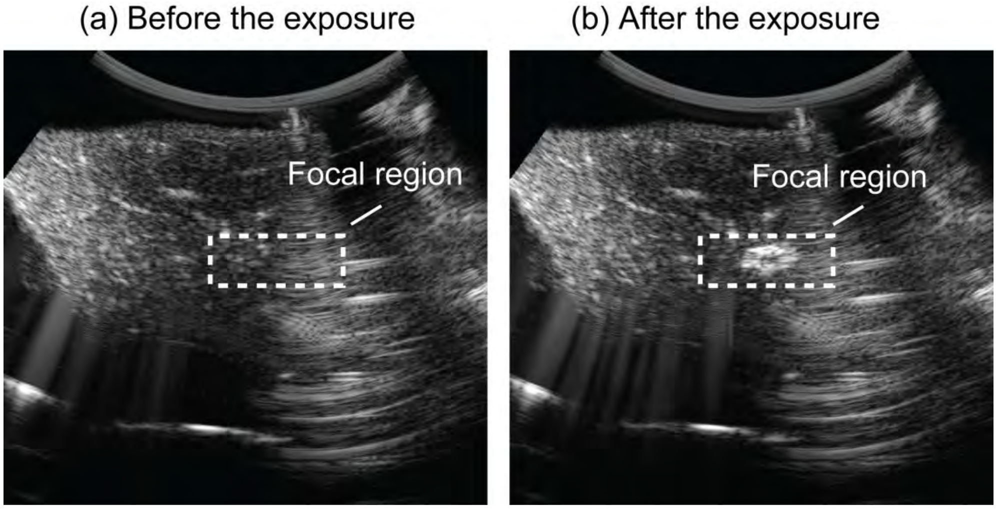

Figure 5.3 B-mode ultrasound images (a) before and (b) right after a 10 MPa (free field, peak-positive pressure) and 34 s HIFU exposure within an exercised chicken breast.

5. 2. Acousto-optic sensing

As we can see real-time monitoring of lesion formation still poses challenges thus far, especially at lower ultrasound pressure levels where boiling effect does not result. Therefore, there is a need for new approaches that are able to provide accurate feedback associated with the formation and development of HIFU lesions.

The sensing contrasts of the modalities discussed above are based on the dynamic changes in either proton resonant frequency shift or mechanical/acoustic properties accompanying the thermal necrosis of tissue. In soft tissue, such as liver and breast, thermal necrosis induces an increase in the optical absorption coefficient (μ_a) and the reduced scattering coefficient ($\mu_s^{'}$) of the lesioned volume. In the visible and near-infrared (NIR) optical wavelength range, optical absorption in tissue is predominantly dictated by the relative concentrations of water, lipids, oxy-haemoglobin (HbO_2) and deoxy-haemoglobin (Hb) (Quaresima *et al.* 1998), and scattering is affected by the tissue structural inhomogeneities and the variations in index of refraction. A study from Nilsson *et al* (1998) demonstrated a 100-300% increase in optical absorption and 120-280% increase in reduced scattering coefficient (for 600-1500 nm) in necrotic and normal rat liver *in vivo*. Similar trends were reported for *ex-vivo* porcine liver (Khokhlova *et al.* 2006) and chicken breast (Ben-David *et al.* 2008) at wavelengths of 1064 and 1041 nm, respectively. Three major mechanisms have been proposed for the observed increase in optical absorption and scattering. First, the coagulation increases the concentration of chromophores (Cilesiz and Welch 1993; Yaroslavsky *et al.* 2002). Next, the formation of mathaemoglobin from haemoglobin during blood coagulation has been shown (Black and Barton 2004) to cause a five-fold increase in the absorption at 1064 nm. Finally, the decrease in the average effective size of the scatterers further increases the number of scattering sites and consequentially the scattering (Nilsson *et al.* 1998).

Optical sensing, therefore, presents a potential modality for monitoring lesion formation in tissues such as breast, brain, and prostate, where optical access is facilitated by characteristically low absorption, particularly when compared with highly vascularized tissues such as kidney and liver. However, as mentioned earlier (Chapter 1 and 2), light is highly scattered in most of biological tissues, resulting in a diffusive optical field that limits spatial resolution to approximately 5 mm (at best) for penetration depth of order centimeters (Boas *et al.* 2001).

In this chapter, AO sensing is proposed as a technique to monitor, in real time, the formation of *non-cavitating* lesions from HIFU exposures in excised chicken breast. The formation of a lesion results in a measurable increase in the optical absorption and reduced scattering coefficients, which in turn would induce a reduction in the amplitude of the AO signal amplitude (Sakadzic and Wang 2005; Lai *et al.* 2009a). The sensing technique is based on the AOI system described in Chapter 3 and modified to allow for real-time monitoring of a fixed volume using a lock-in amplifier to enhance the SNR. Since the same HIFU beam is used to simultaneously form the lesion and pump the AO response, registration between the sensing and therapy modalities is automatic and the system is used to both monitor the onset of lesion formation and estimate the resulting lesion volume in real time.

5. 3. Materials and methods

Fig. 5.4 shows a schematic of the experimental apparatus used for this study. It is comprised of four sub-systems: a HIFU system to provide both the local heating and ultrasound modulation; a GaAs photorefractive crystal-based AOI system described in Chapter 3 to detect the local optical properties of the tissue; an active cavitation detection (ACD) system using a conventional ultrasound imaging system to determine whether or not boiling is generated during the exposure; and finally, a passive cavitation detection (PCD) system using a single element transducer to monitor the broadband emissions from the potential inertial cavitation. Figure 5.5 is a photograph showing the arrangement of

HIFU/PCD transducers, diagnostic ultrasound probe, and incident light beam with respect to the experiment sample.

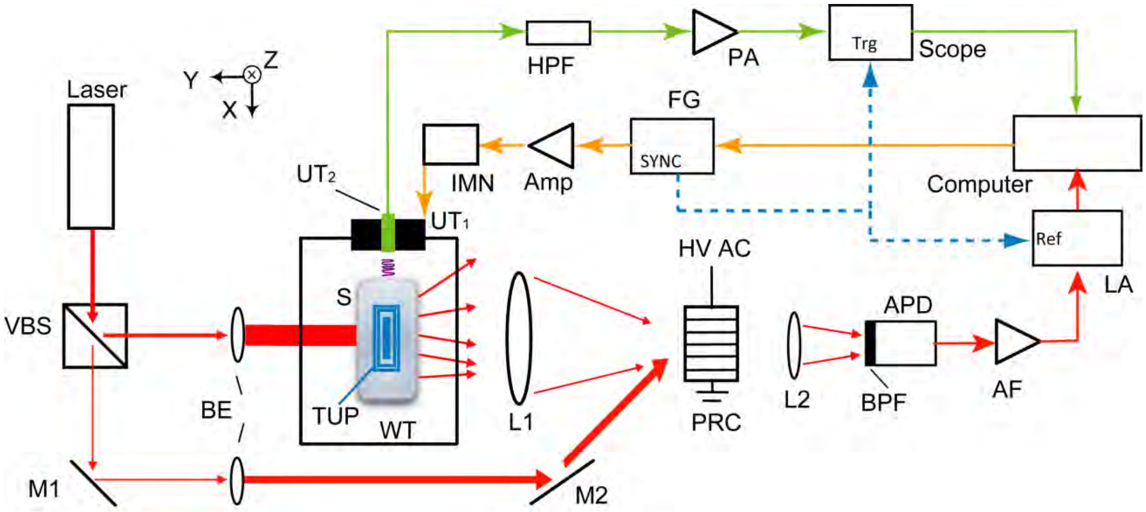
HPF
PA
Trg
Scope
Laser
Y
Z
X
FG
SYNC
Amp
IMN
UT2
UT1
Computer
Ref
LA
HV AC
APD
VBS
S
BE
TUP
WT
L1
PRC
L2
BPF
AF
M1
M2

Figure 5.4 A schematic of the experimental setup used in this study. XYZ- optical system coordinate (with Z as the vertical axis); VBS- variable beam splitter; BE_1, BE_2- beam expander; M_1, M_2- mirror; TUP- Terason ultrasound probe (acoustic axis along the Z axis); WT- tank filled with degassed water; S- degassed chicken breast sample; UT_1- HIFU transducer; UT_2- ultrasound transducer for passive-cavitation detection (PCD); L_1, L_2- lens; HV AC- high voltage AC electrical field; PRC- photorefractive crystal; BPF- band-pass filter; APD- avalanche photodiode; AF- active filter; LA- lock-in amplifier; FG- function generator; Amp- power amplifier; IMN- impedance matching network; PA- preamplifier; HPF- high-pass filter; Scope- Oscilloscope; SYNC- synchronizing output; Trg- trigger signal; Ref- reference signal.

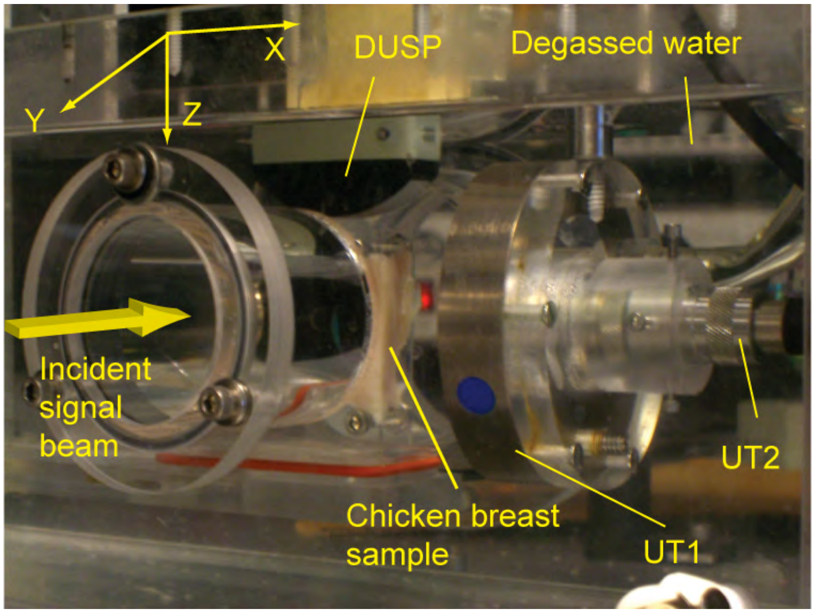

Figure 5.5 A photograph showing the arrangements of HIFU transducer, PCD transducer, diagnostic ultrasound probe, incident light beam and experiment chicken breast sample.

5.3.1. Ex-vivo tissue sample preparation

Ex-vivo chicken breast was used as experiment sample for this study. Chicken breasts were purchased 24 hours prior to the experiment from a local grocery store (Shaw's Allston, Boston, MA, USA). The tissue samples were cut from the chicken breasts to a size of 50x50 mm along both the X and Z axes and 15-30 mm along the Y axis (Fig. 5.6 a-b). The cut tissue samples were degassed in 1% phosphate buffered saline solution (PBS, BP665-1, FisherBiotech, NJ, USA) for 3 hours (Aspirator Pump, Model 7049-00, Cole-Parmer Instrument Company, Ill, USA). Then the sample was mounted in an acrylic holder that was designed to hold the tissue sample through gentle compression with two plates in the Y direction (Figure 5.6c-d). The sample and the holder were then submerged in a large tank (400x180x160 mm^3) filled with freshly degassed (for 1 hour) water as shown in Figure 5.5. The tissue holder was attached to a three-dimension automated translation stage (VXM, Velmex, NY, USA) that allowed the sample to be positioned accurately with respect to the HIFU focus.

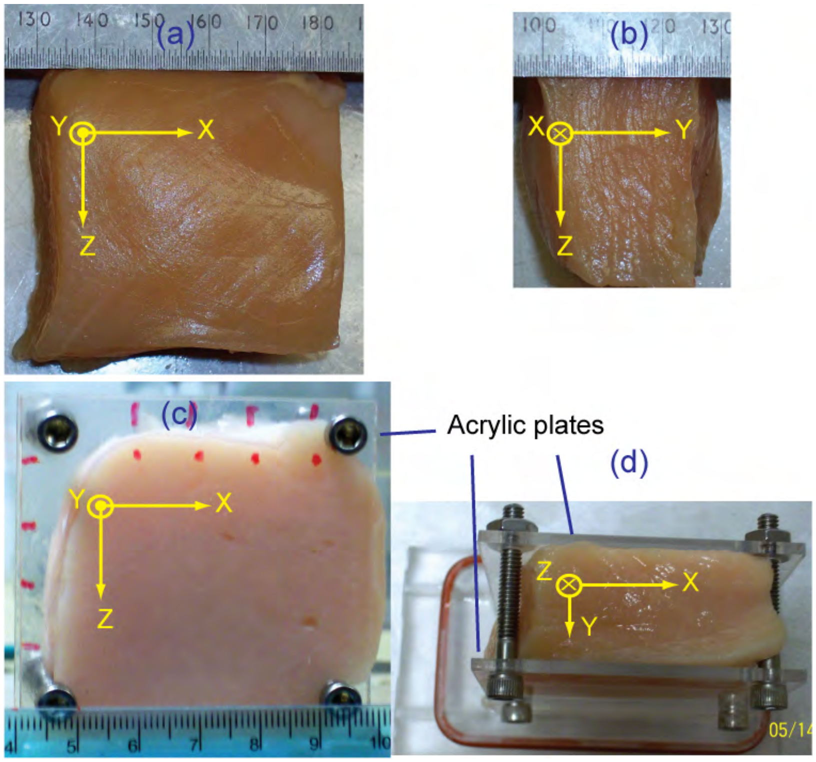

Figure 5.6 Preparation of chicken breast sample. (a), (b): cut tissue sample in the XZ and YZ planes, respectively; (c), (d): degassed tissue sample mounted in the holder.

In this study, 2 or 3 lesions were produced in each sample, with a minimum separation of 10 mm along the Z axis between neighboring lesions. The focal peak of the HIFU was approximately 16 mm into the tissue along the X axis. To ensure that subsequent lesions are generated from the same initial conditions, a minimum of 3 min wait time was used between exposures to allow for tissue cooling. In addition, a thermometer was used to monitor the water temperature at two hourly intervals for each experiment, giving a mean value of 21 ±2°C.

5.3.2. HIFU exposure sub-system

In typical AOI systems, the AO interaction was driven by continuous wave ultrasound (Wang *et al.* 1995), millisecond- duration ultrasound bursts with low duty cycle (Kim *et al.* 2006) or short ultrasound pulses (Murray *et al.* 2004). In the present study, the AO response was driven by a HIFU field, a 1.1 MHz sine wave that was 100% amplitude modulated using a 50 Hz square wave, yielding a pulse train possessing a 50 % duty cycle (Figure 5.7), which serves to generate *both* the AO response and the local heating in tissue during the exposure *at the same time*.

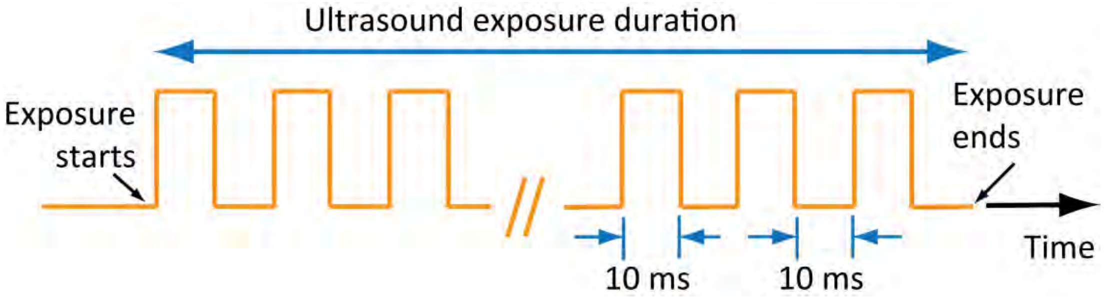

Figure 5.7 The amplitude modulated sinusoidal waves with central frequency of 1.1 MHz during the HIFU exposure. The modulation frequency is 50 Hz and the duty cycle is 50%.

The modulated signals were excited from a function generator (33120A, Agilent, CA, USA), programmed by a personal computer (Dimension 4600, Dell, TX, USA) as shown in Figure 5.4. This function generator also provides a 50 Hz reference signal to the lock-in amplifier, and a trigger signal for data acquisition on the oscilloscope, which will be further mentioned in the following sections. The output of the function generator was attenuated by 20 dB before being sent to a power amplifier (55dB, A150, ENI, NY, USA), whose output was connected to an impedance matching network. The output of the impedance matching network was monitored with a high-impedance voltage probe, which was connected to an oscilloscope (LC334A, LeCroy, NY, USA) and served as an indicator of HIFU pressure amplitude. In a separate measurement performed in degassed water, the driving voltage into the HIFU transducer was mapped to acoustic pressure at the focus using a calibrated fiber optic fiber hydrophone (100 μm fiber diameter, FOPH500, RP Acoustics, Leutenback, Germany).

A 70 mm-aperture, spherically focused single-element piezoelectric transducer (H102, Sonic Concepts, WA, USA) with a 20 mm-diameter central hole was used as the HIFU source (UT_1 in Figure 5.4) in this study. The acoustic beam profile was measured under a peak positive pressure of 9.5 MPa in water using the fiber optic hydrophone. The 6 dB full width half maximum (FWHM) of the focal region was measured to be $10.5x1.6x1.6\ mm^3$. The acoustic axis of the HIFU transducer was aligned perpendicular to the incident light beam such that the focal point intersected with the center of the incident laser beam.

Table 5.1 HIFU Exposure Parameters

	Duration (s)	[*] **Peak pressure (MPa)**	[†] **Peak intensity (W/cm^2)**	**Number of exposures**
Group 1	40	8	2100	72
Group 2	5-60	6-10	1200-3300	87
Group 3	‡	10	3300	157
Group 4	25-75	10	3300	189

[*] Free field peak positive pressure, calibrated in water.

[†] Approximated free-field spatial-peak temporal-peak intensity from equation $I = P_0^2 / (2\rho\upsilon_a)$, where P_0 is the peak positive pressure in water; ρ is the mass density of water, 1000 kg/m^3; and υ_a is the sound speed in water, 1500 m/s.

[‡] Determined by changes in the AO response during the exposure.

Table 5.1 details the exposure parameters used in this study. The acoustic intensities were chosen in order to necrose tissue while avoiding the generation of inertial cavitation and/or boiling. Two study groups were used to explore how AO response change is related to lesion formation under the same (Group 1) or different (Group 2) exposure parameters. The exposures in a third category (Group 3) were used to investigate the feasibility of using the AO response to dynamically guide the exposure duration in order to obtain more consistent and repeatable lesion volumes compared with exposures of a fixed duration (Group 4). The pressure amplitudes shown in Table 5.1 refer to free field peak-positive pressures measured in water, and the corresponding spatial-peak temporal-peak acoustic intensities were approximated from these pressure measurements.

5.3.3. AO sensing sub-system

The PRC-based AOI system described in Chapter 3 is used in this study. An important distinction in the present case, however, is that the output from the photodetector was preamplified (20 dB) and low-pass filtered (at 500 kHz) by an Active Filter (Model 3940, Krohn-Hite, MA, USA), and then fed directly into a lock-in amplifier (LA) (SR830, Stanford Research System, CA). The 50 Hz HIFU modulation signal served as the reference signal for the LA. This resulted in the real-time output from the LA being proportional to the RMS value of the DC offset signal. The LA output was recorded on a personal computer and served as a measure of the AO interaction strength averaged over the 30 ms integration time of the LA.

An example of an averaged AO signal waveform obtained under a relatively low focal pressure (1 MPa peak positive) in *ex-vivo* tissue is illustrated in Figure 5.8. Acquisition of this signal took approximately 20 s (1,000 averages) in order to reach the required SNR level. The APD output possessed a maximum of V_0 in the absence of the HIFU field. At time t_0 the HIFU field was present in the interaction region, resulting in tagged photons and a corresponding voltage offset, V_{pp}. Subsequently, when the HIFU field was off at time $t_0 + 10$ ms, the APD output gradually returned to V_0 at a rate that was governed by the response time of the PRC crystal. This trend was repeated for each modulation cycle of HIFU field.

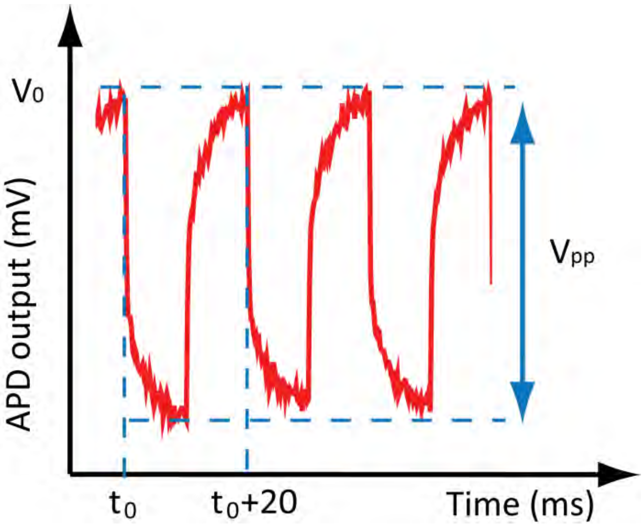

Figure 5.8 An example of time domain AO signal monitored at the APD output under a relatively low ultrasound focal pressure (1 MPa peak positive) in *ex-vivo* chicken breast. The waveform was obtained by coherently averaging over 1,000 sweeps (10-ms HIFU bursts) which took more than 20 s. No lesion was formed in this case.

It should be pointed out that the exposure parameters used for this example were not sufficient to lesion the tissue, which resulted in a constant value for V_{pp}. However, if the optical properties of the tissue had been affected through the formation of a lesion, the increased attenuation would reduce the number of “tagged photons” and the depth of modulation (Sakadzic and Wang 2005; Kothapalli *et al.* 2007; Lai *et al.* 2009a). Therefore V_{pp} would be reduced over time, as the lesion grows in size. Since the averaged waveform in Figure 5.8 took up to 20 s to acquire, simple time averaging is not suitable for real-time monitoring. The LA was implemented in this study to increase this speed by virtue of the reduced bandwidth afforded by lock-in detection (i.e. less noise).

We set the LA integration time constant to 30 ms, with a 12 dB/octave roll off. The continuous output of the LA, denoted as $S(t)$, was proportional to the RMS of V_{pp}. This value was streamed and recorded on the personal computer at a rate of 7 Hz and displayed as a function of exposure time.

The value of AO signal amplitude varied from sample to sample (Lai *et al.* 2009), so the value of $S(t)$ of each exposure was recorded and normalized as $NS(t)=S(t)/S_0$, where S_0 was the initial value for each exposure, and it was defined in this study as the mean value of $S(t)$ measured in the time window of 2-5 s from the start of the exposure, when no lesion was formed. The change of AO signal amplitude during the exposure was then quantified as

$$\Delta S(t)=\left|NS(t)-1\right|\times 100\%=\left|S(t)/S_0-1\right|\times 100\%. \tag{5.1}$$

5.3.4. Passive cavitation detection

A 7.5 MHz single element, focused transducer (140-710-S, Olympus, MA, USA, diameter 15.9 mm, focal length 57 mm), was used as a passive detector (UT_2 in Figure 5.4) of cavitation noise and installed in the central aperture of the HIFU transducer, aligned concentrically, coaxially and confocally with respect to the HIFU field as shown in Figure 5.9. During the HIFU exposure, this transducer functions passively, receiving acoustic signals originating from its focal region, which was also the focal region of the HIFU field.

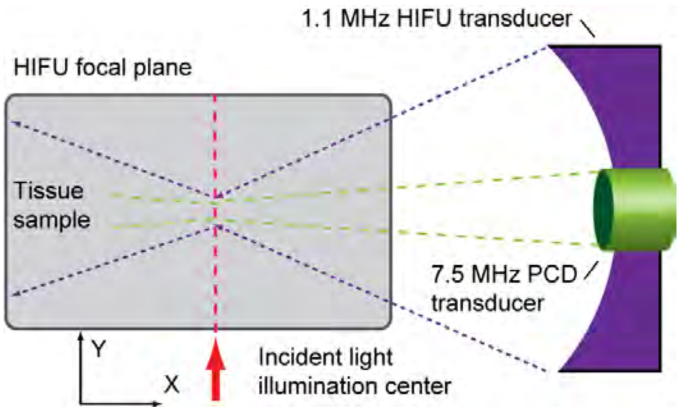

Figure 5.9 Schematic of PCD transducer positioning with respect to the HIFU field and incident light illumination.

The acoustic signals sensed by this “passive cavitation detector” (PCD) originate from two mechanisms: (a) the scattering of the fundamental and the non-linear components of the HIFU field from tissue inhomogeneities and/or bubbles and (b) the broadband acoustic emissions from bubbles (Leighton 1997). The detected signals were high-pass filtered at 5 MHz (F5081, Allen Avionics, NY, USA) in order to minimize the HIFU fundamental and the first three harmonics of the detected signals. The filtered signals were then amplified by a low noise preamplifier (40 dB, Model 5185, EG&G, MD, USA) and recorded using the oscilloscope (Figure 5.4). The oscilloscope was triggered by the function generator corresponding to the start of a HIFU burst, and the PCD traces were digitized at a rate of 25 Msample/sec with a window of length of 200 μs (with a delay of 72 μs to allow for time of flight of the HIFU field and any emissions from the focal region). The digitized signals were downloaded through the GPIB interface to the personal computer, at a constant rate of 7 Hz. The data transfer time ultimately limited the speed of acquisition used in this study. After the exposure, the PCD signals were processed in Matlab (McLaughlan 2008; Farny *et al.* 2009) to obtain the level of broadband acoustic emissions, which served as an indication for inertial cavitation in the HIFU/PCD confocal volume. The gray, real curve in Figure 5.10 shows the corresponding PCD signal, which remained between 0.3-0.4 volts during the exposure, indicating that no inertial cavitation was detected during the exposure. In the comparison, the black, dashed curve in Figure 5.10 shows an example of PCD broadband emission as a function of time when inertial cavitation was generated during another exposure in another tissue sample with the signal associated with cavitation beginning at approximately 27 s.

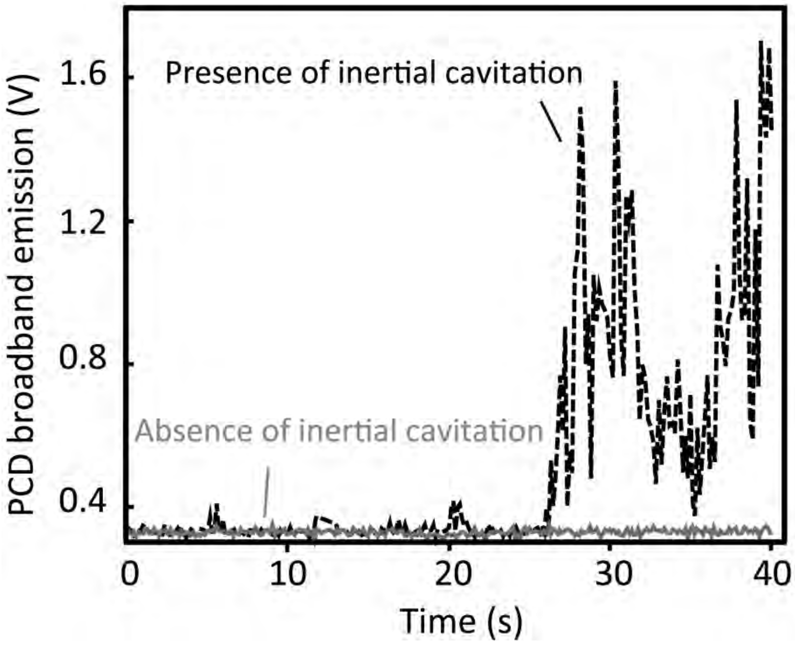

Figure 5.10 The PCD broadband emission as a function of exposure time from two exposures. The real and dashed curves represent the scenario without and with the presence of inertial cavitation during the exposure, respectively.

5.3.5. Active cavitation detection

A commercially available diagnostic ultrasound imaging system (TUP in Figure 5.4), Terason 2000 (Terason Tech, MA, USA) employing a 128-element, 38-mm aperture linear probe (10L5, center frequency of 7.5 MHz, focal distance set at 50 mm) was used to image the tissue samples and sense the onset of hyperechogenic regions associated with stable cavitation and boiling. The array was aligned parallel to the propagation direction of the HIFU field (X axis) and perpendicular to the light path. It was aligned such that the focal peak of the HIFU was approximately in the centre of the array and 50 mm away from the transducer along the imaging acoustic axis. B-mode ultrasound images were acquired immediately before and after each HIFU exposure. The presence of boiling was identified through the changes in hyperechogenicity in the focal region of the HIFU transducer (Rabkin *et al.* 2006) as shown in Figure 5.3.

5.3.6. Characterization of the lesion volume

The lesion volume was estimated for each exposure. Each sample was dissected using a skin-graft knife (SM9940, Cincinnati Surgical Company, OH, USA). They were first cut along the approximate position of the HIFU focal plane (Figure 5.11a) in order to identify the centre of the lesion in the Y direction, and then along the XZ plane to expose the central cross-section of the lesion. A photograph of this cross-section, with a millimeter scale rule, was taken using a digital camera (M763, Kodak, NY, USA) for every lesion. Figure 5.11(a) shows an example photograph of a lesion cross-section produced by a 3300 W/cm^2 (free field peak intensity, 10 MPa peak pressure) 50 s exposure, with the

HIFU propagating from left to right along the X axis. A Matlab routine was developed to identify the lesion boundary in the tissue based on an iso-intensity contour threshold method, as shown in Figure 5.11(b).

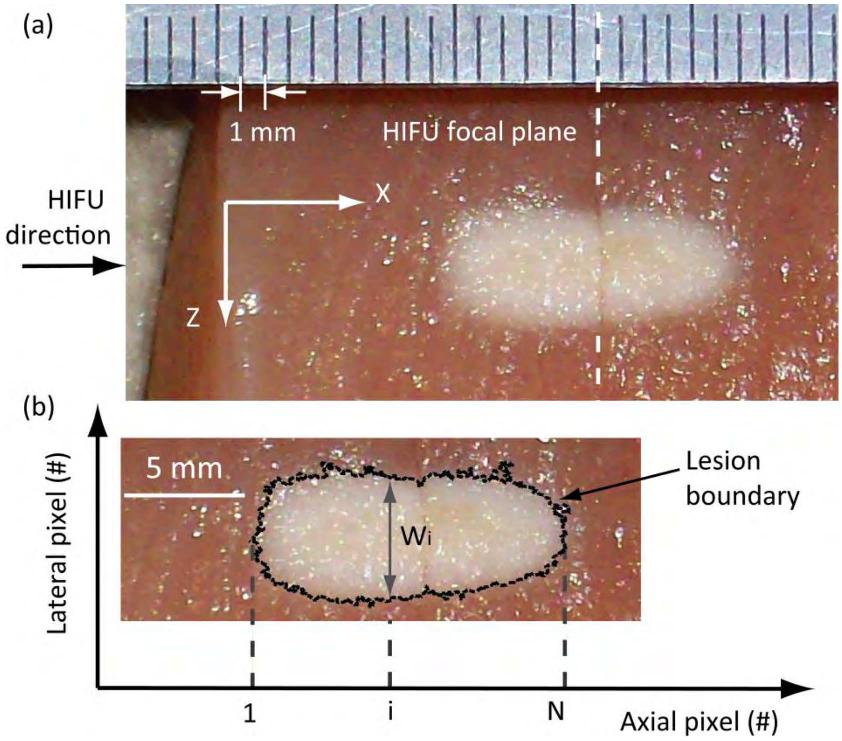
(a)
1 mm
HIFU focal plane
HIFU direction
X
Z
(b)
Lateral pixel (#)
5 mm
Lesion boundary
Wi
1
i
N
Axial pixel (#)

Figure 5.11(a) A cross-section photo of a lesion produced in *ex-vivo* chicken breast by a 3300 W/cm^2 (peak intensity, 10 MPa peak pressure) and 50 s exposure. The HIFU direction was from left to right, with its focus plane 16 mm into the tissue along the X direction. (b) The photograph of the lesion with its boundary outlined by dashed black lines.

For volume estimation it was assumed that the lesion was axis-symmetric. This is a reasonable approximation for this study which employed relatively homogeneous tissue samples devoid of large structural defects like big blood vessels, and did not employ acoustic intensities sufficient to induce inertial cavitation activity or boiling. The lesion volume, denoted as LV, was estimated using the equation

$$LV = \sum_{i=1}^{N} \left\{ \pi(\frac{W_i}{2}) / C_p^{\,3} \right\}, \tag{5.2}$$

where N is the total amount of pixels along the length of the lesion, W_i is the lesion width at acoustic position *i*, and C_p is the pixel calibration factor, defined as the number of pixels per mm distance in the cross-section photograph. The same procedure was performed for all lesions in the study, which could then be compared with their corresponding AO signal amplitude reduction ($\Delta S(t)$). It should be mentioned here that this calculation of lesion volume is more representative of the true geometry than describing the lesion as a circular cylinder or perfect ellipsoid (Meaney *et al.* 1998). Although we do assume axis-symmetric, it must also be noted that the act of removing the sample from the tissue holder might have led to geometric deformation sufficient to modify the measured dimensions of the lesion (Zheng and Vaezy 2008).

5. 4. Experiment results

Figure 5.12 (a) shows a typical non-normalized AO signal amplitude plot $S(t)$, from a single 3300 W/cm^2 (10 MPa peak pressure) 40 s HIFU exposure in *ex-vivo* chicken breast. The figure shows $S(t)$ increased from 0 to 29 mV in less than 1 second after the HIFU was turned on. Between 2-5 s, $S(t)$ had a mean value $S_0 = 29.5\,\text{mV}$ with a standard deviation of 0.29 mV. After 8 s, $S(t)$ started to decrease and obtained a value of 14.9

mV by the end of the exposure. Figure 5.12 (b) shows the corresponding PCD broadband emission as a function of time, indicating that no inertial cavitation was detected during this exposure. Two B-mode images acquired immediately before and after this non-cavitating exposure are displayed in Figure 5.12 (c) and (d), where the dashed box indicates the approximate position of the HIFU focus. No change in echogenicity was observed as a result of this exposure, suggesting that no boiling occurred. Figure 5.12 (e) shows the cross-section photograph of the lesion generated from this exposure, where the HIFU propagated from left to right along the X axis. With Eq. (5.2), the volume of this lesion was estimated to be 252 mm^3. Although no evidence of this lesion was identifiable from the B-mode images, the reduction in $S(t)$ during the exposure indicates a change in the optical properties of the sample.

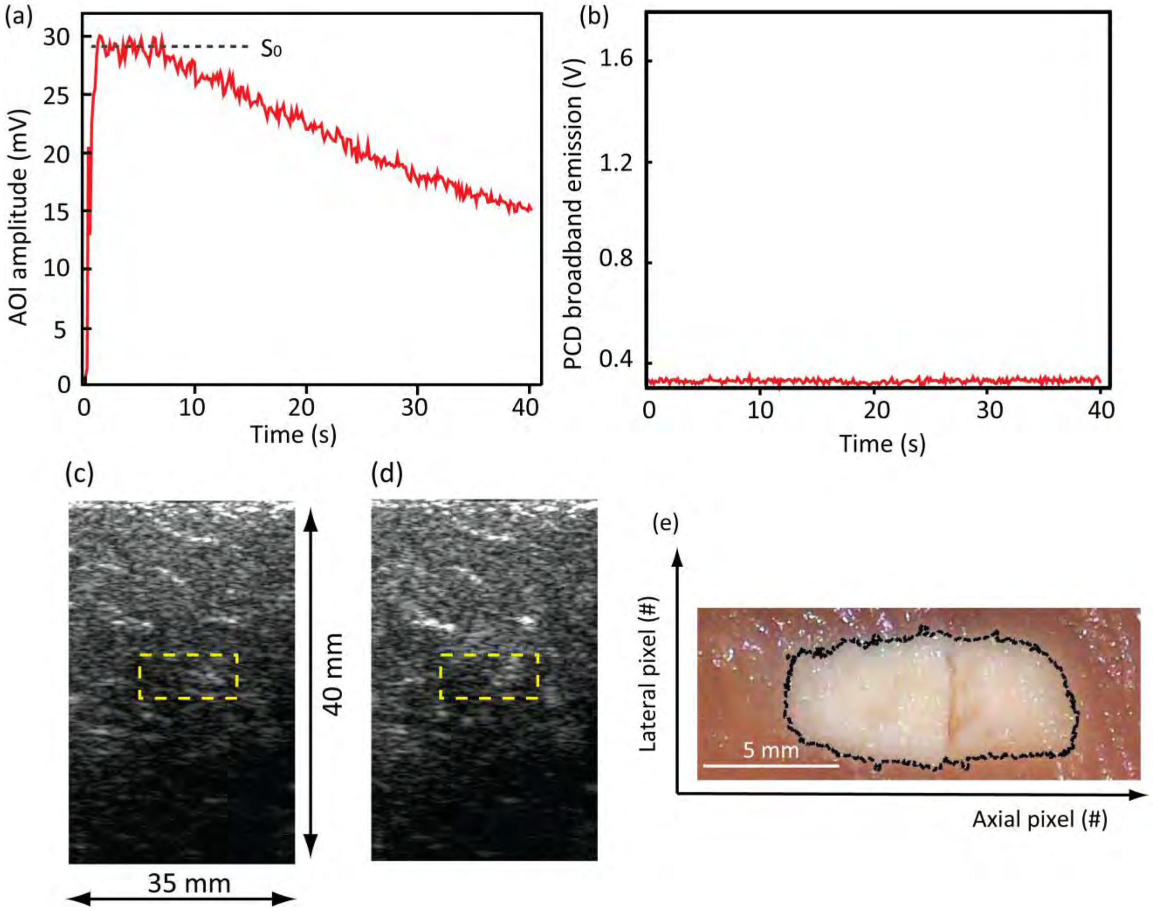

Figure 5.12 Examples for a typical 3300 W/cm^2 (peak intensity, 10 MPa peak pressure) 40 s exposure in *ex-vivo* chicken breast: (a) non-normalized AOI amplitude as a function of exposure time; (b) PCD signal as a function of exposure time; B-mode ultrasound images acquired immediately (c) before and (d) after the exposure (the dashed box indicates the approximate location of the HIFU focus); (e) A photograph of the cross-section of the lesion generated by this exposure (HIFU field propagated from left to right, and the bar length represents 5 mm spatially).

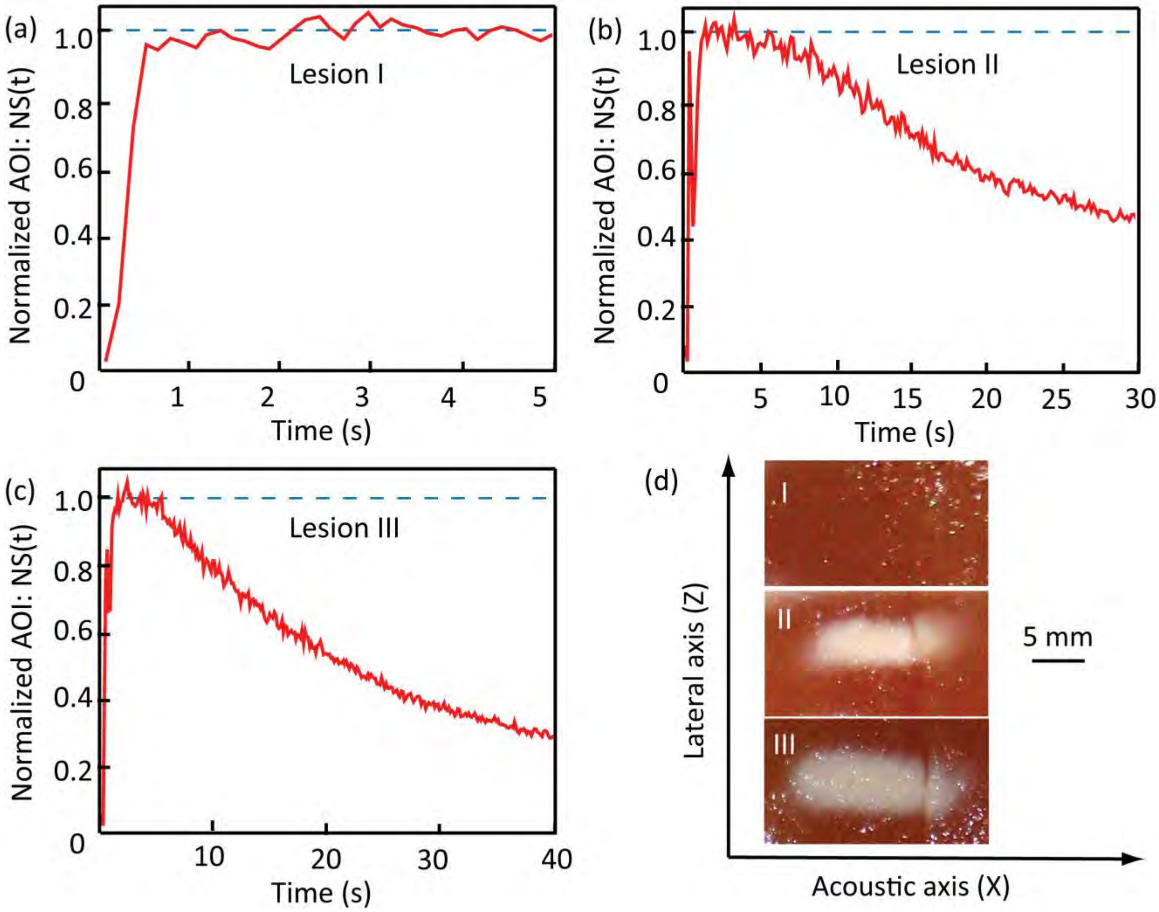

Figure 5.13 Normalized AO signal amplitude as a function of time for three HIFU exposures in one single tissue sample with the same peak intensity (3300 W/cm^2, 10 MPa peak pressure) but different durations of (a) 5 s, (b) 30 s, and (c) 40 s; (d) Photographs of the cross-sections.

In order to demonstrate how the AO signal is affected by lesion size, three exposures were performed in a single tissue sample at different locations along the Z direction. Each exposure had the same peak intensity (3300 W/cm^2, 10 MPa peak pressure) but the exposure times were 5, 30 and 40 s. Figure 5.13 (a)-(c) shows the normalized AOI amplitude, $NS(t)$, and the corresponding lesion cross-sections are displayed in Figure 5.13 (d). For each of the exposures $NS(t)$ increased from 0 to 1 in less than 1 s after the HIFU exposure was turned on. The signal spiking observed in the initial rise of (b) and (c) was related with the set detection bandwidth of the LA. Between 2-5 s, $NS(t)$ had a constant value of 1.00 ±0.03 for three exposures. For the 5 s exposure, there was no change in $NS(t)$ greater than ±0.03 throughout the entire exposure, which corresponded to no lesion present in the tissue. However, for the longer exposures, $NS(t)$ started to reduce around 5-7 s, ending at 0.45 for 30 s exposure and 0.28 for 40 s exposure (Figure 5.13b-c). The measured lesion volumes were 250 and 470 mm^3 respectively (Figure 5.13d), suggesting that the greater reduction in $NS(t)$ correlates with larger lesion volume. In both Figure 5.13(b) and (c), we interpret the knee of the $NS(t)$ curves at 5-7 second to indicate the onset of lesion formation.

In order to further explore the relationship between normalized AOI reduction, $\Delta S(t)$, and the corresponding ensuing lesion volume, 72 exposures were performed with fixed pressure and duration (Group 1, Table 1). A further 87 exposures were performed with varied pressures and/or durations (Group 2, Table 1) to further study how the relation between $\Delta S(t)$ and lesion volume was affected by the exposure parameters. For each of these exposures, the PCD signals and B-mode images confirmed the absence of inertial cavitation and boiling for all exposures in the study.

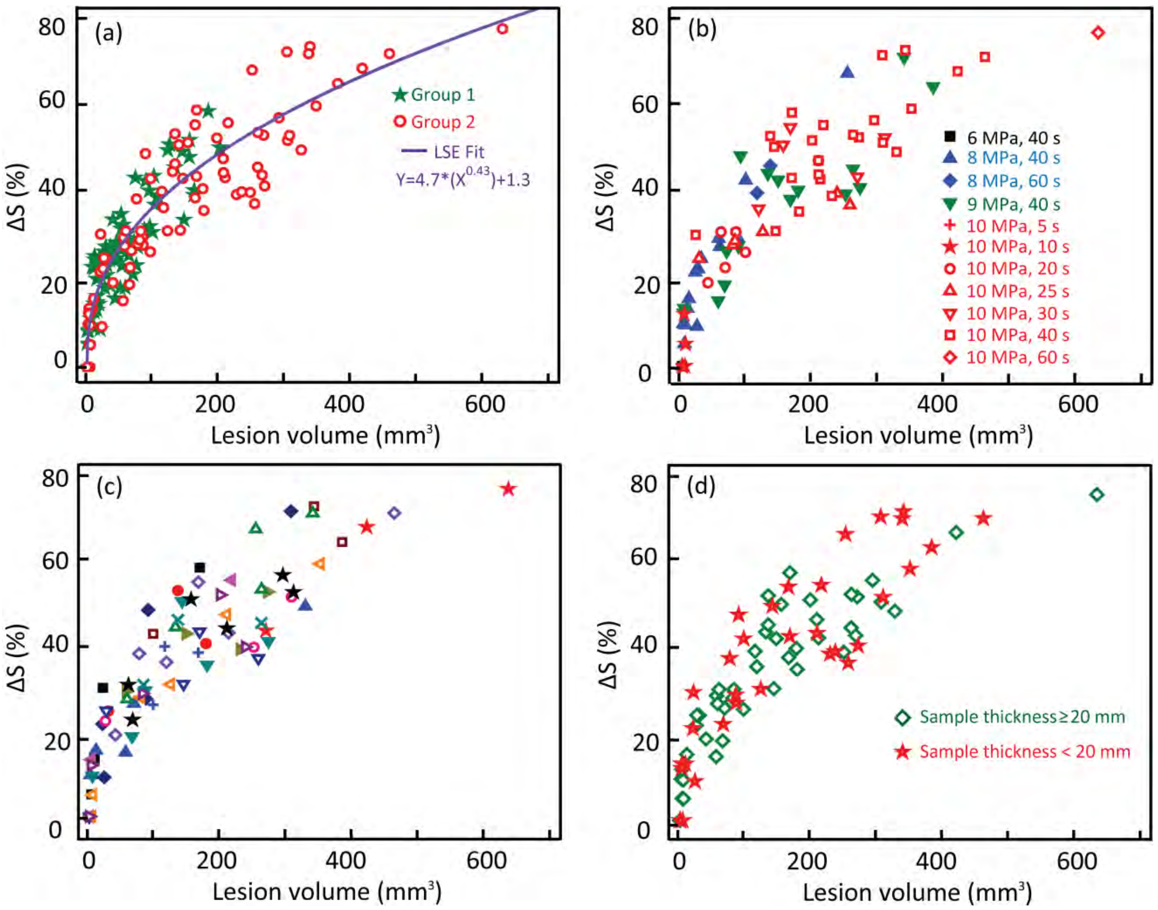

Figure 5.14 (a) The normalized AO signal amplitude change ΔS as a function of resulting lesion volume for Group 1 (stars), and 2 (circles) exposures as well as the LSE fit for the data (line). The correlation between AO signal amplitude change and resulting lesion volume for Group 2 exposures were sorted according to the exposure parameters (b) sample source (c) and sample thickness (d). Each color symbol in (c) represents one sample cut from the same chicken breast.

Figure 5.14(a) shows the correlation of $\Delta S(t)$ with the measured lesion volume for Groups 1 (green stars) and 2 (red circles) as well as the least square error (LSE) power fit for the measurements (purple line). From Group 1 data, it can be seen that when using the same pressure and exposure duration, the ensuing lesion volumes were broadly distributed, ranging from 0 to 205 mm^3. However, despite this large distribution in lesion volume, the level the level of $\Delta S(t)$ nevertheless is correlated with the measured volumes. This data indicates the measured reduction in AO signal level is a much better predictor of lesion formation than the acoustic source driving parameters. The correlation between $\Delta S(t)$ and lesion volume remained consistent when different exposure parameters were employed as shown from the Group 2 data in Figure 5.14(a). The Group 2 data is re-plotted in Figure 5.14(b)-(d), with the symbols in each plot corresponding to different experimental parameters. In Figure 5.14(b), each symbol corresponds to a given exposure pressure and time, while in Figure 5.14(c) the symbol represents measurements on a different chicken breast. Finally in Figure 5.14(d) the symbols indicate whether the sample is thick (> 20mm) or thin (< 20mm). Taken as a whole, Figure 5.14 serve to underscore the wide variety of samples tested and the fact that $S(t)$ tends to track lesion volume irrespective of exposure parameters, sample source and geometry.

For HIFU treatments, it is imperative to ensure that the desired target volume is necrosed while the neighboring healthy tissues are not adversely affected. Therefore, predictable and repeatable shapes and sizes of necrosed regions are required to avoid inadequate or excessive heating. In order to use AO sensing to guide HIFU therapy in real time, measurements of the instantaneous $S(t)$ were continuously streamed to the computer at a rate of 7 measurements per second. HIFU exposure was continued until $\Delta S(t)$ equaled or exceeded the user preset threshold AO change at which point the HIFU exposure was immediately terminated. A flow chart of the exposure process is given in Figure 5.15.

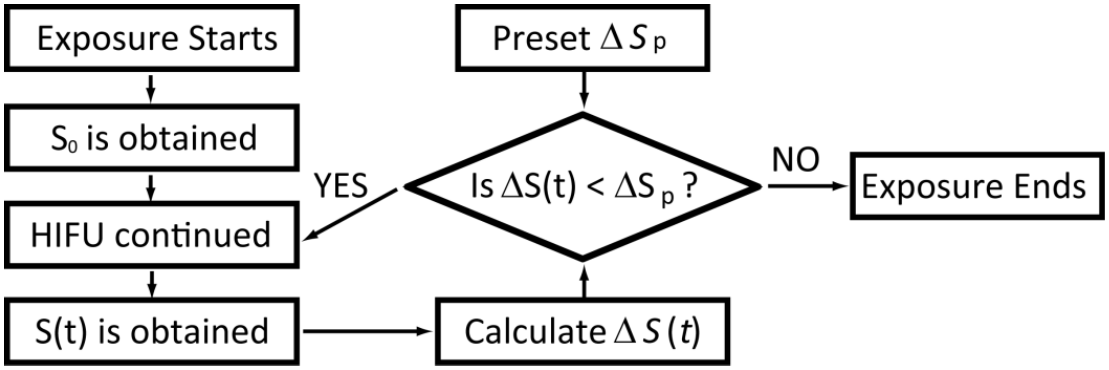

Figure 5.15 The feedback method used for guiding the exposure using the measured AO response.

To demonstrate the efficacy of this approach compared with exposures employing fixed time durations, 157 repeat exposures (Group 3, Table 5.1) were performed at the same peak intensity (3300 W/cm^2, 10 MPa peak pressure), with the exposure duration regulated in real time by the method described above. These were compared with another series of 189 exposures at a fixed intensity (Group 4, Table 5.1) but a number of preset exposure durations. Table 5.2 shows the mean and standard deviation of the resulting exposure durations corresponding to each ΔS_p for Group 3, and Figure 5.16 illustrates the distribution of the resulting lesion volumes as a function of (mean) exposure durations for Groups 3 and 4. As we can see from Figure 5.16, when the exposure durations and/or the mean of lesion volumes were approximately equivalent, a 30-40% decrease in the standard deviation of the lesion volumes was obtained when a preset AO reduction threshold was used as the criteria to guide the exposures. In addition, the lesion volumes shown in Figure 5.16 for different ΔS_p agree quite well with the estimated lesion volumes based on the LSE fit in Figure 5.14(a).

Table 5.2 Mean and standard deviation (STD) of durations for Group 3 exposures

ΔS_p (%)	20	30	40	50	60
Mean (s)	25	31	38	57	67
Standard deviation (s)	7	9	10	15	22

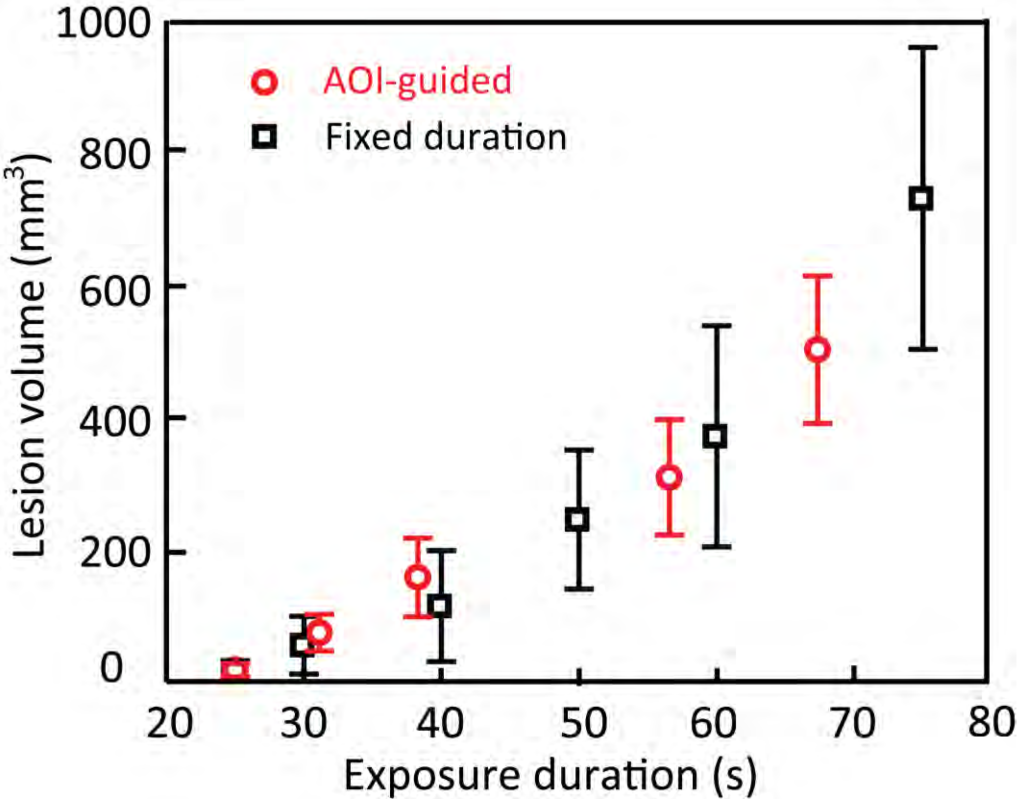

Figure 5.16 Lesion volumes as a function of exposure duration for exposures guided by AO response (circles, with 20, 30, 40, 50 and 60% preset ΔS_p from left to right) and exposures with fixed durations (squares, with 25, 30, 40, 50, 60, and 75 s from left to right). The height of the position and the error bar represent the mean value and the standard deviation of the lesion volumes, respectively.

5. 5. Discussion

5.5.1. AO monitoring of exposures

The objective of this study was to develop an integrated AO sensing system to monitor the onset and growth of HIFU lesions in ex-vivo chicken breast in real time. The amplitude of the detected AOI signal was affected by a number of parameters which included the amount of light reaching the AO interaction region, the optical path length through the tissue, the characteristics of the ultrasound field, the characteristics of the PRC configuration (size, absorption coefficient and TWM gain coefficient), as well as the optical properties of the AO interaction region (Lai *et al.* 2009). During the process of HIFU exposure, the reduction of AOI amplitude in Figure 5.12 (a) was associated with an increase in optical absorption and scattering coefficients due to the formation of a lesion within the AO interaction region, the existence of which was confirmed by the cross-section photograph. We note that lesions created in this study were unable to be visualized with B-mode ultrasound and likely this was due to the absence of cavitating bubbles, which highlights the need for a more robust detection method.

It was found (Figure 5.13a-d) that the AOI response was correlated with the lesion volume. The extent of tissue damage depends on a number of factors, such as the profile and the intensity of the HIFU field, exposure duration, acoustic path length in the tissue, as well as the physical properties and the functional status of the overlying tissues between the transducer and the focal region (ter Haar 1995; Meaney *et al.* 1998; Wang *et al.* 2003). Samples that were found to contain large blood vessels upon subsequent dissection photography were excluded from the data set in this study. Despite constant HIFU pressure and exposure duration, large variations in the ensuing lesion volumes were observed (Figure 5.14a, Group 1), likely due to inhomogeneities in the tissue samples, which can cause acoustic reflection, refraction, scattering and diffraction (Wang *et al.* 2003). The large variations in lesion volumes were in agreement with previously published data (ter Haar *et al.* 1989; Meaney *et al.* 1998; Wang *et al.* 2003; Li *et al.* 2006).

Interestingly, the normalized AO signal amplitude of an exposure changed proportionally with the volume of the resultant lesion (Figures 5.14a-d), and the correlation was unaffected by the exposure parameters, sample source and sample geometry at the given range. This is the case because the normalized AO signal amplitude reduction, as discussed earlier, was solely caused by the formation of a lesion. The larger the volume of such a lesion, the fewer the number of photons "tagged" by the ultrasound, resulting in a greater reduction in AO signal. Therefore, the change in AO response during exposure could potentially be used to determine the onset and development of a HIFU lesion. This is of significance since real-time feedback of lesion formation is still a challenge for HIFU treatments.

5.5.2. AOI-guided exposures

To guarantee the efficacy of HIFU treatments it is important to ensure that the desired tumor volume is necrosed while damage to neighboring healthy tissues is kept to a minimum. Therefore, the ability to predict consistently the size and shape of necrosed regions is of importance. Unfortunately, the volumes of individual lesions, many of which would be required to ablate a complete tumor, can vary due to the aforementioned factors. As a result, inadequate or excessive heating might be employed in practice, resulting in incomplete tumor ablation or damage of healthy tissues. In this study, the use of AO sensing was proposed as an exposure-guidance method in order to obtain less variability in lesion volume (Figure 5.15). Statistical analysis of the measurements (Figure 5.16) demonstrated significant improvements in the consistency and repeatability of individual lesion volumes by using feedback from AO sensing in contrast with using fixed exposure parameters to guide tissue necrosis. It should be mentioned at this point that these measurements were performed in relatively homogeneous chicken breast samples, representing the best scenario for HIFU exposures. For *in vivo* applications, exposures with fixed duration would produce more diverse lesions in terms of volume, whereas the AOI-guided exposures should be immune to such changes as the AO response is normalized to the initial level for each exposure. These suggest that AO sensing could potentially be used to improve treatment planning and efficacy evaluation.

5.5.3. Limitations of lesion detection

In our experimental setup, accurate prediction of lesion volume was limited by the size of the HIFU focal volume, which consequently limits the AO sensing volume. (AO signal strength is roughly quadratic in the pressure amplitude (Lai *et al.* 2009).) This effect was reflected in the correlation curve in Figure 5.14. When the lesion volume was less than 40

mm^3 (corresponding to the contour volume of FWHM of the peak pressure), $\Delta S(t)$ increased approximately linearly with the lesion volume, as expected. Above 40 mm^3, however, the curve plateaued due to the pressure contours of the HIFU field, outside of the main focal zone, giving a lower detection sensitivity for AO. In order to accurately detect or guide the formation of larger legions, the AO sensing region could be expanded by using an additional transducer with a larger focal field to pump the AO interaction, provided this larger beam does not exceed the optical illumination region.

5.5.4. Influence of inertial cavitation

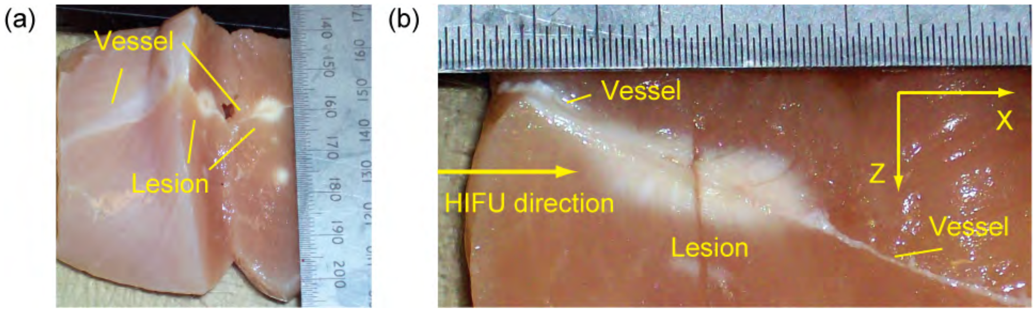

Figure 5.17 Lesion photos (a) along the focal plane and (b) in the XZ plane when the HIFU field propagated across a big blood vessel in an *ex-vivo* chicken breast sample.

As mentioned previously, the data reported in this study were obtained using HIFU exposure intensities that are too low to generate inertial cavitation in the tissue in most instances. However, when the HIFU beam traversed across large blood vessels, as shown in Figure 5.17, four out of five 10 MPa, 40 s HIFU exposures (these five data set were not included Table 5.1) resulted in inertial cavitation being detected by the PCD (the red curve in Figure 5.18). The corresponding AO signal amplitude as a function of time is also shown in Figure 5.18.

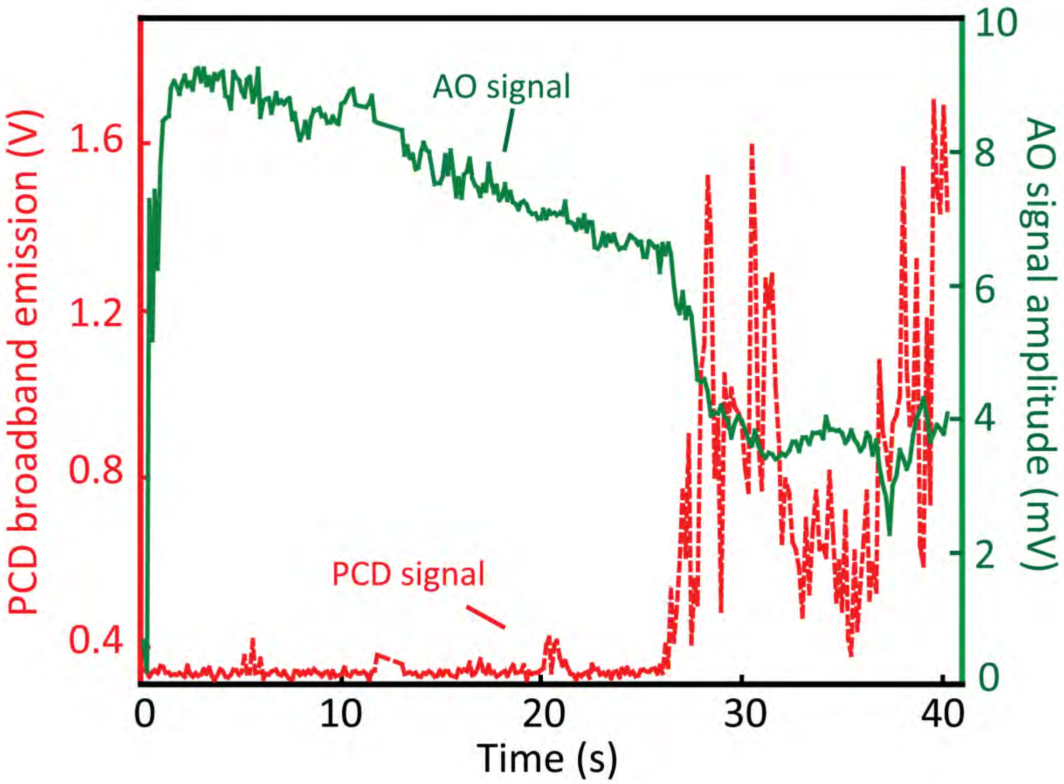

Figure 5.18 The PCD broadband emission (dashed line) as a function of time when inertial cavitation activity was detected during a HIFU exposure and an example of corresponding AO response (real line) as a function of time.

As we can see from Figures 5.17 and 5.18 that the existence of structural defects like large blood vessels increases the possibility of generating inertial cavitation, which in turn serves to distort the orientation and shape of the lesion . The bubble activity excited pre-focally serves partially "block" the propagation of HIFU field to into the focal region. This so-called "shielding" effect may account for the sudden reduction in AO signal amplitude in Figure 5.18, as the ultrasound modulation is proportional to the square of the *in situ* ultrasound pressure amplitude in the AO interaction region. Thus when there is inertial cavitation, the correlation between $\Delta S(t)$ and the lesion volume breaks down, as shown in Figure 5.19. The deviation originates primarily from the erratic reduction in $S(t)$ and the increased error in lesion volume estimation based on Eq. (5.2). The physical mechanisms and potential consequences of these phenomena, however, require further study.

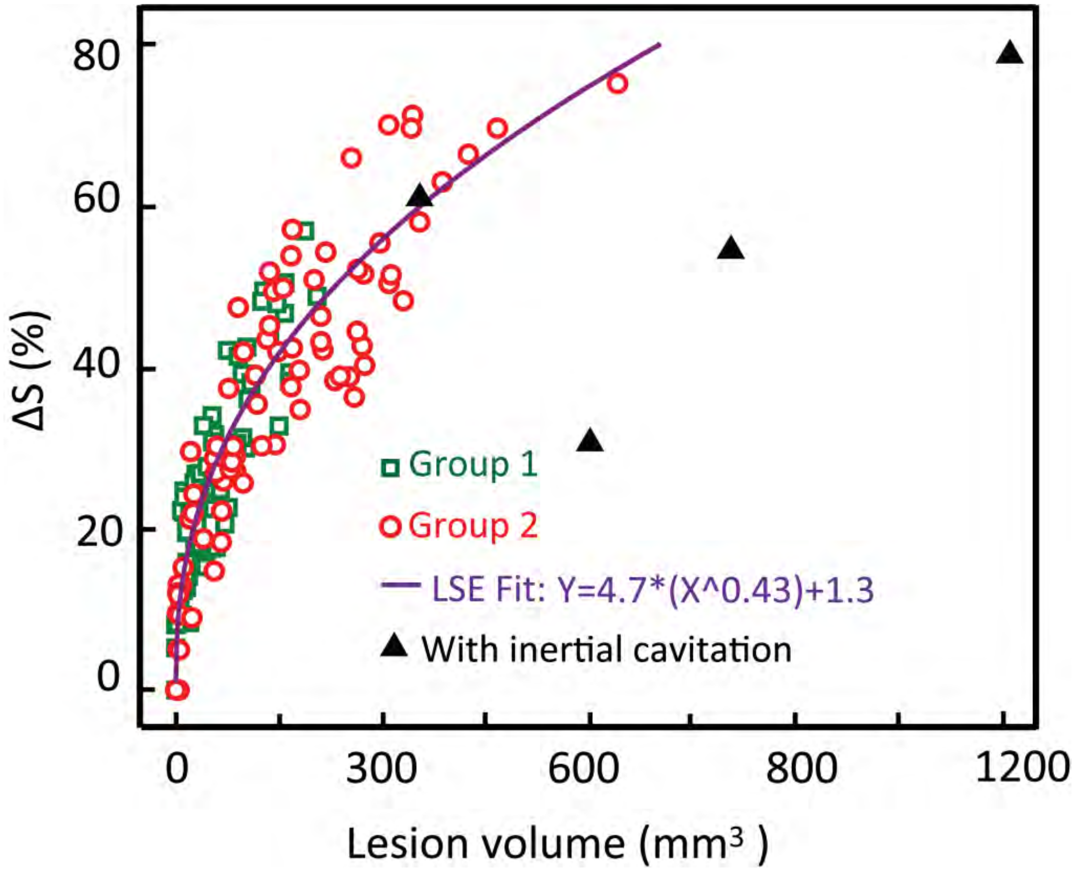

Figure 5.19 The relationship between AO signal amplitude change and lesion volume for four exposures (triangles) when inertial cavitation occurred during the exposure.

5. 6. Summary

In this Chapter we describe a series of experiments in which the GaAs PRC-based AO sensing system was modified and used to sense and monitor, in real time, the formation of lesions under HIFU exposures. The same HIFU field induced tissue heating and pumped the AO interaction. Because the same acoustic beam was used for both therapy and sensing, alignment was automatic. The AO signal amplitude change during exposure correlated with the resulting lesion volume, which suggests that AO sensing could improve the efficacy of HIFU exposure evaluation in organs that support diffusive optical fields; notably breast, brain, and prostate. The use of AO sensing for real-time feedback yielded a 30-40% improvement in the consistency of resultant lesion volumes, compared with fixed duration exposures. Although the system was not optimized for *in vivo* trials, this exploratory study indicates that *in vivo* HIFU guidance using AO sensing may indeed be feasible. Moreover the technique studied in this paper is not limited to HIFU therapy, but could potentially be used for treatment monitoring of other thermal ablation therapies such as laser and microwave.

Chapter 6

Summary and Conclusions

6. 1. Objectives and goals

The overall goals of this research are to (a) better understand the nature of ultrasound-induced modulation of diffusive light in turbid media, (b) design and construct a photorefractive crystal-based AO imaging system operating in the near infrared optical wavelength regime, and (c) use this system to quantitatively measure the optical properties of tissue mimicking materials and for real-time monitoring of HIFU treatment process. To fulfill these objectives, studies in four topics have been thus far performed and documented in the dissertation.

6. 2. AO sensing in the NIR

The physical principles of ultrasound-induced modulation of diffuse light are discussed in the context of an analytical model based on the two acknowledged mechanisms for light-sound interaction: periodic variations in medium refractive index and periodic optical scatterer displacement. It is shown that the optical phase modulation due to each mechanism, when acting independently, is proportional to the square of ultrasound focal pressure amplitude and averaged number of scattering events. When the acoustic wavelength is large compared to optical mean free path length, the phase increments induced in consecutive scattering events by both mechanisms are somewhat correlated, probably because the phase of the sound field is relatively constant along the optical path. Moreover, there is non-negligible correlation between phase increments due to the aforementioned mechanisms, which is destructive (negative) and possesses a magnitude that is also proportional to focal pressure amplitude squared and averaged number of scattering events. The strength of the *net* optical phase modulation induced by ultrasound decreases with ultrasound frequency and optical transport coefficient (sum of absorption and scattering coefficients), which has been confirmed experimentally in previous studies. This dependence of modulation strength on optical properties functions as the theoretical foundation for quantitative optical measurements using pressure contrast AO sensing, a new approach developed in the research.

A GaAs photorefractive crystal-based AO system operating at 1064 nm optical wavelength is successfully developed and deemed more suitable for sensing in tissue and tissue like phantoms. The characterization, optimization, and operational theory of this system are detailed. This system serves as the experimental platform in the study.

A modified approach, based on standard AO sensing techniques, is developed to *quantify* the optical properties of diffuse media. We measure the ratio of standard AO signals generated when insonifying the same sample volume with successive, short-duration ultrasound pulses at two different focal pressures. The resulting "pressure contrast signal" (PCS), is solely dependent on the mean phase shift imparted on the diffusive light from the ultrasound perturbation. Once calibrated for a particular ultrasound pulse shape and pressure set, the PCS yields a direct measure of the spatially averaged optical transport attenuation coefficient within the AO interaction region. It is also shown that the PCS measurements yield materials properties that consistent in either homogeneous media or embedded optical inhomogeneities. Experiments further demonstrate that pressure contrast AO sensing can potentially be used for (a) detecting/imaging the optical inhomogeneities in tissue and (b) producing a quantitative measure of the optical properties of optically diffuse media without *a priori* knowledge of the background media in which the heterogeneities are embedded.

6. 3. AO sensing for guiding HIFU therapy

The fact that tissue optical absorption and scattering coefficients are irreversibly increased by the formation of thermally necrosed regions under HIFU exposure suggests that AO sensing techniques can be used for monitoring HIFU treatment in real-time. A fixed, focused ultrasound beam is used to induce tissue heating as well as pump the AO interaction, thereby automatically co-registering with AO sensing volume with the expected location of HIFU lesion formation. Experiments performed in *ex-vivo* chicken breast demonstrate that the change in AO signal amplitude during an exposure is correlated with the resulting lesion volume, suggesting the AO sensing can be used to characterize the onset and subsequent development of a lesion in real time. Experiments using the AO response for real-time feedback to control HIFU exposure duration result in more consistent and predictable lesion formation when compared with results obtained with fixed HIFU exposure duration.

6. 4. Suggestions for future work

Work performed in this dissertation, like the plurality of current studies in the area of AOI, was performed in either tissue-mimicking phantoms or *ex vivo* tissue. Further improvements are required to make this technique suitable for clinical trials.

6.4.1 Improvement of effective sensing depth

The most critical limitation of AOI technique comes from limited sensing depth in tissue caused by the typically low SNR of AO signals. Presently, the majority of AO systems (Murray *et al.* 2004; Ramaz *et al.* 2004; Sakadzic and Wang 2004; Bossy *et al.* 2005; Kim *et al.* 2006; Bossy *et al.* 2007; Li *et al.* 2008; Lai *et al.* 2009), including the one used in this study, employ CW lasers as the light source where the maximum permissible exposure (MPE) for safe clinical usage is strictly limited. In addition, only the light traversing the AO interaction region is modulated by the ultrasound, which is typically detected against a much stronger background of unmodulated light. The total amount of tagged light that can be collected outside the tissue sample is therefore small and the SNR poor. Even though the incident laser intensity (200 mW/cm^2) and the sample thickness in this study (less than 30 mm) did not test the upper limit of system sensitivity, the system described in this dissertation was not optimized for clinical applications, where relevant sensing depths are typically more than 50 mm (Wang 1998). Given recently reported progresses in increasing AO signal SNR by incorporating a pulsed laser with high peak intensity but low duty cycle (Rousseau *et al.* 2008; Rousseau *et al.* 2009) and/or the possibility of more efficient demodulators based on, for example, confocal Fabry-Perot

Interferometer (CFPI, Sakadzic and Wang, 2004) and spectral-hole burning crystals (SHBC, Li *et al.* 2008), we believe that deep-tissue, real-time imaging of tissue optical properties using AO sensing could become a reality. In addition, the enhancement in tagged photon flux afforded by greater peak laser intensity will speed up the response of PRC demodulators, helping to diminish the mitigating influence of room/platform vibration and/or physiological motion *in vivo*.

6.4.2 Improvement of sensing speed and image-guidance HIFU treatments

The improved system SNR discussed above can also facilitate faster pressure contrast AO sensing. For pressure contrast AO, the coherent average of a large number of ultrasound pulses (typically 10,000) are required to get a single AO scan line, from which a single PCS was computed. This procedure was then repeated several time (8-80 times in our experiments) to obtain an estimate of the mean PCS along the ultrasound scan line, a process that proved to be quite time consuming. Indeed, obtaining a pressure contrast AO image of an embedded optical inclusion in two dimensions with desirable contrast and resolution could take hours. With enhanced SNR, fewer samples will need to be averaged, reducing the time required to get a scan line and potentially allowing for quantitative optical sensing and imaging *in vivo* using pressure contrast AO.

For the HIFU treatment monitoring, the AO amplitude change, monitored in real time, was used as a metric to infer the size of the lesion formed in the tissue sample. However, with potential improvements in system SNR, real-time 2-D imaging of the HIFU focal region during the exposure may prove feasible, providing the location and shape of the necrosed region. This could be accomplished by using a clinical ultrasound-imaging machine to both form B-mode structural images *and* pump the AO response. This approach was used for imaging optical absorption contrast by Bossy *et al*. (2005) in tissue phantoms and excised tissue samples.

6.4.3 Optical illumination and detection alignment

The AO system described in this study employs a transillumination geometry in which the laser source and detector are on the opposite sides of the sample, and the ultrasound propagates perpendicular to the source-detector axis. This alignment, however, has severe drawbacks for medical imaging, for in many situations transillumination is impractical or might call for much larger penetration depths. A more convenient configuration is to install the source and detector on the same surface of the sample. The feasibility of this reflection configuration for AO imaging has been successfully demonstrated (Lev *et al.* 2000; Granot *et al.* 2001; Li and Wang 2004; Sakadzic and Wang 2004; Kothapalli and Wang 2009). However, it should be noted that the background ("untagged") photon flux is much higher in a reflection geometry than in a transillumination geometry, which makes detection of the tagged photons emanating from deep within the tissue more challenging, which in turn could compromise signal SNR.

Bibliography

American Cancer Society, "Breast Cancer Detailed Guide", (2009)

American National Standards Institute, "American National Standard for the Safe Use of Laser in Health Care Facilities, ANSI Z1361.1", American National Standards Institute, New York, (2000)

Arridge, S. R., "Optical tomography in medical imaging", *Inverse Problems*, Vol.15, pp: R41-R93, (1999)

Arridge, S. R., and J. C. Schotland, "Optical tomography: forward and inverse problems", *Inverse Problems*, Vol.25, pp: 123010-123068, (2009)

Atlan, M., B. C. Forget, and A. C. Boccara, "Pulsed acousto-optic imaging in dynamic scattering media with heterodyne parallel speckle detection", *Optics Letters*, Vol.30, pp: 1360-1362, (2005)

Atlan, M., F. Ramaz, B. C. Forget, and A. C. Boccara, Acousto-optic imaging techniques in optically scattered media: towards tumors detection, in *World Conference on Ultrasonics*, Paris, 2003.

Bailey, M. R., L. N. Couret, O. A. Sapozhniko, B. A. Khokhlova, G. R. ter Haar, S. Vaezy, X. Shi, R. Martin, and L. A. Crum, "Use of overpressure to assess the role of bubbles in focused ultrasound lesion shape in vitro", *Ultrasound in Medicine and Biology*, Vol.27, pp: 695-708, (2001)

Bal, G., "Inverse transport theory and applications", *Inverse Problems*, Vol.25, pp: 053001, (2009)

Bal, G., and J. C. Schotland, "Inverse scattering and acousto-optic imaging", *Physical Review Letters*, Vol.104, pp: 043902, (2010)

Ben-David, M., R. Cantor, N. Balbul, M. Yehuda, and I. Gannot, "Measuring tissue heat penetration by scattered light measurements", *Lasers in Surgery and Medicine*, Vol.40, pp: 494-499, (2008)

Berg, W. A., C. I. Campassi, and O. B. Ioffe, "Cystic lesions of the breast: sonographic-pathologic correlation", *Radiology*, Vol.227, pp: 183-191, (2003) Betzig, E., J. K. Trautman, T. D. Harris, J. S. Weiner, and R. L. Kostelak, "Breaking the Diffraction Barrier: Optical Microscopy on a Nanometric Scale", *Science*, Vol.251, pp: 1468-1470, (1991)

Black, J. F., and J. K. Barton, "Chemical and structural changes in blood undergoing laser photocoagulation", *Photochemistry and Photobiology*, Vol.80, pp: 89-97, (2004)

Blonigen, F. J., A. Nieva, C. A. DiMarzio, S. Manneville, L. Sui, G. Maguluri, T. W. Murray, and R. A. Roy, "Computations of the acoustically induced phase shifts of optical paths in acoustophotonic imaging with photorefractive-based detection", *Applied Optics*, Vol.44, pp: 3735-3746, (2005)

Bluestone, A., G. Abdoulaev, C. Schmitz, R. Barbour, and A. Hielscher, "Three-dimensional optical tomography of hemodynamics in the human head", *Optics Express*, Vol.9, pp: 272-286, (2001)

Boas, D. A., D. H. Brooks, E. L. Miller, C. A. Dimarzio, M. Kilmer, R. J. Gaudette, and Q. Zhang, "Imaging the body with diffuse optical tomography", *IEEE Signal Processing Magazine*, Vol.18, pp: 57-75, (2001)

Bossy, E., A. R. Funke, K. Daoudi, and A. C. Boccara, "Transient optoelastography in optically diffusive media", *Applied Physics Letters*, Vol.90, pp: 174111, (2007)

Bossy, E., L. Sui, T. W. Murray, and R. A. Roy, "Combination of ultrasound and acousto-optical imaging using a pulsed-ultrasound scanner", *Proceedings of SPIE*, Vol.5697, pp: 145-153, (2005)

Bossy, E., L. Sui, T. W. Murray, and R. A. Roy, "Fusion of conventional ultrasound imaging and acousto-optic sensing by use of a standard pulsed-ultrasound scanner", *Optics Letters*, Vol.30, pp: 744-746, (2005)

"Breast cancer: Early detection and prompt treatment are critical", *Mayo Clinical Health Letter (Supplement)*, pp: 1-8, (2001)

Brooksby, G. W., and C. M. Penny, "Measurement of ultrasonically modulated scattered light for imaging in turbid media", *Proceedings of SPIE*, Vol.2389, pp: 564-570, (1995)

Cannestra, A. F., S. Y. Bookheimer, N. Pouratian, A. O'Farrell, N. Sicotte, N. A. Martin, D. Becker, G. Rubino, and A. W. Toga, "Temporal and topographical characterization of language cortices using intraoperative optical intrinsic signals", *Neuroimage*, Vol.12, pp: 41-54, (2000)

Cassarly, W., "Taming Light", *SPIE's OE Magazine*, December, pp: 16-18, (2002) Chan, A. H., V. Y. Fujimoto, D. E. Moore, R. W. Martin, and S. Vaezy, "An image-guided high intensity focused ultrasound device for uterine fibroids treatment", *Medical Physics*, Vol.29, pp: 2611-2620, (2002)

Chance, B., S. Nioka, J. Zhang, E. F. Conant, E. Hwang, S. Briest, S. G. Orel, M. D. Schnall, and B. J. Czernicki, "Breast Cancer Detection Based on Incremental Biochemical and Physiological Properties of Breast Cancers: A Six-Year, Two-Site Study", *Academic Radiology*, Vol.12, pp: 925-933, (2005)

Chandrasekhar, R., *Radiation Transfer*. Oxford: Clarendon, (1950)

Cilesiz, I. F., and A. J. Welch, "Light dosimetry: effects of dehydration and thermal damage on the optical properties of the human aorta", *Applied Optics*, Vol.32, pp: 477-487, (1993)

Cline, H. E., J. F. Schenck, R. D. Watkins, K. Hynynen, and F. A. Jolesz, "Magnetic resonance-guided thermal surgery", *Magnetic Resonance in Medicine*, Vol.30, pp: 98-106, (1993)

Colak, S. B., M. B. van der Mark, G. W. Hooft, J. H. Hoogenraad, E. S. van der Linden, and F. A. Kujipers, "Clinical optical tomography and NIR spectroscopy for breast cancer detection", *IEEE Journal of Selected Topics in Quantum Electronics*, Vol.5, pp: 1143-1158, (1999)

Contini, D., F. Martelli, and G. Zaccanti, "Photon migration through a turbid slab described by a mode based on diffusion approximation: I. Theory", *Applied Optics*, Vol.36, pp: 4587-4599, (1997)

Coussios, C., C. H. Farny, G. T. Haar, and R. A. Roy, "Role of acoustic cavitation in the delivery and monitoring of cancer treatment by high-intensity focused ultrasound (HIFU)", *International Journal of Hyperthermia*, Vol.23, pp: 105-120, (2007)

Cubeddu, R., A. Pifferi, P. Taroni, A. Torricelli, and G. Valentini, "Noninvasive absorption and scattering spectroscopy of bulk diffusive media: An application to the optical characterization of human breast", *Applied Physics Letters*, Vol.74, pp: 874-876, (1999)

Cummings, M., D. Wright, and C. Furnival, "The feasibility of retrospective grading of breast cancer histology slides derived from multiple pathology services", *Breast*, Vol.4, pp: 179-182, (1995)

Dang, C. M., K. Zaghiyan, S. R. Karlan, and E. H. Phillips, "Increased use of MRI for breast cancer surveillance and staging is not associated with increased rate of mastectomy", *The American Journal of Surgery*, Vol.75, pp: 937-940, (2009) Daoudi, K., A. C. Boccara, and E. Bossy, "Detection and discrimination of optical absorption and shear stiffness at depth in tissue-mimicking phantom by transient optoelastography", *Applied Physics Letters*, Vol.94, pp: 154103, (2009)

Delaye, P., L.A. Montmorillon, and G. Roosen, "Transmission of time modulated optical signals through an absorbing photorefractive crystal", *Optics Communications,* Vol.118, pp: 154-164, (1995)

Delaye, P., A. Blouin, D. Drolet, L.A. Montmorillon, G. Roosen, and J.P. Monchalin, "Detection of ultrasonic motion of a scattering surface by photorefractive InP:Fe under an applied dc field", *Journal of the Optical Society of America B,* Vol.14, pp: 1723-1734, (1997)

Demos, S. G., A. J. Vogel, and A. H. Gandjbakhche, "Advances in optical spectroscopy and imaging of breast lesions", *Journal of Mammary Gland Biology and Neoplasia*, Vol. 11, pp: 165-181, (2006)

Dewhirst, M. W., B. L. Viglianti, M. Lora-Michiels, M. Hanson, and P. J. Hoopes, "Basic principles of thermal dosimetry and thermal thresholds for tissue damage from hyperthermia", *International Journal of Hyperthermia*, Vol.19, pp: 267-294, (2003)

Dolfi, D., and F. Micheron, "Imaging process and system for transillumination with photon frequency marking", in *International Patent WO 89/00278*, (1989)

Duck, F. A., *Physical properties of tissue: a comprehensive reference book*. Academic, (1990)

Farny, C. H., R. G. Holt, and R. A. Roy, "Temporal and spatial dependence of HIFU-induced inertial and hot-vapor cavitation with a diagnostic ultrasound system", *Ultrasound in Medicine and Biology*, Vol.35, pp: 603-615, (2009)

Fercher, A. F., W. Drexler, C. K. Hitzenberger, and T. Lasser, "Optical coherence tomography- principles and applications", *Reports on Progress in Physics*, Vol.66, pp: 239-303, (2003)

Fishkin, J. B., O. Coquoz, E. R. Anderson, B. M., and T. B. J., "Frequency-domain photon migration measurements of normal and malignant tissue optical properties in a human subject", *Applied Optics*, Vol.36, pp: 10-20, (1997)

Flobbe, K., P. J. Nelemans, A. G. H. Kessels, A. G. H. Beets, M. F. von Meyenfeldt, and J. M. A. van Engelshoven, "The role of ultrasonography as an adjunct to mammography in the detection of breast cancer: a systematic review", *European Journal of Cancer*, Vol.38, pp: 1044-1050, (2002) Forget, B. C., F. Ramaz, M. Atlan, J. Selb, and A. C. Boccara, "High-contrast fast Fourier transform acousto-optical tomography of phantom tissues with a frequency-chirp modulation of the ultrasound", *Applied Optics*, Vol.42, pp: 1379-1383, (2003)

Furusawa, H., K. Namba, S. Thomsen, F. Akiyama, A. Bendet, C. Tanaka, Y. Yasuda, and H. Nakahara, "Magnetic resonance-guided focused ultrasound surgery of breast cancer: reliability and effectiveness", *Journal of the American College of Surgeons*, Vol.203, pp: 54-63, (2006)

Gelet, A., J. Y. Chapelon, R. Bouvier, O. Rouviere, Y. Lasne, D. Lyonnet, and J. M. Dubernard, "Transrectal high-intensity focused ultrasound: minimally invasive therapy of localized prostate cancer", *Journal of Endourology*, Vol.14, pp: 519-528, (2000)

Gianfelice, D., M. Amara, A. Belblidia, and Y. Boulanger, "MR Imaging–guided Focused US Ablation of Breast Cancer: Histopathologic Assessment of Effectiveness—Initial Experience", *Radiology*, Vol.227, pp: 849-855, (2003)

Gianfelice, D., A. Khiat, Y. Boulanger, M. Amara, and A. Belblidia, "Feasibility of magnetic resonance imaging-guided focused ultrasound surgery as an adjunct to tamoxifen therapy in high-risk surgical patients with breast carcinoma", *Journal of Vascular and Interventional Radiology*, Vol.14, pp: 1275-1282, (2003)

Gladkova, N. D. K., G. A. Petrova, N. Nikulin, S. G. Radenska-Lopvok, L. B. Snopova, Y. P. Chumakov, V. A. Nasonova, V. M. Gelikonov, G. V. Gelikonov, R. V. Kuranov, A. M. Sergeev, and F. I. Feldchtein, "In vivo optical coherence tomography imaging of human skin: norm and pathology", *Skin Research and Technology*, Vol.6, pp: 6-16, (2001)

Granot, E., A. Lev, Z. Kotler, and B. G. Sfez, "Detection of inhomogeneities with ultrasound tagging of light", *Journal of the Optical Society of America A*, Vol.18, pp: 1962-1967, (2001)

Gross, M., P. Goy, and M. Al-Koussa, "Shot-noise detection of ultrasound-tagged photons in ultrasound-modulated optical imaging", *Optics Letters*, Vol.28, pp: 2482-2484, (2003)

Gross, M., M. Lesaffre, F. Ramaz, P. Delaye, G. Roosen, and A. C. Boccara, "Detection of the tagged or untagged photons in acousto-optic imaging of thick scattering media by photorefractive adaptive holography", *The European Physical Journal E*, Vol.28, pp: 173-182, (2009) Gross, M., F. Ramaz, B. C. Forget, M. Atlan, A. C. Boccara, P. Delaye, and G. Roosen, "Theoretical description of the photorefractive detection of the ultrasound modulated photons in scattering media", *Optics Express*, Vol.13, pp: 7097-7112, (2005)

Hale, G. M., and M. R. Querry, "Optical constants of water in the 200 nm to 200 μm wavelength region", *Applied Optics*, Vol.12, pp: 555-563, (1973)

Hale, T. C., and K. Telschow, "Optical lock-in detection using photorefractive frequency domain processing", *Applied Physics Letters*, Vol.69, pp: 2632-2634, (1996)

Harper, A. P., E. Kelly-Fry, and J. S. Noe, "Ultrasound breast imaging- the method of choice for examining the young patient", *Ultrasound in Medicine and Biology*, Vol.7, pp: 231-237, (1981)

Heffer, E. L., and S. Fantini, "Quantitative oximetry of breast tumors: a near-infrared method that indentifies two optimal wavelengths for each tumor", *Applied Optics*, Vol.41, pp: 3827-3939, (2002)

Hill, C. R., J. C. Bamber, and G. R. ter Haar, *Physical Principles of Medical Ultrasonics*. Chichester, UK: John Wiley & Sons, Ltd, (2004)

Hill, C. R., and G. R. ter Haar, "High intensity focused ultrasound- potential for cancer treatment (Review article)", *British Journal of Radiology,* Vol.68, pp: 1296-1303, (1995)

Hindle, W. H., L. Davis, and D. Wright, "Clinical value of mammography for symptomatic women 35 years of age and younger", *American Journal of Obstetrics and Gynecology*, Vol.180, pp: 1484-1490, (1999)

Huang, D., E. A. Swanson, C. P. Lin, J. S. Schuman, W. G. Stinson, W. Chang, M. R. Hee, T. Flotte, K. Gregory, C. Puliafito, A., and J. G. Fujimoto, "Optical coherence tomography", *Science,* Vol.254, pp: 1178-1181, (1991)

Hughes, L. E., R. E. Mansel, and D. J. T. Webster, *Benign disorders and diseases of the breast*. London: Balliere Tindall, (1989)

Hurd, T. C., and S. B. Edge, "Breast cancer imaging", *Surgical Oncology Clinics of North America*, Vol.8, pp: 1-15, (1999)

Hynynen, K., W. R. Freund, H. E. Cline, C. A. H., R. D. Watkins, J. P. Vetro, and F. A. Jolesz, "A clinical, noninvasive, MR imaging-monitored ultrasound surgery method", *Radiographics*, Vol.16, pp: 185-195, (1996) Illing, R., and A. Chapman, "The clinical applications of high intensity focused ultrasound in the prostate", *International Journal of Hyperthermia*, Vol.23, pp: 183-191, (2007)

Institute of Medicine, "Mammography and Beyond", National Academy Press, (2001)

Ishimaru, A., *Single scattering and transport theory (Wave propagation and scattering in random media 1)*. New York: Academic Press, (1978)

Jackson, V. P., "The current role of ultrasonography in breast imaging", *Radiological Clinics of North Amerca*, Vol.33, pp: 1161-1170, (1995)

Jackson, V. P., H. E. Reynolds, and D. R. Hawes, "Sonography of the breast", *Seminars in Ultrasound, CT and MRI*, Vol.17, pp: 460-475, (1996)

Kempe, M., M. Larionov, D. Zaslavsky, and A. Z. Genack, "Acousto-optic tomography with multiply scattered light", *Journal of the Optical Society of America A*, Vol.14, pp: 1151-1158, (1997)

Kennedy, J. E., "High-intensity focused ultrasound in the treatment of solid tumours", *Nature Reviews. Cancer*, Vol.5, pp: 321-327, (2005)

Kennedy, J. E., F. Wu, G. R. ter Haar, F. V. Gleeson, R. R. Phillips, M. R. Middleton, and D. Cranston, "High-intensity focused ultrasound for the treatment of liver tumors", *Ultrasonics*, Vol.42, pp: 931-935, (2004)

Khokhlova, T. D., M. S. Canney, D. Lee, K. I. Marro, L. A. Crum, V. A. Khokhlova, and M. R. Bailey, "Magnetic resonance imaging of boiling induced by high intensity focused ultrasound", *Journal of the Acoustical Society of America*, Vol.125, pp: 2420-2431, (2009)

Khokhlova, T. D., I. M. Pelivanov, O. A. Sapozhniko, V. S. Solomatin, and A. A. Karabutov, "Opto-acoustic diagnostics of the thermal action of high-intensity focused ultrasound on biological tissues: the possibility of its applications and model experiments", *Quantum Electronics*, Vol.36, pp: 1097-1102, (2006)

Khosrofian, J. M., and B. A. Garetz, "Measurement of a Gaussian laser beam diameter through the direct inversion of knife-edge data", *Applied Optics*, Vol.22, pp: 3406-3410, (1983)

Kim, C., K. H. Song, and L. V. Wang, "Sentinel lymph node detection ex vivo using ultrasound-modulated optical tomography", *Journal of Biomedical Optics*, Vol.13, pp: 020507, (2008) Kim, C., and L. V. Wang, "Multi-optical-wavelength ultrasound-modulated optical tomography: a phantom study", *Optics Letters*, Vol.32, pp: 2285-2287, (2007)

Kim, C., R. J. Zemp, and L. V. Wang, "Intense acoustic bursts as a signal-enhancement mechanism in ultrasound-modulated optical tomography", *Optics Letters*, Vol.31, pp: 2423-2425, (2006)

Kim, D. Y., W. K. Moon, N. Cho, E. S. Ko, S. K. Yang, J. S. Park, S. M. Kim, I. A. Park, J. H. Cha, and E. H. Lee, "MRI of the breast for the detection and assessment of the size of ductal carcinoma in situ", *Korean Journal of Radiology*, Vol.8, pp: 32-29, (2007)

Kneeshaw, P. J., L. W. Turnbulll, and P. J. Drew, "Current applications and future direction of MR mammography", *British Journal of Cancer*, Vol.88, pp: 4-10, (2003)

Kohrman, K. U., M. S. Michel, J. Gaa, E. Marlinghaus, and P. Alken, "High intensify focused ultrasound as noninvasive therapy for mutilocal renal cell carcinoma: case study and review of the literature", *Journal of Urology*, Vol.167, pp: 2397-2403, (2002)

Kolb, T. M., J. Lichy, and J. H. Newhouse, "Comparison of the performance of screening mammography, physical examination, and breast US and evaluation of factors that influence them: an analysis of 27,825 patient evaluations", *Radiology*, Vol.225, pp: 165-175, (2002)

Konofagou, E. E., J. Thierman, and K. Hynynen, "The use of ultrasound-stimulated acoustic emission in the monitoring of modulus changes with temperature", *Ultrasonics*, Vol.41, pp: 337-345, (2003)

Kopans, D. B., *Breast Imaging*. Lippincott-Raven Philadelphia and New York, (1998)

Kopans, D. B., "Breast-cancer screening with ultrasonography", *Lancet*, Vol.354, pp: 2096-2097, (1999)

Kopelman, D., Y. Inbar, A. Hanannel, D. Freundlich, D. Castel, A. Perel, A. Greenfeld, T. Salamon, M. Sareli, A. Valeanu, and M. Papa, "Magnetic resonance-guided focused ultrasound surgery (MRgFUS): Ablation of liver tissue in a porcine model", *European Journal of Radiology*, Vol.59, pp: 157-162, (2006)

Kothapalli, S.-R., S. Sakadzic, C. Kim, and L. V. Wang, "Imaging optically scattering objects with ultrasound-modulated optical tomography", *Optics Letters*, Vol.32, pp: 2351-2353, (2007) Kothapalli, S.-R., and L. Wang, "Ex vivo blood vessel imaging using ultrasound-modulated optical microscopy", *Journal of Biomedical Optics*, Vol.14, pp: 014015-014011, (2009)

Kothapalli, S.-R., and L. V. Wang, "Ultrasound-modulated optical microscopy", *Journal of Biomedical Optics*, Vol.13, pp: 054046, (2008)

Kou, L., D. Labrie, and P. Chylek, "Refractive indices of water and ice in the 0.65-2.5 um spectral range", *Applied Optics*, Vol.32, pp: 3531-3540, (1993)

Ku, G., G. Yao, and L. V. Wang, "Chirped ultrasound-modulated optical tomography", *Proceedings of SPIE*, Vol.3597, pp: 371-375, (1999)

Lai, P., R. A. Roy, and T. W. Murray, "Quantitative characterization of turbid medium using pressure contrast acousto-optic imaging", *Optics Letters*, Vol.34, pp: 2850-2852, (2009)

Lai, P., R. A. Roy, and T. W. Murray, "Sensing the optical properties of diffusive media by acousto-optic pressure contrast imaging", *Proceedings of SPIE*, Vol.7177, pp: 71771G, (2009)

Lai, P., J. R. McLaughlan, A. B. Draudt, T. W. Murray, R. O. Cleveland, and R. A. Roy, "Monitoring and guidance of high intensity focused ultrasound exposures in real time using acousto-optic imaging: feasibility and demonstration *ex vivo*", *Proceedings of SPIE*, Vol.7564, pp: 75642B, (2010)

Leff, D. R., O. Warren, L. C. Enfield, A. P. Gibson, T. Athanasiou, D. K. Pattern, J. C. Hebden, G. Z. Yang, and A. Darzi, "Diffuse optical imaging of the healthy and diseased breast: a systematic review", *Breast Cancer Research and Treatment*, Vol.108, pp: 9-22, (2007)

Lehman, C. D., and M. D. Schnall, "Imaging in breast cancer: magnetic resonance imaging", *Breast Cancer Research*, Vol.7, pp: 215-219, (2005)

Leighton, T. G., *The Acoustic Bubble*. San Diego, CA: Academic Press, Inc., (1997)

Lerner, J. M., and A. Thevenon, *The Optics of Spectroscopy* (2010), http://www.horiba.com/us/en/scientific/products/optics-tutorial//?Ovly=1

Lesaffre, M., F. Jean, F. Ramaz, A. C. Boccara, M. Gross, and G. Roosen, "In situ monitor of the photorefractive time-response in a self-adaptive wavefront holography setup developed for acousto-optic imaging", *Optics Express*, Vol.15, pp: 1030-1042, (2007) Leutz, W., and G. Maret, "Ultrasonic modulation of multiply scattered light", *Physica B*, Vol.204, pp: 14-19, (1995)

Lev, A., Z. Kotler, and B. G. Sfez, "Ultrasound tagged light imaging in turbid media in reflectance geometry", *Optics Letters*, Vol.25, pp: 378-380, (2000)

Leveqe-Fort, S., "Three-dimensional acousto-optic imaging in biological tissues with parallel signal processing", *Applied Optics*, Vol.40, pp: 1029-1036, (2000)

Leveqe-Fort, S., A. C. Boccara, M. Lebec, and H. Saint-Jalmes, "Ultrasonic tagging of photon paths in scattering media: parallel speckle modulation processing", *Optics Letters*, Vol.24, pp: 181-183, (1999)

Lewa, C. J., "Magnetic-resonance-imaging in the presence of mechanical waves", *Spectroscopy Letters*, Vol.24, pp: 55-67, (1991)

Li, A., E. L. Miller, M. E. Kilmer, T. J. Brukilacchio, T. Chaves, J. Stott, Q. Zhang, T. Wu, M. Chorlton, R. H. Moore, D. B. Kopans, and D. A. Boas, "Tomographic optical breast imaging guided by three-dimensional mammography", *Applied Optics*, Vol.42, pp: 5181-5190, (2003)

Li, C., and L. V. Wang, "Photoacoustic tomography and sensing in biomedicine", *Physics in Medicine and Biology*, Vol.54, pp: R59-R97, (2009)

Li, F., R. Feng, Q. Zhang, J. Bai, and Z. Wang, "Estimation of HIFU induced lesions in vitro: numerical simulation and experiment", *Ultrasonics*, Vol.44, pp: e337-e340, (2006)

Li, J., G. Ku, and L. V. Wang, "Ultrasound-modulated optical tomography of biological tissue by use of contrast of laser speckles", *Applied Optics*, Vol.41, pp: 6030-6035, (2002)

Li, J., S. Sakadzic, G. Ku, and L. V. Wang, "Transmission- and side-detection configurations in ultrasound-modulated optical tomography of thick biological tissues", *Applied Optics*, Vol.42, pp: 4088-4094, (2003)

Li, J., and L. V. Wang, "Methods for parallel-detection-based ultrasound-modulated optical tomography", *Applied Optics*, Vol.41, pp: 2079-2084, (2002)

Li, J., and L. V. Wang, "Ultrasound-modulated optical computed tomography of biological tissues", *Applied Physics Letters*, Vol.84, pp: 1597-1599, (2004) Li, Y., P. Hemmer, C. Kim, H. Zhang, and L. V. Wang, "Detection of ultrasound-modulated diffuse photons using spectral hole burning", *Optics Express*, Vol.16, pp: 14862-14874, (2008)

Li, Y., H. Zhang, C. Kim, K. H. Wagner, P. Hemmer, and L. V. Wang, "Pulsed ultrasound-modulated optical tomography using spectral-hole burning as a narrowband spectral filter", *Applied Physics Letters*, Vol.93, pp: 011111, (2008)

Lizzi, F. L., R. Muratore, C. X. Deng, J. A. Kettering, S. K. Alam, M. S., and A. Kalisz, "Radiation-force technique to monitor lesions during ultrasonic therapy", *Ultrasound in Medicine and Biology*, Vol.29, pp: 1593-1605, (2003)

Luechniger, R., F. Duru, R. Candinas, and P. Boesiger, "Safety considerations for magnetic resonance imaging of pacemaker and ICD patients", *Herzschrittmachertherapie und Elektrophysiologie*, Vol.15, pp: 73-81, (2004)

Lynn, J. G., R. L. Zwemer, A. J. Chick, and A. E. Millar, "A new method for the generation and use of focused ultrasound in experimental biology", *Journal of General Physiology*, Vol.26, pp: 179-193, (1942)

Mahan, G. D., W. E. Engler, J. J. Tiemann, and E. Uzgiris, "Ultrasonic tagging of light: Theory", *Proceedings of the National Academy of Sciences USA*, Vol.99, pp: 1415-1419, (1998)

Maleke, C., and E. E. Konofagou, "Harmonic motion imaging for focused ultrasound (HMOFU): a fully integrated technique for sonication and monitoring of thermal ablation in tissues", *Physics in Medicine and Biology*, Vol.53, pp: 1773-1793, (2008)

Marcotte-Bloch, C., C. Balu-Maestro, E. Chamorey, F. Ettore, I. Raoust, B. Flipo, and C. Chapellier, "MRI for the size assessment of pure ductal carcinoma in situ (DCIS): A prospective study of 33 patients", *European Journal of Radiology* (in press)

Marks, F. A., H. W. Tomlinson, and G. W. Brooksby, "A comprehensive approach to breast cancer detection using light: photon localization by ultrasound modulation and tissue characterization by spectral discrimination", *Proceedings of SPIE*, Vol.1888, pp: 500-510, (1993)

McDannold, N., K. Hynynen, D. Wolf, G. Wolf, and F. A. Jolesz, "MRI evaluation of thermal ablation of tumors with focused ultrasound", *Journal of Magnetic Resonance Imaging*, Vol.8, pp: 91-100, (1998)

McLaughlan, J. R., "An investigation into the use of cavitation for the optimisation of high intensity focused ultrasound (HIFU) treatments". Doctor of Philosophy in

Physics, London: University of London, Joint Department of Physics, Institute of Cancer Research and Royal Marsden NHS Trust, (2008)

Meaney, P. M., M. D. Cahill, and G. R. ter Haar, "The intensity dependence of lesion position shift during focused ultrasound surgery", *Ultrasound in Medicine and Biology*, Vol.26, pp: 441-450, (2000)

Meaney, P. M., R. L. Clarke, G. R. ter Haar, and I. H. Rivens, "A 3-D finite-element model for computation of temperature profiles and regions of thermal damage during focused ultrasound surgery exposures", *Ultrasound in Medicine and Biology*, Vol.24, pp: 1489-1499, (1998)

Millerd, J. E., M. Ziari, and A. Partovi, Photorefractive in semiconductors. Academic Press, (1999)

Mishchenko, M. I., J. W. Hovenier, and L. D. Travis, eds., Light scattering by nonspherical particles. San Diego: Academic Press, (2000)

Mourant, J. R., J. P. Freyer, A. H. Hielscher, A. A. Eick, D. Shen, and T. M. Johnson, "Mechanisms of light scattering from biological cells relevant to noninvasive optical-tissue diagnosis", *Applied Optics*, Vol.37, pp: 3586-3593, (1998)

Mourant, J. R., T. Fuselier, J. Boyer, T. M. Johnson, and I. J. Bigio, "Predictions and measurements of scattering and absorption over broad wavelength ranges in tissue phantoms", *Applied Optics*, Vol.36, pp: 949-957, (1997)

Murray, T. W., and R. A. Roy, "Illuminating Sound: Imaging Tissue Optical Properties with Ultrasound", *Acoustics Today*, Vol.3, pp: 17-23, (2007)

Murray, T. W., L. Sui, G. Maguluri, R. A. Roy, A. Nieva, F. J. Blonigen, and C. A. DiMarzio, "Detection of ultrasound-modulated photons in diffuse media using the photorefractive effect", *Optics Letters*, Vol.29, pp: 2509-2511, (2004)

National Cancer Institute, "Fact Sheet: Improving methods for breast cancer detection and diagnosis", (2002)

National Cancer Institute, "Mammograms", (2009)

Neighbors, T. H., and W. G. Mayer, "Asymmetric light diffraction by pulsed ultrasonic waves", *Journal of the Acoustical Society of America*, Vol.74, pp: 146, (1983)

Ng, K. Y., and Y. Liu, "Therapeutic ultrasound: its application in drug delivery", *Medicinal Research Reviews*, Vol.22, pp: 204-223, (2002) Nilsson, A. M. K., C. Sturesson, D. L. Liu, and S. Andersson-Engels, "Changes in spectral shape of tissue optical properties in conjunction with laser-induced thermotherapy", *Applied Optics*, Vol.37, pp: 1256-1267, (1998)

Nziachristos, V., and B. Chance, "Probing physiology and molecular function using optical imaging: applications to breast cancer", *Breast Cancer Research*, Vol.3, pp: 41-46, (2001)

Nziachristos, V., A. G. Yodh, M. D. Schnall, and B. Chance, "MRI-guided diffuse optical spectroscopy of malignant and benign breast lesions", *Neoplasia*, Vol.4, pp: 347-354, (2002)

Oraevsky, A. A., S. L. Jacques, G. H. Pettit, I. S. Saidi, F. K. Tittel, and P. D. Henry, "Optical properties and energy pathways", *Lasers in Surgery and Medicine*, Vol.12, pp: 585-597, (1992)

Oraevsky, A. A., S. L. Jacques, and F. K. Tittel, "Measurement of tissue optical properties by time-resolved detection of laser-induced transient stress", *Applied Optics*, Vol.36, pp: 402-415, (1997)

Passos, D., J. C. Hebden, P. N. Pinto, and R. Guerra, "Tissue phantom for optical diagnostics based on a suspension of microspheres with a fractal size distribution", *Journal of Biomedical Optics*, Vol.10, pp: 064036, (2005)

Patterson, M. S., B. Chance, and B. C. Wilson, "Time resolved reflectance and transmittance for the noninvasive measurement of tissue optical properties", *Applied Optics*, Vol.28, pp: 2331-2336, (1989)

Peters, N. H., I. H. Borel Rinkes, N. P. Zuithoff, W. P. Mali, K. G. Moons, and P. H. Peters, "Meta-analysis of MR imaging in the diagnosis of breast lesions", *Radiology*, Vol.246, pp: 116-124, (2008)

Pifferi, A., J. Swartling, E. Chikodze, A. Torricelli, P. Taroni, A. Bassi, S. Anderson-Engels, and R. Cubeddu, "Spectroscopy time-resolved diffuse reflectance and transmittance measurements of the female breast at different interfiber distances", *Journal of Biomedical Optics*, Vol.9, pp: 1143-1151, (2004)

Podoleanu, A., J. Rogers, D. Jackson, and S. Dunne, "Three dimensional OCT images from retina and skin", *Optics Express*, Vol.7, pp: 292-298, (2000)

Pogue, B. W., and M. S. Patterson, "Review of tissue simulating phantom for optical spectroscopy, imaging and dosimetry", *Journal of Biomedical Optics*, Vol.11, pp: 041102, (2006) Porter, T. R., and F. Xie, "Therapeutic ultrasound for gene delivery", *Echocardiography*, Vol.18, pp: 349-353, (2001)

Povazay, B., K. Bizheva, A. Unterhuber, B. Herman, H. Sattmann, A. F. Fercher, and W. Drexler, "Submicrometer axial resolution optical coherence tomography", *Optcis Letters*, Vol.27, pp: 1800-1802, (2002)

Prahl, S., *Mie theory model for tissue optical properties*. (1998), http://omlc.ogi.edu/classroom/ece532/class3/mie.html

Prahl, S., *Optical Absorption of Hemoglobin*. (1999), http://omlc.ogi.edu/spectra/hemoglobin/index.html

Prahl, S., *Some biological scatterers*. (2002), http://omlc.ogi.edu/classroom/ece532/class3/scatterers.html

Prahl, S., *Mie Scattering Calculator*. (2007), http://omlc.ogi.edu/calc/mie_calc.html

Quaresima, V., S. J. Matcher, and M. Ferrari, "Identification and quantification of intrinsic optical contrast for near-infrared mammography", *Photochemistry and Photobiology*, Vol.67, pp: 4-14, (1998)

Rabkin, B. A., V. Zderic, L. A. Crum, and S. Vaezy, "Biological and physical mechanisms of HIFU-induced hyperecho in ultrasound image", *Ultrasound in Medicine and Biology*, Vol.32, pp: 1721-1729, (2006)

Rabkin, B. A., V. Zderic, and S. Vaezy, "Hyperecho in ultrasound images of HIFU therapy: involvement of cavitation", *Ultrasound in Medicine and Biology*, Vol.31, pp: 947-956, (2005)

Ramaz, F., B. C. Forget, M. Atlan, and A. C. Boccara, "Photorefractive detection of tagged photons in ultrasound modulated optical tomography of thick biological tissues", *Optics Express*, Vol.12, pp: 5469-5474, (2004)

Rice, A., and C. M. Quinn, "Angiogenesis, thrombospodin, and ductal carcinoma in situ of the breast", *Journal of Clinical Pathology*, Vol.55, pp: 569-574, (2002)

Rivens, I., A. Shaw, J. Civale, and H. Morris, "Treatment monitoring and thermometry for therapeutic focused ultrasound", *International Journal of Hyperthermia*, Vol.23, pp: 121-139, (2007)

Rosenschein, U., V. Furman, E. Kerner, I. Fabian, J. Bernheim, and Y. Eshel, "Ultrasound Imaging–Guided Noninvasive Ultrasound Thrombolysis : Preclinical Results", *Circulation*, Vol.102, pp: 238-245, (2000) Rousseau, G., A. Blouin, and J.-P. Monchalin, "Ultrasound-modulated optical imaging using a powerful long pulse laser", *Optics Express*, Vol.16, pp: 12577-12590, (2008)

Rousseau, G., A. Blouin, and J.-P. Monchalin, "Ultrasound-modulated optical imaging using a high-power pulsed laser and a double-pass confocal Fabry-Perot interferometer", *Optics Letters*, Vol.34, pp: 3445-3447, (2009)

Sakadzic, S., and L. V. Wang, "Ultrasound modulation of multiply scattered coherent light: An analytical model for anisotropically scattering media", *Physics Review E*, Vol.66, pp: 026603, (2002)

Sakadzic, S., and L. V. Wang, "High resolution ultrasound-modulated optical tomography in biological tissues", *Optics Letters*, Vol.29, pp: 2770-2772, (2004)

Sakadzic, S., and L. V. Wang, "Modulation of multiply scattered coherent light by ultrasound pulses: An analytical model", *Physics Review E*, Vol.72, pp: 033620, (2005)

Saleh, B. E. A., and M. C. Teich, *Fundamental of Photonics*. New York: John Wiley & Sons, Inc., (1991)

Saslow, D., C. Boetes, W. Burke, S. Harms, M. O. Leach, and L. C. D., "American Cancer Society guidelines for breast screening with MRI as an adjunct to mammography", *CA: A Cancer Journal for Clinicians*, Vol.57, pp: 75-89, (2007)

Sathyam, U. S., and S. Prahl, "Limitations in measurements of subsurface temperatures using pulsed photothermal radiometry", *Journal of Biomedical Optics*, Vol.2, pp: 251-261, (1997)

Selb, J., D. K. Joseph, and D. A. Boas, "Time-gated optical system for depth-resolved functional brain imaging", *Journal of Biomedical Optics*, Vol.11, pp: 044008, (2006)

Selb, J., S. Leveqe-Fort, L. Potter, and A. C. Boccara, "3D acousto-optic modulated-speckle imaging in biological tissues", *Comptes Rendus de I'Academie des Sciences-Series IV- Physics*, Vol.2, pp: 1213-1225, Paris, France (2001)

Selb, J., L. Potter, and A. C. Boccara, "Nonlinear effects in acousto-optic imaging", *Optics Letters*, Vol.27, pp: 918-920, (2002)

Siegel, D. A., and A. J. Plueddemann, "The motion of a solid sphere in an oscillating flow: an evaluation of remotely sensed doppler velocity estimates in the sea", *Journal of Atmospheric and Oceanic Technology*, Vol.8, pp: 296, (1991) Smith, J. A., and E. Andreopoulou, "An overview of the status of imaging screening technology for breast cancer", *Annals of Oncology*, Vol.15 (supplement 1), pp: i18-i26, (2004)

Solymar, L., D. J. Webb, and A. G. Jepsen, *The physics and applications of photorefractive materials.* Oxford: Clarendon Press, (1996)

Squire, L. F., and R. A. Novelline, *Squire's fundamentals of radiology*. Cambridge: Harvard University Press, (1997)

Srinivasan, V. J., R. Huber, I. Gorczynska, J. G. Fujimoto, J. Y. Jiang, P. Reisen, and A. E. Cable, "High-speed, high-resolution optical coherence tomography retinal imaging with a frequency-swept laser at 850 nm", *Optics Letters*, Vol.32, pp: 361-363, (2007)

Stavros, A. T., D. Thickman, C. L. Rapp, M. A. Dennis, S. H. Parker, and G. A. Sisney, "Solid breast nodules: use of sonography to distinguish between benign and malignant lesions", *Radiology*, Vol.196, pp: 123-134, (1995)

Stewart, E. A., W. M. W. Gedroyc, C. M. C. Tempany, B. J. Quade, Y. Inbar, T. Ehrenstein, A. Shushan, J. T. Hindley, R. D. Goldin, M. David, M. Sklair, and J. Rabinovici, "Focused ultrasound treatment of uterine fibroid tumors: Safety and feasibility of a noninvasive thermoablative technique ", *American Journal of Obstetrics and Gynecology*, Vol.189, pp: 48-54, (2003)

Stott, J. J., D. J. Townsend, M. Kashamabala, R. A. Roy, and C. A. Dimarzio, "Interactions mechanisms in acousto-photonic imaging", *Proceedings of SPIE*, Vol.4129, pp: 426-430, (2000)

Sui, L., "Acousto-optic Imaging in Diffuse Media Using Pulsed Ultrasound and The Photorefractive Effect". Doctor of Philosophy in Mechanical Engineering, Boston: Boston University, Department of Aerospace and Mechanical Engineering, (2005)

Sui, L., T. W. Murray, and R. A. Roy, "The combination of pulsed acousto-optic imaging and B-mode diagnostic ultrasound for three-dimensional imaging in *ex vivo* biological tissue", *Proceedings of SPIE*, Vol.6086, pp: 60861B, (2006)

Sui, L., R. A. Roy, C. A. Dimarzio, and T. W. Murray, "Imaging in diffuse media with pulsed-ultrasound-modulated light and the photorefractive effect", *Applied Optics*, Vol.44, pp: 4041-4048, (2005)

Tempany, C. M., E. A. Stewart, N. McDannold, B. J. Quade, F. A. Jolesz, and K. Hynynen, "MR imaging-guided focused ultrasound surgery of uterine leiomyomas: A feasibility study", *Radiology*, Vol.226, pp: 897-905, (2003) ter Haar, G. R., "Ultrasound focal beam surgery", *Ultrasound in Medicine and Biology*, Vol.21, pp: 1089-1100, (1995)

ter Haar, G. R., D. Sinnett, and I. Rivens, "High intensity focused ultrasound - a surgical technique for treatment of discrete liver tumors", *Physics in Medicine and Biology*, Vol.34, pp: 1743-1750, (1989)

Thomsen, S., and D. Tatman, "Physiological and pathological factors of human breast disease that can influence optical diagnosis", *Annals of the New York Academy of Sciences*, Vol.838, pp: 171-193, (1998)

Thuroff, S., C. Chaussy, G. Vallancien, W. Wieland, H. Kiel, A. le Duc, F. Desgrandchamps, J. J. M. C. H. de la Rosette, and A. Gelet, "High-Intensity Focused Ultrasound and Localized Prostate Cancer: Efficacy Results from the European Multicentric Study", *Journal of Endourology*, Vol.17, pp: 673-677, (2003)

Tomlinson, H. W., and J. J. Tiemann, "Ultrasonic tagging for light imaging in a scattering medium", *Patent Disclosure Letter, General Electric Corporate Research and Development Center*, (1992)

Tuchin, V. V., ed. Handbook of Optical Biomedical Diagnosis. SPIE, Washington, (2002)

Uchida, T., N. T. Sanghvi, T. A. Gardner, M. D. Koch, D. Ishii, S. Minei, T. Satoh, T. Hyodo, A. Irie, and S. Baba, "Transrectal high-intensity focused ultrasound for treatment of patients with stage T1b-2n0m0 localized prostate cancer: a preliminary report", *Urology*, Vol.59, pp: 394-398, (2002)

US Food and Drug Administration, "Information for manufacturers seeking marketing clearance of diagnostic ultrasound systems and transducers", Department of Health and Human Services, Center for Devices and Radiological Health, (1997)

Vaezy, S., R. Martin, H. Yaziji, P. Kaczkowski, G. Keilman, S. Carter, M. Caps, E. Chi, M. R. Bailey, and L. A. Crum, "Hemostasis of punctured blood vessels using high-intensity focused ultrasound", *Ultrasound in Medicine and Biology*, Vol.24, pp: 903-910, (1998)

Vaezy, S., X. Shi, E. C. Martin, N. I. Nelson, M. R. Bailey, and L. A. Crum, "Real-time visualization of high-intensity focused ultrasound treatment using ultrasound imaging", *Ultrasound in Medicine and Biology*, Vol.27, pp: 33-42, (2001)

Vallancien, G., E. Chartier-Kastler, and M. Harouni, "Focused extracorporeal pyrotherapy: experimental study and feasibility in man", *Seminars in Urology*, Vol.11, pp: 7-9, (1993) van Veen, R. L. P., H. J. C. M. Steremborg, A. Pifferi, A. Torricelli, and R. Cubeddu, Determination of VIS-NIR absorption coefficients of mammalian fat, with time- and spatially revolved diffuse reflectance and transmission spectroscopy, in *Biomedical Topical Meetings*, Optical Society of America, Washington, 2004.

Vaupel, P., K. Shlenger, C. Knoop, and M. Hockel, "Oxygenation of human tumors: evaluation of tissue oxygen distribution in breast cancers by computerized O_2 tension measurements", *Cancer Research*, Vol.51, pp: 3316-3322, (1991)

Vaupel, P., O. Thews, D. K. Kelleher, and M. Hoeckel, "Current status of knowledge and critical issues in tumor oxygenation results from 25 years research in tumor pathophysiology", *Advances in Experimental Medicine and Biology*, Vol.454, pp: 591-602, (1998)

Viator, J. A., and S. Prahl, "Photoacoustic imaging of gelatin phantoms using matched filed processing", *Proceedings of SPIE*, Vol.3601, pp: 276-283, (1999)

Wang, L. V., "Ultrasound-modulated optical tomography of dense turbid media", *Proceedings of SPIE*, Vol.2676, pp: 91-102, (1996)

Wang, L. V., "Rapid modeling of diffuse reflectance of light in turbid slabs", *Journal of the Optical Society of America A*, Vol.15, pp: 936-944, (1998)

Wang, L. V., "Ultrasonic modulation of scattered in turbid media and a potential novel tomography in biomedicine", *Photochemistry and Photobiology*, Vol.67, pp: 41-49, (1998)

Wang, L. V., "Mechanisms of ultrasonic modulation of multiply scattered coherent light: a Monte Carlo model", *Optics Letters*, Vol.26, pp: 1191-1193, (2001)

Wang, L. V., "Mechanisms of ultrasound modulation of multiply scattered coherent light: An analytic model", *Physics Review Letters*, Vol.87, pp: 043903, (2001)

Wang, L. V., "Ultrasound-mediated biophotonic imaging: A review of acousto-optical tomography and photo-acoustic tomography", *Disease Markers*, Vol.19, pp: 123-138, (2004)

Wang, L. V., S. L. Jacques, and X. Zhao, "Continuous-wave ultrasonic modulation of scattered laser light to image objects in turbid media", *Optics Letters*, Vol.20, pp: 629-631, (1995)

Wang, L. V., and G. Ku, "Frequency-swept ultrasound-modulate optical tomography of scattering media", *Optics Letters*, Vol.23, pp: 975-977, (1998) Wang, L. V., and X. Zhao, "Ultrasound-modulated optical tomography of absorbing objects buried in dense tissue-simulating turbid media", *Applied Optics*, Vol.36, pp: 7277-7282, (1997)

Wang, W., Y. Wang, and J. Tang, "Safety and efficacy of high intensity focused ultrasound ablation therapy for adenomyosis", *Academic Radiology*, Vol.16, pp: 1416-1423, (2009)

Wang, Z., J. Bai, F. Li, Y. Du, S. Wen, K. Hu, G. Xu, P. Ma, N. Yin, W. Chen, F. Wu, and R. Feng, "Study of a "biological focal region" of high-intensity focused ultrasound", *Ultrasound in Medicine and Biology*, Vol.29, pp: 749-754, (2003)

Wasif, N., J. Garreau, A. K. Terando, D, D. F. Mund, and A. E. Giuliano, "MRI versus ultrasonography and mammography for preoperative assessment of breast cancer", *American Journal of Surgery*, Vol.75, pp: 970-975, (2009)

Watkin, N. A., I. H. Rivens, and G. R. ter Haar, "The intensity dependence of the site of maximal energy deposition in focused ultrasound surgery", *Ultrasound in Medicine and Biology*, Vol.22, pp: 483-491, (1996)

Webb, P. M., M. C. Cummings, and C. M. Furnival, "Changes in survival after breast cancer: improvements in diagnosis or treatment?" *The Breast*, Vol.13, pp: 7-14, (2004)

Weidner, N., J. Folkman, F. Pozza, P. Bevilacqua, E. N. Allred, D. H. Moore, S. Meli, and G. Gasparini, "Tumor angiogenesis: a new significant and independent prognostic indicator in early-stage breast carcinoma", *Journal of the National Cancer Institute*, Vol.84, pp: 1875-1887, (1992)

Weissleder, R., and V. Ntziachristos, "Shedding light onto live molecular targets", *Nature Medicine*, Vol.9, pp: 123-128, (2003)

Wu, F., Z. Wang, Y. Cao, W. Chen, J. Bai, J. Zou, and H. Zhu, "A randomized clinical trial of high-intensity focused ultrasound ablation for the treatment of patients with localized breast cancer", *British Journal of Cancer*, Vol.89, pp: 2227-2233, (2003)

Wu, F., Z. Wang, W. Chen, J. Bai, H. Zhu, and T. Qiao, "Preliminary experience using high-intensity focused ultrasound for the treatment of patients with advanced stage renal malignancy", *Journal of Urology*, Vol.170, pp: 2237-2240, (2003)

Wu, F., Z. Wang, W. Chen, J. Zou, J. Bai, H. Zhu, K. Li, F. Xie, C. Jin, H. Su, and G. Gao, "Extracorporeal focused ultrasound surgery for treatment of human solid carcinomas: early Chinese clinical experience ", *Ultrasound in Medicine and Biology*, Vol.30, pp: 245-260, (2004) Wu, F., Z. Wang, and H. Zhu, "Feasibility of US-guided high-intensity focused ultrasound treatment in patients with advanced pancreatic cancer: initial experience", *Radiology*, Vol.236, pp: 1034-1040, (2005)

Xie, B., J. Ling, W. Zhang, X. Huang, J. Zhen, and Y. Huang, "The efficacy of high-intensity focused ultrasound (HIFU) in advanced pancreatic cancer", *Clinical Oncology and Cancer Research*, Vol.5, pp: 183-186, (2008)

Xu, M., and L. V. Wang, "Photoacoustic imaging in biomedicine", *Review of Scientific Instruments*, Vol.77, pp: 041101, (2006)

Xu, X., H. Zhang, P. Hemmer, D. Qing, C. Kim, and L. V. Wang, "Photorefractive detection of tissue optical and mechanical properties by ultrasound modulated optical tomography", *Optics Letters*, Vol.32, pp: 656-658, (2007)

Yao, G., S. Jiao, and L. V. Wang, "Frequency-swept ultrasound-modulated optical tomography in biological tissue by use of parallel detection", *Optics Letters*, Vol.25, pp: 734-735, (2000)

Yao, G., and L. V. Wang, "Theoretical and experimental studies of ultrasound-modulated optical tomography in biological tissue", *Applied Optics*, Vol.39, pp: 659-664, (2000)

Yaroslavsky, A. N., P. C. Schulze, I. V. Yaroslavsky, R. Schober, F. Ulrich, and H.-J. Schwartz, "Optical properties of selected native and coagulated human brain tissues in vitro in the visible and near infrared spectral range", *Physics in Medicine and Biology*, Vol.47, pp: 2059-2073, (2002)

Yodh, A. G., and B. Chance, "Spectroscopy and imaging with diffuse light", *Physics Today*, Vol.48, pp: 34-40, (1997)

Zemp, R., S. Sakadzic, C. Kim, and L. V. Wang, "Laser speckle statistics in ultrasound-modulated optical tomography ", *Proceedings of SPIE*, Vol.6437, pp: 64371L, (2007)

Zheng, X., and S. Vaezy, "A localization methods of lesions induced by high intensity focused ultrasound based on acoustic backscatter change", *30th Annual International IEEE EMBS Conference*, pp: 3673-3676, (2008)

Zhu, Q., M. Huang, N. Chen, K. Zarfos, B. Jagjivan, M. Kane, P. Hedge, and H. S. Kurtzman, "Ultrasound-guided optical tomographic imaging of malignant and benign breast lesions: initial clinical results of 19 cases", *Neoplasia*, Vol.5, pp: 379-388, (2003)

Zitter, R. N., "Ultrasonic Diffraction of Light by Short Acoustic Pulses", *Journal of the Acoustical Society of America*, Vol.43, pp: 864, (1968)

Vita

Puxiang Lai was born in 1980 in Shanghang, Fujian Province, China. He received a Bachelor of Engineering degree in Biomedical Engineering in 2002 from Tsinghua University, Beijing, China, and a Master of Science in Acoustics in 2005 from Chinese Academy of Sciences, Beijing, China. In September 2005, he entered the doctoral program under the guidance of Professors Ronald A. Roy and Todd W. Murray in the Mechanical Engineering Department of Boston University.